

Modeling of Nucleation and Dynamic Rupture on Heterogeneous Frictional Interfaces with Applications to Foreshocks

A Thesis by
Natalie Sarah Ann Schaal

In Partial Fulfillment of the Requirements
for the Degree of
Doctor of Philosophy

The logo for the California Institute of Technology (Caltech), consisting of the word "Caltech" in a bold, orange, sans-serif font.

California Institute of Technology

Pasadena, California

2018

(Defended May 10, 2018)

© 2018

Natalie Sarah Ann Schaal
ORCID: 0000-0003-4825-4344

All rights reserved

Acknowledgements

There is a long list of people that I would like to thank for their guidance and encouragement throughout my time at Caltech, including faculty, staff, fellow students, friends, and family. My graduate student experience would have not been the same without them.

First, I would like to thank my adviser, Professor Nadia Lapusta, who has been with me on this journey from the start. I am grateful to her for her patience as I acquired my foundational knowledge of geophysics as well as for supporting my interests outside of research, including teaching and university administration. Nadia has mentored me in many facets of life, from research to effective communication to achieving my career goals and beyond. I am truly thankful for her investment in me, care for both my happiness and success, and encouragement to always reach higher.

I would also like to thank the other members of my thesis committee: Professors Thomas Heaton, Guruswami Ravichandran, and Jean-Philippe Avouac. I am grateful to Tom for inspiring me to think outside of the box in scientific discussions and for guiding me in the development of my teaching skills. I have enjoyed interacting with Ravi in a variety of contexts, from discussions of technical topics to careers to initiatives for improving the graduate student experience at Caltech. I also appreciate his warm support of all students and his investment in the Engineering and Applied Sciences Graduate Student Advisory Committee, which we founded together. Jean-Philippe has provided me with an example of excellent teaching, especially in the way

he creates a supportive learning environment in which people from all perspectives can feel comfortable asking questions. I also owe him a special thank you for his insightful comments to my thesis.

In addition to my thesis committee, the current and former members of the Lapusta group have been instrumental in the progress of my research. The group members are caring people who are ready and willing to help with anything, from debugging our code to setting up for events. I owe a special thank you to Carolina Oseguera, Yen-Yu Lin, Semechah Lui, and Junle Jiang.

There are more colleagues at Caltech that I would also like to thank, who I have had the pleasure of working with in a variety of extracurricular contexts. I have enjoyed getting to know them and sharing in our mutual investments in department-wide and campus-wide initiatives. I owe a special thank you to Cassandra Horii and Felicia Hunt, for guiding me in the development of my teaching and leadership skills. I am also thankful for the friends that I have met through participation in leadership activities, for example, via the Graduate Student Council and SOPS. In addition, I truly value the members of the MCE 2012 cohort, who have shared in each step of this journey with me. Special thanks go to Dingyi Sun, Anthony Massari, Tess Saxton-Fox, and Sarah Mitchell.

Finally, I would like to thank my family. I am grateful to them for always encouraging me to pursue my interests and for being my cheerleaders along the way. A special thank you goes to my husband, Christoph, for supporting me both personally and scientifically, and for helping me build confidence in my skills.

Abstract

While many large earthquakes are preceded by observable foreshocks, the mechanisms responsible for the occurrence of these smaller-scale seismic events remain uncertain. One physical explanation of foreshocks with growing support is that they are produced by the interaction of slow slip, due to the nucleation of the upcoming mainshock, with fault patches of different properties. Having a better understanding of how earthquakes nucleate on heterogeneous faults would increase our capacity to forecast potentially hazardous events.

With this motivation in mind, we seek to understand what conditions produce isolated microseismicity within the nucleating region of the mainshock and to study the mechanics of the resulting events. Inspired by the suggestion from laboratory experiments that foreshocks occur on asperities, i.e., local deviations from planarity that are flattened by the overall compression, we explore the behavior of asperity-type patches of higher compressive stress embedded in the larger seismogenic region of a rate-and-state fault model by conducting 3D numerical simulations of their slip over long-term sequences of aseismic and seismic slip. Our models do produce smaller-scale seismicity during the aseismic nucleation of much larger seismic events, and we explore their properties as well as the separation in length scales needed to produce them. These foreshock-like events have stress drops that are consistent with laboratory and field observations and approximately constant, despite the highly elevated compression assigned to the source patches. Two main factors contributing to the reasonable stress

drops are the significant extent of the rupture into the region surrounding the patch and the aseismic stress release just prior to the seismic event.

We also investigate the seismologically-derived properties of the asperity-type events using the spectral analysis commonly applied to natural microseismic events. We find that the seismological methods cannot adequately capture the properties of the simulated events. In part, the seismological estimates of their stress drops are significantly different from the actual stress drops determined from the on-fault stress changes. This is because our sources have more complex features than the standard models from which the current seismological methods have been built, including heterogeneous stress change over the rupture area with much larger initial stress change, and heterogeneous rupture speed. We identify features in the far-field seismograms of the asperity-type sources that differ from the standard models and can be potentially characteristic of the asperity-type sources.

Our asperity-type models of microseismicity sources provide insight into the conditions conducive for generating foreshocks on both natural and laboratory faults and the properties of the resulting events. The conclusions provided jointly by the two perspectives in this study – dynamically simulating the behavior of seismic sources within heterogeneous fault models and seismologically analyzing their far-field source spectra – have important implications that warrant further study. Topics for future research include the interaction among smaller-scale seismic events and their role in the mainshock nucleation process, the effect of timing on their source properties, and relation to the so-called seismic nucleation phase of the subsequent mainshock.

Contents

Acknowledgements	iii
Abstract	v
List of Figures	x
List of Tables	xiv
1. Introduction	1
1.1. Motivation	1
1.2. Modeling of foreshock-like events	2
1.2.1. Inspiration for asperity-type source models	2
1.2.2. Numerical approach and resolution	5
1.3. Mechanics of the simulated intershocks	7
1.4. Investigation of seismologically-derived properties	7
2. Developing models of foreshocks during the nucleation of the upcoming mainshock	10
2.1. Rate-and-state friction and nucleation size	11
2.2. Length scales in the problem and microseismicity isolation	13
2.3. Model geometry and parameters	15
2.4. Exploration of fully isolated microseismic events	21
2.4.1. Sequences of seismic events	21

2.4.2. Nucleation of intershocks	27
2.5. Rupture extent of foreshocks versus the larger-scale nucleation size	32
2.6. Exploration of mainshock triggering by patch-initiated events	35
3. Unexpectedly reasonable stress drops and the underlying rupture mechanics	42
3.1. Stress drops of intershocks	43
3.2. Extended rupture area	48
3.3. Aseismic stress release	49
3.4. Simplified stress drop calculation	55
4. Investigating seismological interpretations of asperity-type sources	60
4.1. Producing synthetic seismograms	61
4.2. Deriving source properties from seismograms	64
4.2.1. Spectral fitting	64
4.2.2. Calculating source properties from spectral parameters	68
4.3. Scaling the simulated source to different moment magnitudes	70
4.4. Comparison of seismologically-derived spectral parameters from the asperity-type sources to idealized models	73
4.4.1. Idealized Source Models (ISMs)	73
4.4.2. Centered Asperity-Type Source Models (CATSMs)	84
4.5. Comparison between stress drops derived from seismological and direct methods	93
4.6. Exploration of potentially characteristic features	103
5. Conclusions and outlook	108
5.1. Conclusions	108
5.1.1. Heterogeneous fault models and the mechanics of intershocks	108
5.1.2. The seismological interpretation of asperity-type events	110

5.2. Linking to natural faults	112
5.3. Discussion of future research directions and associated implications .	115
5.3.1. Building heterogeneous fault models	115
5.3.2. Investigating the mechanics of intershock nucleation and the resulting rupture	121
5.3.3. Exploring seismological interpretations and characteristic fea- tures of asperity-type events	125
A. Appendices	128
A.1. Model parameters and geometry for the preliminary set	128
A.2. Results concerning intershock behavior for the preliminary set	129

List of Figures

2.1. Schematic of important length scales in the problem for a given inter-shock.	14
2.2. Schematic of the modeling process.	16
2.3. Characteristics of the patches used in this study.	18
2.4. Maximum slip rate over the fault as a function of time.	22
2.5. Snapshots of the slip velocity distribution over the seismogenic region for case A.	24
2.6. Snapshots of slip velocity, friction coefficient, and shear stress evolution for an intershock.	26
2.7. Snapshots of slip velocity at the end of the nucleation process of twelve different intershocks.	29
2.8. Long-range triggering between intershocks via postseismic slip and resulting variability in intershock nucleation.	31
2.9. Isolation ratio \tilde{h}_m^*/D_r for the main set of models.	33
2.10. Intershock rupture extent and initiation conditions for one case of low isolation ratio \tilde{h}_m^*/D_r	34
2.11. Snapshots of slip velocity for examples of the three categories of separation between intershocks and mainshocks from the transition set of models.	39
3.1. Stress drops of intershocks as a function of the patch normal stress.	44

3.2. Example of shear stress change due to an intershock.	46
3.3. Shear stress changes that are used to derive the simplified stress drop calculation	47
3.4. Effect of the patch normal stress on the rupture extent.	49
3.5. Average aseismic and seismic stress change on the patches.	51
3.6. Seismic fraction of average shear stress change on the patch.	52
3.7. Effect of simultaneously doubling σ_p and L_p on the seismic fraction of average shear stress change on the patch.	53
3.8. Dependence of the seismic and total average shear stress change (on the patch) of the intershocks on the normal stress ratio for the main set of simulations.	54
3.9. Average shear stress change within the ruptured area outside of the patch $\overline{\Delta\tau_m}$ for intershocks in the main set.	57
3.10. Results for the Variable Background Normal Stress (VBNS) set of simulations.	58
4.1. The assumed coordinate system and focal sphere stations for the production of synthetic seismograms.	62
4.2. Waveforms and spectral fits for event S1 calculated for station on the sphere located at $\theta = 26.5^\circ$ and $\phi = 55^\circ$	66
4.3. Radiation pattern for p-, sh- and sv-waves over the 864 focal sphere stations.	71
4.4. Comparison between dynamic events in models with spatial and slip-related scales different by a factor of 10^3	74
4.5. Source model descriptions.	77
4.6. Comparison of the normalized horizontal source slip profiles of our ISMs to the model from <i>Madariaga</i> [1976].	79
4.7. Comparison of trends in k vs. θ for our Madariaga-like ISM.	81

4.8. Comparison of trends in k vs. θ for our RES-like ISM.	83
4.9. Comparison of trends in k vs. θ for an asperity-type source (event S1)	83
4.10. Comparison of trends in the fall-off rate n vs. θ for a variable n spectral fit for different source models.	85
4.11. Centered Asperity-Type Source Models (CATSMs).	88
4.12. Comparison of trends in k vs. θ for the CATSMs using the constant $n = 2$ fit.	89
4.13. Comparison of trends in k vs. θ for the CATSMs using the variable n fit.	90
4.14. Comparison of trends in the fall-off rate n vs. θ for a variable n spectral fit for the CATSMs.	91
4.15. Comparison of trends in stress drop with patch normal stress ratio calculated seismologically and directly.	96
4.16. Comparison of the seismologically-derived to the direct stress drop for the homogeneous set and CATSMs.	97
4.17. Comparison of seismologically-derived to direct stress drops.	99
4.18. Comparison of seismologically-derived to direct seismic moment for the s-wave spectra.	100
4.19. Comparison of seismologically-derived to direct source radii for the s- wave spectra.	101
4.20. Comparison of seismologically-derived to direct source durations for the s-wave spectra.	102
4.21. Comparison of the seismologically assumed rupture velocity and the direct global rupture velocity.	102
4.22. The dependence of the spherically averaged fall-off rate n on fault and rupture properties.	104

4.23. The dependence of p-to-s corner frequency ratio f_c^p/f_c^s on patch properties.	106
A.1. Spatial distribution of fault properties for model A.3 of the preliminary set.	129
A.2. Maximum slip velocity as a function of time for each model in the preliminary set.	131
A.3. Snapshots of the spatial slip velocity distribution over the seismogenic region of the fault for model A.2 in the preliminary set.	134

List of Tables

2.1. Constant parameters in all models.	19
2.2. Parameters in the main set.	19
2.3. Parameters in the VBNS set.	20
2.4. Highlighted models from the main set.	20
2.5. Parameters for the individual models of the transition set.	37
4.1. Properties of the simulated asperity-type seismic events highlighted in Chapter 4.	67
4.2. Theoretical k values for p- and s-wave spectra for classical idealized and updated source models.	69
4.3. Properties of the Centered Asperity-Type Source Models.	86
4.4. Summary of seismologically-derived non-dimensional quantities for dif- ferent source models.	92
A.1. Model parameters for the preliminary set.	130

1. Introduction

1.1. Motivation

Earthquakes pose a great threat to both people and property around the world, particularly in populated areas near large faults, such as the San Andreas Fault (SAF). With continuous advancements in sensing and computational technology, scientists are making significant strides in understanding earthquake processes, despite the inhibiting restriction that the earthquake sources are typically kilometers to tens of kilometers below the Earth's surface. Still, much of the physics of earthquakes is unknown, and the wide range of seismological, geodetic, and geological observations, along with the highly complex and nonlinear nature of the earthquake phenomena, make the investigation of earthquakes a rich problem to study with powerful consequences.

The focus of the work presented here is on the nucleation and rupture mechanics of earthquakes. The nucleation stage is composed of the processes that make locked or slowly moving faults transition into dynamic rupture, causing radiated seismic waves that we perceive as ground shaking. In addition, many large earthquakes are preceded by smaller seismic events, including foreshocks which are interpreted to occur within the nucleating region of the mainshock and defined as the microseismicity occurring around the hypocenter of the upcoming larger-scale event (mainshock) closely in both time and space [*Jones and Molnar, 1976, 1979; Doser, 1990; Dodge et al., 1995, 1996;*

Abercrombie and Mori, 1996; Maeda, 1999; Reasenber, 1999; Bowman and King, 2001; Zanzerkia et al., 2003; McGuire et al., 2005; Bouchon et al., 2011, 2013; Kato et al., 2012; Brodsky and Lay, 2014]. Currently, foreshocks can only be identified as such post factum, i.e., after the mainshock has occurred, limiting the use of their potential predictive power.

How earthquakes nucleate is a fundamental problem of earthquake science [*Rice and Ruina, 1983; Dieterich, 1992; Rice et al., 2001; Rubin and Ampuero, 2005; Lapusta and Barbot, 2012*], comprised of many unanswered questions. For example, why are foreshocks observed sometimes but not always? What mechanism is responsible for the occurrence of foreshocks and, hence, what is the role of foreshocks in the nucleation of the upcoming mainshock? How are these precursory events able to occur in a nucleation region without immediately triggering the upcoming larger-scale event? Having a better understanding of how earthquakes nucleate would increase our capacity to forecast potentially hazardous events. In particular, if the role of foreshocks in the nucleation of the mainshock could be determined and the ability to identify events as foreshocks before the mainshock occurs could be developed, then, theoretically, this information could be used to forecast dangerous upcoming mainshocks and thereby provide life-saving warnings. With this motivation in mind, we seek to understand what conditions produce isolated microseismicity within the nucleating region of the mainshock, and to study the resulting events along with their properties through numerical modeling.

1.2. Modeling of foreshock-like events

1.2.1. Inspiration for asperity-type source models

One viewpoint with growing evidence is that foreshocks are triggered by slow (aseismic) slip that interacts with fault patches [*Kanamori and Stewart, 1978; Jones and*

Molnar, 1979; Dodge et al., 1995; McGuire et al., 2005; Segall et al., 2006; Liu et al., 2007; Lohman and McGuire, 2007; Kato et al., 2012; Lengliné et al., 2012; Bouchon et al., 2013; McLaskey and Kilgore, 2013; Brodsky and Lay, 2014]. *Dodge et al.* [1996] determined that fault heterogeneity has an important influence both on the location of the nucleating region and the number of foreshocks. This is consistent with a broader view that much of microseismicity may be caused or facilitated by aseismic fault slip [e.g., *Perfettini and Avouac, 2004, 2007; Wei et al., 2015*]. Heterogeneous fault properties could provide the means for smaller-scale seismic events to develop without perturbing the entire seismogenic (earthquake-prone) zone into a mainshock. Moreover, it is likely that fault properties and stresses are heterogeneous on a range of scales [e.g., *Smith and Heaton, 2011*].

An important insight into this problem is provided by unique laboratory experiments of earthquake nucleation on a meter-scale slab of granite [*McLaskey and Kilgore, 2013; McLaskey et al., 2014*]. The experiments produce quasi-static accelerating slip (nucleation process) that grows into dynamic rupture. Significantly, smaller seismically detectable events – foreshocks – occur in the nucleation region. The authors report that these small events, with magnitudes in the range of -7 to -5.5 , typically have stress drops within the expected range for natural earthquakes (1-10 MPa), and argue that these laboratory events are similar to natural earthquakes. Due to persistent locations of the foreshock sources in their repeated experiments, McLaskey and co-authors infer that these small seismic events are occurring at asperities, i.e., bumps, on the fault interface.

Inspired by these experiments, we construct asperity-type sources of smaller-scale seismicity in our rate-and-state fault model via heterogeneous fault properties, namely elevated normal stress, and consider how they interact with a larger-scale nucleation process. From their lab experiments, *McLaskey and Kilgore [2013]* infer a larger-scale nucleation size of about 1 m. They also infer that smaller events occur on patches with

diameters on the order of 1 to 10 cm. Therefore, the model would need to incorporate two scales of nucleation sizes that are 1 to 2 orders of magnitude apart, which can be achieved by increasing the fault-normal stress correspondingly.

While adding patches of higher normal stress to the seismogenic zone may seem like a straightforward way to perturb the larger-scale nucleation process into producing more complex behavior, at first glance, it is not expected to produce realistic behavior. To prevent a smaller-scale event from immediately triggering the nucleation of the mainshock, the event, and hence its nucleation size, needs to be much smaller than the nucleation size of the mainshock; it is not clear that such separation can be achieved for realistic fault properties. Furthermore, since shear stress on a frictional interface is proportional to the normal stress through a friction coefficient, one would assume that changes in shear stress would also be proportional to the normal stress, leading to unrealistically high stress drops for patches of highly elevated normal stress.

Here, we explore the possibility of producing two scales of seismicity within the seismogenic region in a rate-and-state fault model via patches of higher compression, with or without additionally increasing the smoothness of the patches (represented by a reduced characteristic slip distance), and determine the source properties of the resulting events. To do so, we use a numerical approach [*Lapusta and Liu, 2009*] that allows us to study the behavior of these patches over long-term sequences of earthquakes and aseismic slip, focusing on models with isolated microseismicity driven by larger-scale nucleation processes. While we are motivated by the phenomenon of foreshocks, in Chapter 2, we create a more generic model in which the higher-normal-stress patches interact with aseismic creep from the protracted nucleation process of the mainshock. For clarity in the discussion of our results, we coin the term intershocks: microseismicity occurring between two mainshocks within the creeping, nucleating portions of the seismogenic zone. Foreshocks would thereby be a subset of intershocks, depending on the foreshock definition. Since all our simulated inter-

shocks are driven by the surrounding creep within the seismogenic zone, their study is relevant to the process of generating foreshocks, no matter when or where in the interseismic period they occur.

Our goal is to study these asperity-type intershocks in detail, in order to understand the underlying mechanics of these dynamic events along with the conditions under which they are produced. In terms of natural events, we aim to understand foreshock-like microseismicity of moment magnitude 2-3 or smaller. To that end, we focus only on the nucleation phase of the mainshocks by making the entire seismogenic region up to two times larger than the larger-scale nucleation size. Thus, our mainshocks end shortly after nucleating, making them relatively small, and we do not explore the details of their rupture propagation. In particular, our mainshocks are crack-like, in the sense that the local slip duration for most points on the fault is comparable to the overall duration of the event [e.g., *Zheng and Rice, 1998; Noda et al., 2009*]. Some observations suggest that large events are pulse-like [*Heaton, 1990*], with local slip durations much shorter than the overall even duration; the transition between crack-like and pulse-like rupture modes may occur for events that are large enough, e.g., *Meier et al. [2016]* conclude that the transition occurs around M_w 4.5. Studying such large events is beyond the scope of this work.

1.2.2. Numerical approach and resolution

We investigate earthquake nucleation on heterogeneous faults through 3D numerical simulations using laboratory-derived friction laws that have proven to be representative of the frictional resistance of natural faults at slow slip rates typical of nucleation processes. We utilize the simulation methodology of *Lapusta and Liu [2009]*, which enables the analysis of a 2D planar fault enclosed in a 3D homogeneous elastic bulk. Furthermore, it employs the Boundary Integral Method (BIM) to accurately and efficiently model both the inertial effects during simulated earthquakes and slow slips

during relatively long interseismic periods. In contrast to commonly used quasi-dynamic methods, which are often motivated by the reduction of computational cost from simplified handling of inertial effects during dynamic events [Rice, 1993], our simulation approach is fully dynamic. One critical element is the use of the variable time-stepping procedure from Lapusta *et al.* [2000], which chooses short time steps when the slip velocity is fast (dynamic rupture) and long time steps when the slip velocity is slow (interseismic period). Finally, the last critical element for solving these computationally demanding problems, due to the requirement of high spatial and temporal resolution to capture the dynamic effects over many loading cycles, is the use of parallel computing. All of these components combined allow us to simulate long-term fault behavior and to study microseismicity over many mainshock cycles.

To take advantage of the efficient Fourier representation of the Boundary Integral Method (BIM) procedure [Lapusta and Liu, 2009], we consider an infinite interface created by a periodically repeated domain. The output of our simulations is the distribution in space and evolution in time of the slip on the fault. We declare that a seismic event has begun when the slip rate reaches the velocity threshold of 0.1 m/s, which is approximately when the dynamic terms become important [Rubin and Ampuero, 2005] and is a commonly used criterion. Consistent with this definition of seismic slip, any source properties that we report, such as the earthquake moment, are calculated by only including slip at rates above 0.1 m/s.

The stage of fault behavior that is most numerically challenging is dynamic rupture, and the corresponding controlling parameter of the numerical resolution is the cohesive zone size [Day *et al.*, 2005; Lapusta and Liu, 2009]. This important parameter is defined as the spatial length scale over which the shear stress at the propagating rupture front drops from its peak to its residual value. Day *et al.* [2005] established that the initial cohesive zone size needs to be discretized by at least 3 to 5 spatial cells in order for dynamic rupture to be resolved. Since the patches in our simulations have

an increased normal stress (which reduces the cohesive zone size), dynamic rupture on these patches is numerically costly, and so we restrict our patch normal stress to be up to 15 times higher than the background.

Since we simulate the long-term behavior of the fault, the assigned initial conditions at the start of the simulation are not of particular importance. Instead, the pre-stress conditions for an event in the sequence are formed by the stress distribution created by the loading and prior fault slip.

1.3. Mechanics of the simulated intershocks

Our modeling is successful in producing isolated smaller-scale seismic events (intershocks) within the nucleation processes of the upcoming larger-scale event (mainshock). For the smaller-scale seismic events (intershocks) to remain isolated from larger-scale seismic events (mainshocks) within the same fault model, a clear separation of scales is required, as discussed in detail in Chapter 2.

In Chapter 3, the results of our dynamic numerical simulations are discussed further in reference to the rupture mechanics associated with the intershocks. The focus of this chapter is on the important and unexpected result that our models of asperity-type sources produce reasonable and approximately constant stress drops, consistent with observations of natural microseismicity, despite the highly elevated normal stress assigned to the patches. We explain this finding by the rupture mechanics of the intershocks and propose a corresponding simplified theoretical formulation.

1.4. Investigation of seismologically-derived properties

In addition to building an understanding of the rupture mechanics of asperity-type sources in Chapter 2-3, we also investigate their seismologically derived properties (Chapter 4). Small dynamic events occurring in the Earth's crust are routinely an-

alyzed to deduce a number of properties, most commonly their seismic moment and stress drop [Abercrombie, 1995; Dodge *et al.*, 1995; Iio, 1995; Ide and Beroza, 2001; Ide *et al.*, 2003; Shearer *et al.*, 2006; Hardebeck and Aron, 2009; Baltay *et al.*, 2011; Kwiatek *et al.*, 2011; Lin *et al.*, 2012]. The common seismological methods use a conceptual understanding of the earthquake source that involves a number of simplifying assumptions, such as axi-symmetric rupture propagation with a constant rupture speed and spatially uniform stress decrease within the rupture area. Our asperity-type seismic sources are not as simple, as discussed in Chapter 2-3.

Thus, our seismological investigation has two goals. The first one is to find the properties of the simulated asperity-type sources based on the seismological observations and to compare with the actual properties of the sources from our simulations. This comparison would clarify how such sources are currently perceived by seismological studies and would identify any differences or biases that the simplified analysis brings. Our findings would have direct implications for improving the analysis of seismological data to appropriately determine the source parameters and the source type. The second one is to look for any characteristic features in the seismograms of their emitted p- (pressure) and s- (shear) waves that could be used to distinguish these foreshock-like events from other types of microseismicity. The asperity-type sources in our fault models initiate seismic events on the circular patch of higher normal stress and typically rupture significantly far into the surrounding region, resulting in substantially different stress changes on and off of the patch as well as potentially variable rupture speeds. If these characteristics are reflected in the far-field seismograms in a way that can be accurately detected and interpreted, then one could identify a current seismic event as an asperity-type event and potentially a foreshock, contributing to the physics-based forecasting of the upcoming mainshock.

In the course of our investigation, we also clarify an under-appreciated problem with the idealized source models that motivates the current practices in the analysis

of microseismicity, namely the fact that the kinematic simplicity of axi-symmetric rupture propagation with uniform rupture speed and uniform stress drop is quite difficult to achieve in a dynamic model, as discussed and demonstrated in Chapter 4. This problem has resulted in several variants of the seismological analysis, with significant implications for the inferred source properties. Furthermore, this implies that the commonly-envisioned assumptions are actually not the simplest, in the sense that any realistic source is unlikely to have those properties.

Still, as a point of reference, we compare seismological results from the asperity-type sources to those from classical idealized source models. We chose to include standard approaches within in our study to see how a typical seismologist would interpret our asperity-type events if they occurred in a natural fault setting. Our findings also have direct implications for improving the analysis of seismological data to appropriately determine the source parameters and the source type. Based on our analysis, we then propose potentially characteristic seismological trends.

2. Developing models of foreshocks during the nucleation of the upcoming mainshock

This chapter begins with a brief review of the rate-and-state friction law that governs the resistance of the interface in our simulations, including estimates for the critical minimum length scale associated with transition from quasi-static to dynamic rupture, nucleation size h^* . The chapter continues on to present the important length scales relevant to creating our heterogeneous fault models in which two scales of seismic events can occur, followed by examples of the timing of intershocks within the mainshock recurrence interval and the variability of intershock nucleation, even within the same simulation. Finally, the chapter is concluded with a discussion of the separation in critical length scales needed for reliable isolation of patch-initiated events, as well as an exploration of the behavior in transitional cases between isolation and immediate triggering of the mainshock.

In this chapter, Sections 2.1-2.5 are based on the first part of the manuscript in the final stages of preparation, entitled, “Microseismicity on patches of higher compression during larger-scale earthquake nucleation in a rate-and-state fault model” by Natalie Schaal and Nadia Lapusta.

2.1. Rate-and-state friction and nucleation size

The law governing the frictional resistance of the fault in our model is rate-and-state friction. Derived from laboratory experiments on rocks at slow slip rates, rate-and-state friction has had much success in reproducing many earthquake phenomena, including earthquake nucleation, postseismic slip, aftershocks, and repeating earthquakes [e.g., *Dieterich, 2007; Kaneko et al., 2016; Lwi and Lapusta, 2016; Jiang and Lapusta, 2017*].

In the rate-and-state friction laws, the frictional shear strength is related to effective normal stress through a dependence on the slip rate and “state” of the interface instead of the constant coefficient from classical Coulomb friction. In particular, the form applied in this study is the widely-used Dieterich-Ruina (DR) rate-and-state law, for constant effective normal stress [*Dieterich, 1979; Ruina, 1983*]:

$$\tau = \sigma \left(f_* + a \ln \left(\frac{V}{V_*} \right) + b \ln \left(\frac{V_* \theta}{L} \right) \right), \quad (2.1)$$

$$\dot{\theta} = 1 - \frac{V\theta}{L}, \quad (2.2)$$

where τ is the shear resistance, σ is the effective normal stress (normal stress minus pore pressure), V is the slip rate, θ is a variable representing the “state” of the interface in contact (in units of time), L is the characteristic slip distance, a and b are rate-and-state parameters of the order of 0.01, and f_* is the reference friction coefficient at the reference slip velocity V_* . For a constant slip velocity V , the state variable θ evolves to its steady-state (ss) value $\theta_{ss} = L/V$, transforming the shear resistance τ into its steady-state form, $\tau_{ss} = (f_* + (a - b) \ln(V/V_*))$. The sign of the quantity $(a - b)$ has important implications for the frictional stability of the modeled interface through its rate dependence. If $(a - b) > 0$, then we have velocity-strengthening behavior in steady state, which means that the faster the interface slips the higher the

frictional resistance. If instead $(a - b) < 0$, then we have velocity-weakening behavior in steady state, meaning the frictional resistance decreases with increasing sliding velocity. While velocity-strengthening interfaces respond to slow tectonic loading with slow stable slip, velocity-weakening interfaces can produce spontaneously accelerating slip (i.e., an earthquake) [*Rice and Ruina, 1983; Dieterich, 1992; Rubin and Ampuero, 2005*].

In order for an interface to transition into dynamic rupture, not only does the frictional dependence need to be velocity-weakening, but also the size of the nucleating region with these properties needs to be larger than the nucleation size h^* [*Rice and Ruina, 1983; Rice et al., 2001; Rubin and Ampuero, 2005*]. Theoretical estimates for the nucleation size are generally based on stability analyses in homogeneous 2D settings. We utilize the estimate:

$$\tilde{h}_{\text{RA}}^* = \frac{2}{\pi} \frac{\hat{\mu} b L}{(a - b)^2 \sigma}, \quad (2.3)$$

where $\hat{\mu} = \mu$ for mode III ruptures and $\hat{\mu} = \mu / (1 - \nu)$ for mode II ruptures, μ is the shear modulus, and ν is Poisson's ratio. This estimate was derived by *Rubin and Ampuero [2005]* from a fracture energy balance analysis of a crack extending quasi-statically for the DR rate-and-state parameter regime of $a/b > 0.5$. For a fault in a 3D elastic medium, the nucleation size estimate is expected to increase by a factor of 2 or 3; in particular, the 3D estimate of:

$$\tilde{h}_{\text{3D}}^* = (\pi^2/4) h_{\text{RA}}^* \quad (2.4)$$

with $\hat{\mu} = \mu$ has been successful in matching the combined nucleation sizes produced by 3D earthquake simulations *Chen and Lapusta [2009]*, and it is the estimate used in this study.

The ratio between the size of the seismogenic region W_{seis} and the nucleation size

h^* is a helpful indicator of how prone to instability a given fault is. A ratio of $W_{seis}/h^* < 1$ implies quasi-static behavior (no earthquakes), whereas a value greater than one predicts stick-slip behavior [*Lapusta and Liu, 2009*].

As the estimates show (e.g., Equation 2.3), the nucleation size depends on the effective normal stress and fault frictional properties. In addition, simulations show that there are other factors that can affect the nucleation size h^* , such as the loading rate. In particular, the work of *Kaneko and Lapusta [2008]* provides an example of a stress step in loading can reduce the nucleation size by an order of magnitude. Furthermore, since the aforementioned \tilde{h}^* estimates are for homogeneous faults, the appropriate treatment in a heterogeneous setting is an open question.

2.2. Length scales in the problem and microseismicity isolation

With the goal of producing isolated microseismicity within the protracted nucleation region of the mainshock, we consider circular patches of higher compression within the seismogenic zone. In order for the dynamic ruptures on these patches to remain separated from the upcoming mainshock, a separation in length scales is needed (Figure 2.1).

To produce a seismic event on a patch, the patch diameter D_p needs to be comparable to or larger than the local nucleation size h_p^* . When the patch ruptures, our simulations show that the rupture extent of the intershock D_r is larger, and often much larger, than the patch diameter D_p . At the same time, D_r needs to be sufficiently smaller than the mainshock nucleation size h_m^* or else the patch rupture immediately triggers the mainshock, with no smaller-scale seismicity. Therefore, the nucleation size on the patch h_p^* and the mainshock nucleation size h_m^* need to be well

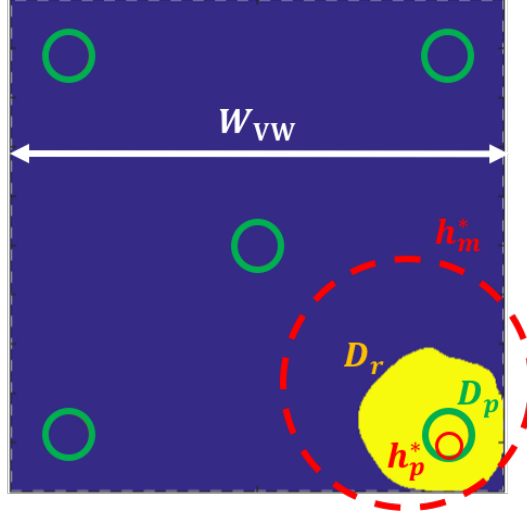


Figure 2.1.: Schematic of important length scales in the problem for a given intershock: h_p^* , nucleation size of a patch with higher normal stress; D_p , diameter of the patch; D_r , diameter of ruptured area in a patch-initiated seismic event; h_m^* , nucleation size of the mainshock; and W_{VW} , size of the velocity-weakening region (seismogenic zone). For smaller-scale seismicity to occur on the patch, $D_p \geq h_p^*$ is generally needed. For the mainshock to occur, $W_{VW} > h_m^*$ is needed. In order for a patch-initiated seismic event to be reliably isolated from the mainshock, D_r must be sufficiently separated from h_m^* , i.e., $D_r \ll h_m^*$. Our simulations show that $D_p \ll D_r$ in many cases. Thus, satisfying the condition $h_p^* \leq D_p \ll D_r \ll h_m^* < W_{VW}$ enables the occurrence of many intershocks per mainshock.

separated according to

$$h_p^* \leq D_p \ll D_r < h_m^* . \quad (2.5)$$

Furthermore, the mainshock nucleation size h_m^* must be smaller than the size of the velocity-weakening region W_{VW} for mainshocks to initiate in the background seismogenic region. This condition provides larger-scale seismic events in addition to the smaller-scale seismic events initiating on circular patches of higher normal stress σ_p , and its effect is discussed further in Section 2.5. In addition, we separate the centers of the patches by approximately \tilde{h}_m^* diagonally and approximately $1.5\tilde{h}_m^*$ in the vertical and horizontal directions so that the patches are close enough for the mainshock nucleation to involve the patches yet as distant as possible to ensure that the intershocks are isolated from one another. Considering scenarios of more densely

patches that are placed with grid-like or random spacing is outside the scope of this work and remains an interesting problem for a future study.

2.3. Model geometry and parameters

Our fault model (Figure 2.2) is divided into three main regions: a seismogenic (velocity-weakening) zone where earthquakes can happen, a stably creeping (velocity-strengthening) section, and a boundary region where a “plate rate” style loading is applied (Figure 2.2b). The velocity-strengthening region serves to transmit the slow loading to the initially locked seismogenic zone. The loading rate is chosen to approximately reproduce the average shear stress rate of 0.001 MPa/s on the fault, from the motivating work of *McLaskey and Kilgore* [2013].

In our models, both the circular patches and the surrounding seismogenic zone have the same velocity-weakening parameters a and b . This setup is in contrast to the more common approach of velocity-weakening patches embedded in a velocity-strengthening creeping region [e.g., *Chen and Lapusta*, 2009]. There is an important difference between the two types of models: dynamic ruptures on patches embedded in a velocity-strengthening region tend to arrest in the surrounding region [e.g., *Lui and Lapusta*, 2016] unless enhanced dynamic weakening is present there [e.g., *Noda and Lapusta*, 2013], whereas in our model, both the patches and the immediate surrounding region can sustain dynamic slip, as they both are velocity-weakening. The rate-and-state parameters a and b used in this study are on the order of 0.01, and the constant L_m on the background of the fault falls within the typical range of 1-100 microns, as in laboratory experiments on rock specimens [e.g., *Dieterich and Kilgore*, 1996; *Marone*, 1998; *Dieterich*, 2007].

Within the seismogenic zone, we place a grid of circular patches of higher normal stress (Figure 2.2a) to ensure that the mainshock nucleation will interact with some

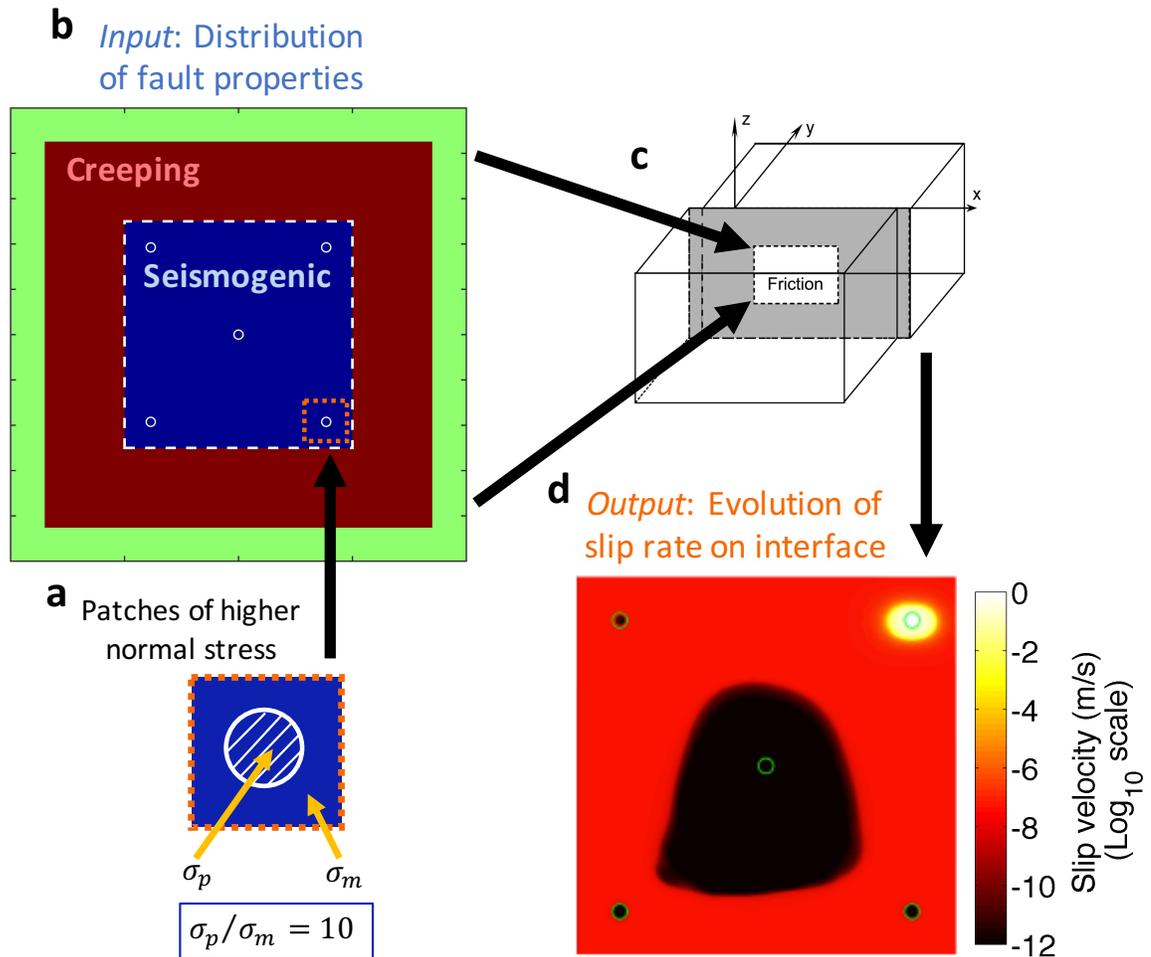


Figure 2.2.: Schematic of the modeling process. **(a)** A typical circular patch of higher normal stress in our model. **(b)** The circular patches (5 in this case) are distributed within the seismogenic zone (blue), which is loaded by the surrounding creeping region (red) and transmits the plate-rate loading from the boundary region (green). **(c)** The 2D heterogeneous fault is embedded in a 3D homogeneous elastic bulk. Through fully dynamic calculations, the result of our simulations is the evolution of slip and stress on the fault. **(d)** An example snapshot of slip rate over the seismogenic region during a patch-hosted seismic event (upper right patch).

of the patches, regardless of where the nucleation originates. This grid-like placement of the patches is not meant to be indicative of the asperity distribution on natural or laboratory faults, but instead provides a simplified geometry with well-spaced sources. The arrangement of our model allows us to explore isolated smaller-scale seismic events within the extended nucleation region of the mainshock, driven by the mechanism of slow slip from the mainshock nucleation. While we explore a variety of patch properties for producing intershocks, the number and location of the patches are held constant.

The circular patches within the seismogenic region are characterized by higher compression σ_p and/or lower characteristic slip L_p (Figure 2.3ab). The higher normal stress σ_p represents more pronounced “bumps.” After the two sides of the fault repeatedly slide past each other over many events, the asperities may also become smoother, represented by a reduced characteristic slip distance L_p within our rate-and-state framework. Recalling the nucleation size estimate (Equation 2.4), both a higher value of normal stress σ_p and a reduced value of L_p contribute to a smaller local nucleation size on the patches h_p^* , leading to a separation in nucleation length scales that potentially allows for isolated microseismicity. Given our focus on exploring patches of higher normal stress, whenever we additionally decrease L_p to help produce a smaller nucleation size, the L ratio L_p/L_m is 0.5. Thus, the main variable characteristics of our patches can be described by the following non-dimensional parameters: normal stress ratio σ_p/σ_m , characteristic slip distance ratio L_p/L_m , patch instability ratio D_p/\tilde{h}_p^* , and nucleation size ratio $\tilde{h}_m^*/\tilde{h}_p^*$ (Figure 2.3).

The models included in this work are divided into two sets: the main set and the Variable Background Normal Stress (VBNS) set. Both sets share the same fundamental properties, such as the bulk material properties, the rate-and-state parameters, and the loading rate (Table 2.1). The central difference between these sets is that the models in the main set all have the same background normal stress σ_m , while the

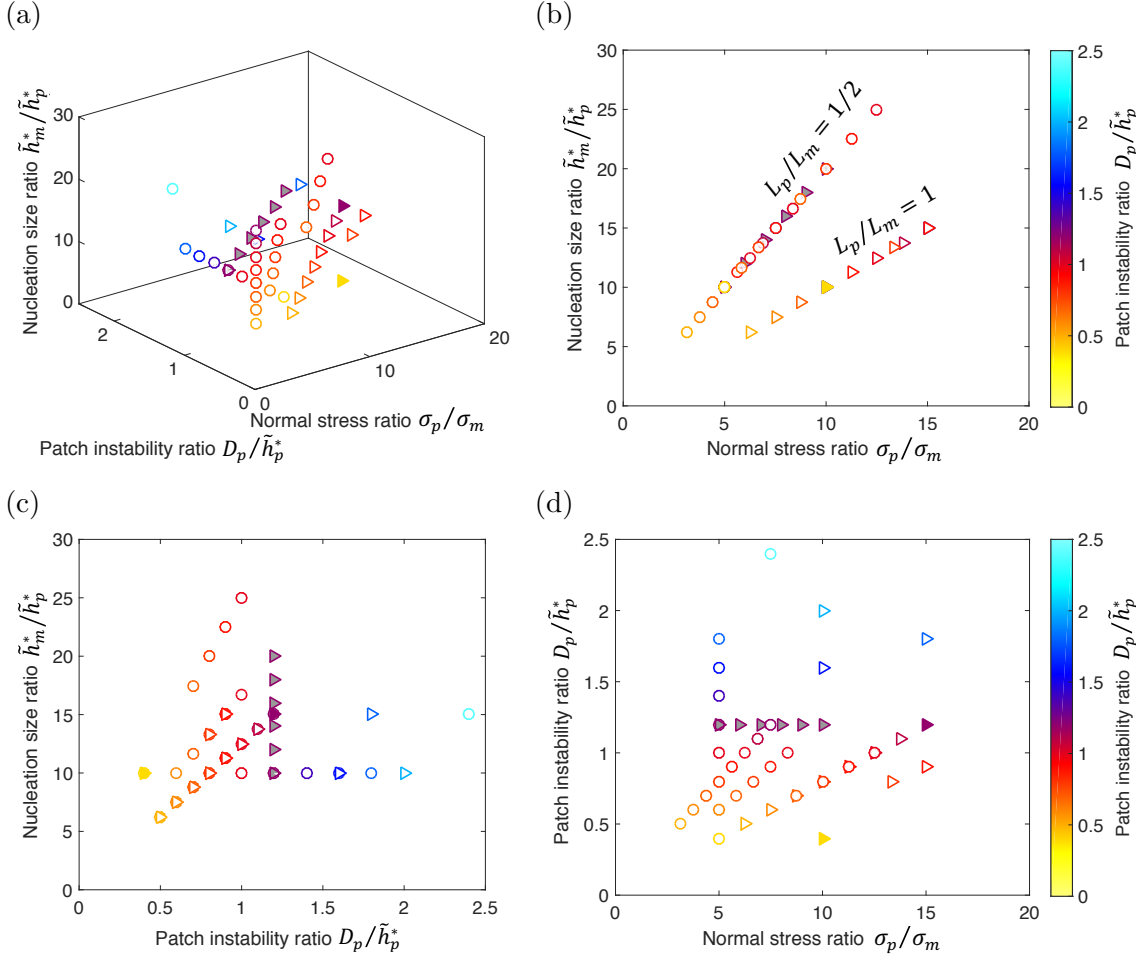


Figure 2.3.: Characteristics of the patches used in this study. Each marker represents one model, while the outline color indicates how prone to dynamic instability the patches should be. Circular and triangular markers identify models with $L_p/L_m = 1/2$, and $L_p/L_m = 1$, respectively. Gray-filled markers indicate models from the VBNS set (discussed in detail in Section 3.4), which all produce intershocks. For the main set, markers filled with the same color as their outline color represent models that do not produce intershocks (i.e., only produce mainshocks) and white-filled markers indicate models that do produce intershocks and thereby satisfy the required separation of scales (Equation 2.5). **(a)** 3D plot indicating the separation in nucleation sizes between the intershocks and mainshocks, instability ratio of the patches, and elevated normal stress on the patches, showing the span of properties explored in this study. **(b)** Since \tilde{h}^* is proportional to σ and inversely proportional to L (Equation 2.4), the relationship between the separation in nucleation sizes and normal stress ratio falls into two distinct lines, one for each L_p/L_m . For the main set, since σ_m , L_m , and \tilde{h}_m^* are held constant, the same $\tilde{h}_m^*/\tilde{h}_p^*$ can be achieved by doubling both L_p and σ_p . For the VBNS set, since σ_p and \tilde{h}_p^* are held constant, increases in \tilde{h}_m^* via decreases in σ_m result in the same linearity between $\tilde{h}_m^*/\tilde{h}_p^*$ and σ_p/σ_m as for the main set. **(c-d)** The remaining distinct sides of the 3D plot in (a).

patch properties are varied (Table 2.2), and for the VBNS set the patch properties are held constant, while the value of σ_m , and hence σ_p/σ_m , is varied (Table 2.3).

Table 2.1.: Constant parameters in all models; “background” refers to the values in the VW region outside of the patches, which are denoted by a subscript “m” for “main.”

Parameter	Symbol	Value
Background characteristic slip distance	L_m	1 μm
Rate-and-state properties in VW region	a	0.0100
	b	0.0255
Reference friction coefficient	f_*	0.6
Reference slip velocity	V_*	10^{-6} m/s
Poisson’s ratio	ν	0.25
Shear modulus	μ	30 GPa
S-wave speed	c_s	3.0 km/s
P-wave speed	c_p	5.2 km/s
“Plate” loading rate	V_{pl}	4.0×10^{-8} m/s

Table 2.2.: Parameters in the main set.

Parameter	Symbol	Value
Estimated background instability ratio	$W_{\text{VW}}/\tilde{h}_m^*$	2
Background normal stress	σ_m	10 MPa
Diameter of patch	D_p	2-10 cm
Normal stress ratio	σ_p/σ_m	3.13-15.00
Characteristic slip distance on patch	L_p	0.5 or 1.0 μm
Estimated patch instability ratio	D_p/\tilde{h}_p^*	0.4-2.4
Estimated ratio of background nucleation size to patch nucleation size	$\tilde{h}_m^*/\tilde{h}_p^*$	6-25

Within the results presented here, three representative simulations from the main set are repeatedly highlighted. For ease of discussion, we call them cases A-C (Table 2.4).

While the vast majority of the models studied here do result in intershocks, the

Table 2.3.: Parameters in the VBNS set.

Parameter	Symbol	Value
Estimated background instability ratio	$W_{\text{VW}}/\tilde{h}_m^*$	1-2
Background normal stress	σ_m	5-10 MPa
Diameter of patch	D_p	6 cm
Normal stress ratio	σ_p/σ_m	5-10
Characteristic slip distance on patch	L_p	0.5 μm
Estimated patch instability ratio	D_p/\tilde{h}_p^*	1.2
Estimated ratio of background nucleation size to patch nucleation size	$\tilde{h}_m^*/\tilde{h}_p^*$	10-20
Estimated background nucleation size	\tilde{h}_m^*	0.5-1.0 m
Normal stress on patch	σ_p	50 MPa

Table 2.4.: Highlighted models from the main set.

Model name	D_p/\tilde{h}_p^*	σ_p/σ_m	L_p/L_m	$\tilde{h}_m^*/\tilde{h}_p^*$
Case A	0.8	10.0	1	10
Case B	1.8	5.0	1/2	10
Case C	2.4	7.5	1/2	15

few models that do not can provide insight into the bounds of this phenomenon. Two different scenarios for suppressing intershocks have emerged in the two sets of models presented here: (1) overly strong patches, and (2) sub-seismic patches. In the first scenario, despite the patches having an instability ratio greater than one, the loading from the interseismic creep is not enough to reach the level of shear stress on the patch needed to cause high (seismic) slip rates before the upcoming mainshock begins in the surrounding area. In the instance where this occurs in our study, the normal stress ratio σ_p/σ_m is 15 and the patch instability ratio D_p/\tilde{h}_p^* is 1.2 (purple filled-in triangle in Figure 2.3). Notably, two other models in our study also have $\sigma_p/\sigma_m = 15$, but they have different instability ratio and patch size, allowing for the occurrence of intershocks. The second scenario arises when the patches have too low of an instability

ratio to host seismic events. Interestingly, this lower bound on instability ratio seems to be dependent on the normal stress ratio as well: for two models with $D_p/\tilde{h}_p^* = 0.4$ in our study, the one with $\sigma_p/\sigma_m = 10$ and $L_p/L_m = 1$ does not produce intershocks (yellow filled-in triangle in Figure 2.3), while the other case with $\sigma_p/\sigma_m = 5$ and $L_p/L_m = 1/2$ does produce some intershocks. In addition, recall that an insufficient separation of scales would also prevent intershocks from happening, for example, when a patch-initiated dynamic rupture grows large enough to reach the nucleation size of the mainshock (Section 2.2). Clearly, the full description of the conditions for producing intershocks is complex. Note that, especially in cases with $D_p/\tilde{h}_p^* < 1$, a significant part of the nucleation occurs outside of the patch (Figure 2.7).

2.4. Exploration of fully isolated microseismic events

2.4.1. Sequences of seismic events

In the reference case of a homogeneous seismogenic zone, our simulations produce periodic sequences of events that span the velocity-weakening region and settle into a regular recurrence interval (Figure 2.4a); we refer to these events as mainshocks. In contrast, when we create heterogeneous faults by adding the circular patches of higher normal stress, the sequences of events become complicated (Figure 2.4b-c). Now both mainshocks and intershocks occur, with the intershocks sometimes occurring closely before, closely after, or far between the mainshocks. This irregular pattern persists, despite the fact that all of the five patches in a given model share the same properties (D_p , σ_p , L_p , a , and b).

The heterogeneity in slip and shear stress created by the rupturing of these patches contributes to the complexity in the mainshock sequences as well. Although we do not focus here on how the occurrence of intershocks, which may be considered to be by-products of the mainshocks nucleation process, affects the mainshock nucleation

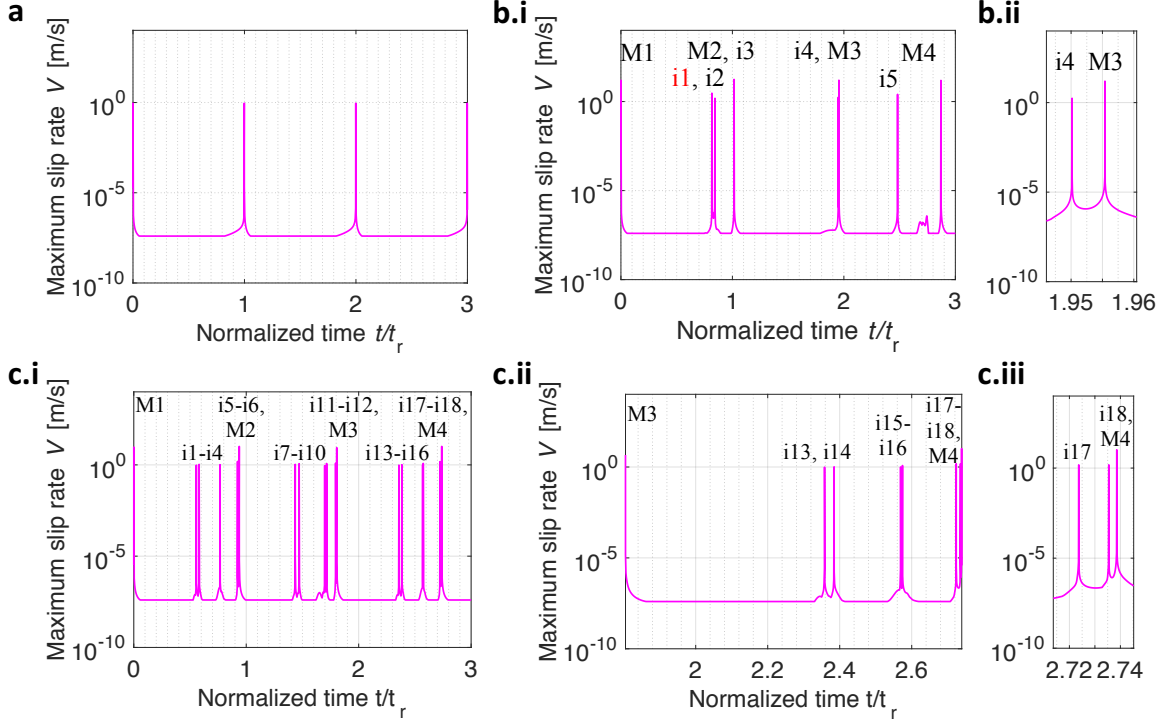


Figure 2.4.: Maximum slip rate over the fault as a function of time. Flat sections correspond to the loading velocity of 4×10^{-8} m/s, and velocity spikes of the order of 10^0 m/s are seismic events. **(a)** The case of a homogeneous seismogenic region (i.e., no patches). **(b.i)** The heterogeneous fault of case A. **(c.i)** A heterogeneous fault with the same instability ratio of case A, except with $L_p/L_m = 1/2$, and $\sigma_p/\sigma_m = 6.66$. For all subplots, $t = 0$ corresponds to the fifth mainshock in the simulation, and the time axes are normalized by the average recurrence time t_r of the homogeneous case. Seismic events are labeled, where “M#” and “i#” enumerate mainshocks and intershocks, respectively. **(b.ii)** Expanded snippet of (b.i) to show how closely i4 happens before M3 (time separation is approximately 0.5% of t_r). **(c.ii)** Events for the last mainshock cycle shown in (c.i). **(c.iii)** Expanded snippet of (c.ii) to highlight two intershocks that occurred closely before M4 (time separation between i17 and M4, and i18 and M4 was approximately 1.5% and 0.3% of t_r , respectively). Event i1 in (b.i) labeled in red is analyzed in more detail in Figure 2.6.

process, the two heterogeneous fault cases shown here (Figure 2.4b-c) provide examples of this effect. Consider the case in Figure 2.4c.i, for example: even though the patches of higher normal stress should make the fault stronger overall, the mainshocks systematically happen earlier than in the homogeneous case (Figure 2.4a), corresponding to an average reduction in recurrence time of 10% per cycle (calculated over 10 mainshocks). Therefore, despite effectively adding “nails” to the seismogenic zone, the recurrence time of the mainshock decreases. This counter-intuitive result is likely due to an accelerated nucleation process, which could be facilitated by one or a combination of the following factors: accelerated postseismic slip from the previous intershocks providing increased loading, one of the foreshock-like events growing into a mainshock, a smaller amount of slip per mainshock, or other factors. These effects would be interesting to investigate further in future work.

The chosen patch properties in a given model determine the frequency of intershock occurrence. In case A (Figure 2.4b), typically two intershocks occur per mainshock cycle, whereas in a case with the same instability ratio but smaller patches, lower normal stress, and lower characteristic slip (Figure 2.4c), six intershocks per cycle is typical. The last cycle in Figure 2.4c.i is expanded in Figure 2.4c.ii and Figure 2.4c.iii to provide an example of how the occurrence of intershocks tends to increase in the latter half of the interseismic period of the mainshock, and to highlight the intershocks occurring just before the upcoming mainshock. Based on their timing, these intershocks are the most foreshock-like. Note, however, that the entire sequence of intershocks is foreshock-like, in the sense that these events are triggered by the slow aseismic nucleation of the following larger dynamic event. Since the overall velocity-weakening domain is only double the larger-scale nucleation size, most of the interseismic period is also the nucleation period for the upcoming larger event.

To visualize a representative interseismic period between mainshocks, Figure 2.5 shows snapshots of the spatial distribution of slip velocity from the event sequence

in Figure 2.4b. At the start of this sequence of snapshots, the seismogenic region is locked (Figure 2.5a). As the aseismic slip develops in the velocity-weakening region and interacts with the patches, an intershock occurs at the upper right patch (Figure 2.5b) and results in postseismic slip (Figure 2.5c). Another intershock and its resulting postseismic slip occur soon thereafter (Figure 2.5d-e). Finally, a mainshock nucleates in the upper right quadrant (Figure 2.5f) and proceeds to rupture the entire seismogenic region. These examples (Figures 2.4 and 2.5) show that our simulated fault behavior has the qualitative features that we set out to achieve, namely the occurrence of smaller-scale isolated seismic events within the aseismic slip of the continued nucleation process of the upcoming larger-scale event.

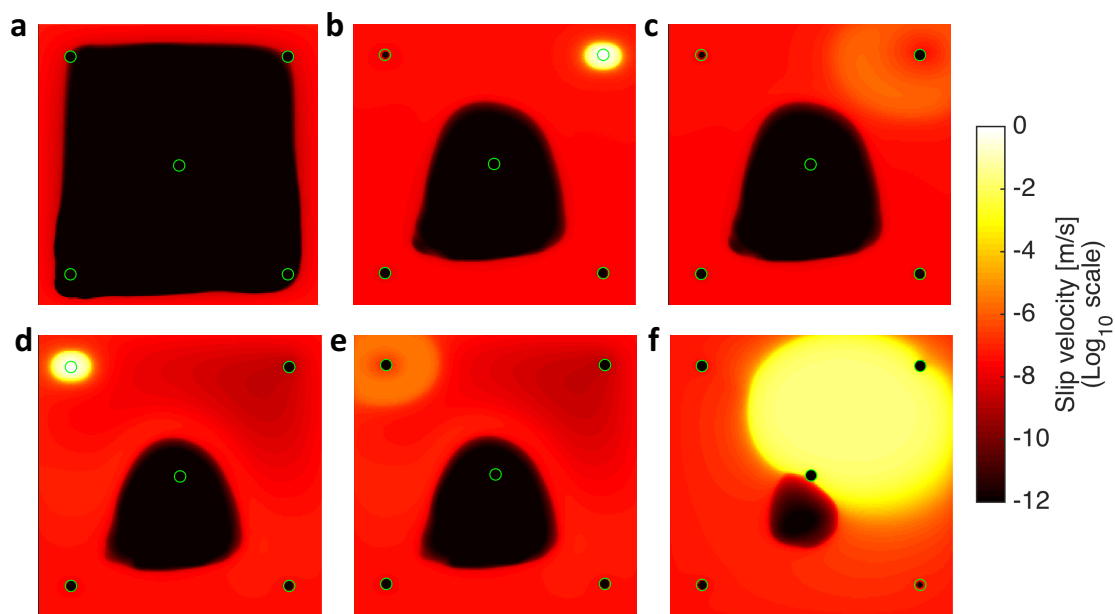


Figure 2.5.: Snapshots of the slip velocity distribution over the seismogenic region for case A, with the five circular patches outlined in green. On this log scale, bright yellow and white correspond to seismic slip rates, orange and red correspond to aseismic slip, and black indicates regions that are effectively locked. The panels capture the interseismic creep before event M2 in Figure 2.4b that includes two intershocks (i1 and i2). (a) Early interseismic period. (b-c) Intershock i1 and the associated postseismic slip. (d-e) Intershock i2 and its postseismic slip. (f) Late stages of the nucleation of mainshock M2.

The classification choice of mainshock or intershock for most of the seismic events

discussed in this work is obvious (e.g., events in Figure 2.5). However, in some cases, the rupture complexity produces less of a distinction between the two groups, with dynamic events rupturing most but not all of the velocity-weakening region. For clarity and consistency in the discussion of our simulation results (e.g., for designating the relative rupture extent D_r/D_p in Section 3.2), we define the intershocks to be patch-initiated events that either partially or completely rupture a single patch of elevated normal stress and have a rupture area that is less than two thirds of the total area of the seismogenic zone. Mainshocks are larger-scale events that often rupture the entire velocity-weakening region, serving to reset the loading cycle. Our mainshocks are not much larger than their nucleation size, only by a factor of about 2, for computational efficiency. In other words, our model is designed to simulate the nucleation process that interacts with stronger fault patches, produce some intershocks, allow the larger-scale nucleation to accelerate to dynamic slip, and then to arrest the larger-scale event soon afterwards. As such, our “mainshocks” are not the focus of this study and we do not analyze them in depth here.

The plethora of data provided by our numerical simulations allows us to study the details of how the patches of higher normal stress are loaded by the surrounding aseismic creep and rupture in a dynamic event (Figure 2.6). This process of an intershock on a patch can be illustrated by four quantities from our simulations: the logarithm of the slip velocity $\log_{10}(V)$, the slip velocity itself V , the effective friction coefficient τ/σ , and the shear stress τ (rows A-D in Figure 2.6). The logarithm of the slip velocity highlights the acceleration of slip as the intershock nucleates, but blurs the details in the seismic slip velocity distribution. Snapshots directly of the slip velocity, on the other hand, show the progression of the seismic rupture (seismic slip rates are shown as all colors other than orange in row B of Figure 2.6). The effective friction coefficient, which is the shear stress normalized by the normal stress, emphasizes the shear stress change outside of the patch. Lastly, snapshots directly of

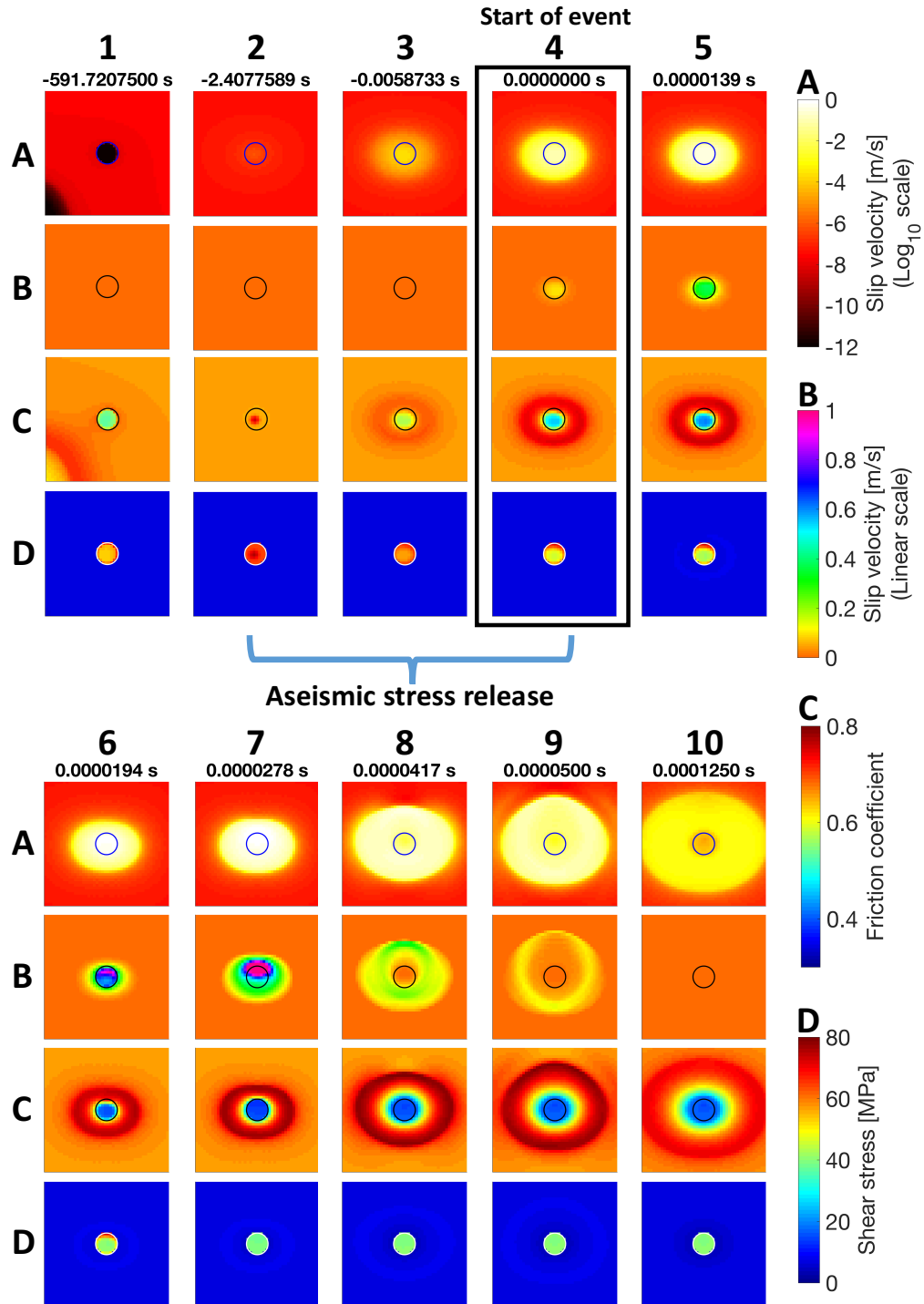


Figure 2.6.: Snapshots of slip velocity (rows **A** and **B**), friction coefficient (row **C**), and shear stress (row **D**) evolution for an intershock (event i1 from Figure 2.4b.i, i.e., case A). The color scale of row **A** is the same as in Figure 2.5 and the color scale for row **B** highlights the seismic slip velocity comparable to the threshold of 0.1 m/s (yellow). The time relative to the start of the intershock (in seconds) is displayed above each column of snapshots, with a black box highlighting the column corresponding to the event start.

the shear stress detail the buildup and lowering of shear stress on the patch.

In the nucleation process of an intershock, the patch starts locked (Figure 2.6A1) until aseismic slip due to the larger-scale nucleation process around the patch engulfs it (Figure 2.6A2), accelerating the slip rates through the start of the seismic event (Figure 2.6B4). From this point on, the slip rates continue to rise as the event ruptures the patch and extends into the surrounding region (Figure 2.6B5-B9) until it dies out (Figure 2.6B10). Additionally, comparing the slip rate and shear stress in a period prior to the start of the seismic event reveals that the shear stress builds up to a peak and then drops slowly until the event starts (Figure 2.6D1-D4), while the slip rates were below the seismic threshold and seemingly stagnant (Figure 2.6B1-B4). This aseismic stress release just before the seismic event occurs within the nucleation zone of the patch, which occupies most of the patch in this particular case, and would likely be difficult to detect on natural faults. However, it can be explored via numerical simulations and is discussed further in Section 3.3. The surprisingly large extent of the rupture into the region outside of the patch is also discussed further, in Section 3.2.

2.4.2. Nucleation of intershocks

In order for a seismogenic (velocity-weakening) region to produce a dynamic event, the region must be larger than its corresponding nucleation size h^* (Section 2.1). To determine the potential for a given zone to produce seismic events, the nucleation size can be estimated based on theoretical considerations, e.g., Equations (2.3) and (2.4). While this estimate is derived for a seismogenic region with homogeneous properties, the case of our simulations is much different, as we model the 3D problem with a seismogenic region that has heterogeneous normal stress and occasionally heterogeneous characteristic slip distance. Since the effect of heterogeneity on nucleation size is not rigorously known, we set up our suites of model parameters based on the nucleation

size from Equation (2.4). For clarity, to indicate that this is an estimate for the nucleation size and that it is calculated from the model parameters prior to running the simulation, we notate it with a tilde, as \tilde{h}^* . Correspondingly, the tilde is omitted when we refer to the actual nucleation size, h^* .

Snapshots of the logarithm of the slip velocity V distributed on and around the patch at the moment when the seismic event starts illuminate how the intershocks in our models nucleate (Figure 2.7). It is apparent that events nucleating on a patch typically involve area adjacent to the patch in the nucleation as well (bright yellow regions in all events included in Figure 2.7). This behavior allows for the initially unexpected result that patches with $D_p/\tilde{h}_p^* < 1$ can still produce seismic events (e.g., events from case A in Figure 2.7a.1-a.3). In addition, understanding how the patch properties translate into nucleation behavior is further complicated by the observation that features of the nucleation at the time it completes – for example, the proportion of the nucleating area within the patch, the amount of the patch that is locked, and the speed of the creep outside of the patch – vary for different events within the same simulation (e.g., Figure 2.7c.1-c.3).

Some of the variability in the intershock nucleation within the same simulation can be attributed to the interaction between events via postseismic slip. A particularly clear example of one intershock influencing the upcoming intershock in this way is shown in Figure 2.8. In this example, the first intershock nucleates normally with accelerated slip over the entire patch as the nucleation completes (Figure 2.8c.1). The second intershock, on the other hand, begins when part of the patch is still locked (Figure 2.8h.1). Analyzing a sequence of slip velocity snapshots (with the scale cropped to highlight creeping speeds) shows that the postseismic slip of the first event travels over to a neighboring patch, causing it to rupture sooner (Figure 2.8e-h). This postseismic perturbation from the previous event allows the second patch to complete its nucleation early, with an apparently smaller nucleation size. The notion

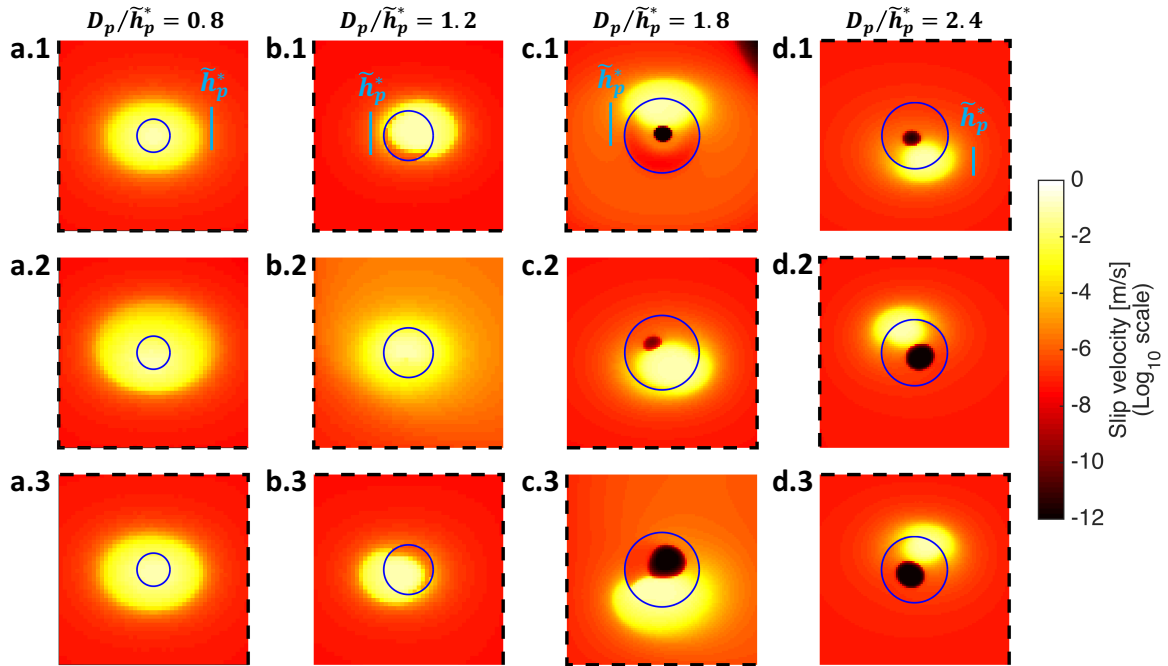


Figure 2.7.: Snapshots of slip velocity at the end of the nucleation process of twelve different intershocks. The columns (**a-d**) correspond to four models with different patch properties and the rows (**1-3**) show different intershocks from the same simulation. The color scale is the same as in Figure 2.5. (**a**) case A. The completed nucleation for all of the events in this simulation looks similar. (**b**) Same properties as case B except $D_p/\tilde{h}_p^* = 1.2$. Nucleation shapes b.1 and b.3 are typical for this model, whereas b.2 is the only one of its kind. (**c**) case B. The three examples given highlight the variation in nucleation shapes for this model. (**d**) case C. Nucleation d.1, with a smaller locked region, is the only one of its kind, as the nucleation for the rest of the events looks like d.2 and d.3. For the events in columns (a-b) there are no locked areas as the nucleation completes, whereas in columns (c-d) part of the patch is still locked. Note that the nucleation size estimate \tilde{h}_p^* for each model is shown by a blue bar, and the boundary between the velocity-weakening and velocity-strengthening region is indicated by black dashed lines.

of smaller nucleation size with increased loading is in line with the findings of *Lapusta et al.* [2000] and *Kaneko and Lapusta* [2008]. In addition, the long-range triggering of events through postseismic slip is consistent with the findings in *Lui and Lapusta* [2016] that neighboring repeating earthquakes interact primarily via postseismic slip, over larger distances than previously assumed.

To gain a more accurate sense of the nucleation sizes for the intershocks in our models, it would be useful to measure the nucleation size directly from the simulation results, but the procedure for how to do so is not obvious. Previous studies have shown that the nucleation estimates developed thus far work well for the more typical scenario of a velocity-weakening patch surrounded by a velocity-strengthening region [e.g., *Chen and Lapusta, 2009*]. In that case, the achieved nucleation size is also easier to measure because the fall-off of slip rates is much sharper, resulting in more clearly defined edges of the nucleation than in our scenario, where both the patches and surrounding seismogenic region are velocity-weakening and accelerating towards failure, albeit on different time scales. In our case, the nucleated area extends outside of the patch, where the properties and thereby the nucleation size is much different (\tilde{h}_m^* is usually 10 or more times larger than \tilde{h}_p^* in our models), and the question remains of how to combine the nucleation length scales measured on and off the patch into a unifying nucleation size estimate. Furthermore, since the nucleation sizes in the mode II and mode III directions differ by a factor of $1/(1 - \nu)$, we have an orientation problem in 3D, unless the nucleated area is perfectly elliptical and lined up with the mode II and mode III slip directions.

Given these uncertainties and variability, we measure a reference length scale for the nucleation size as the largest dimension of the nucleated area in the radial direction within the circular patch, from the log scale slip rate snapshots at the moment the seismic slip rate threshold of 0.1 m/s is reached (defined as the start of the dynamic event). These “nucleation size” measurements typically range from 65% to

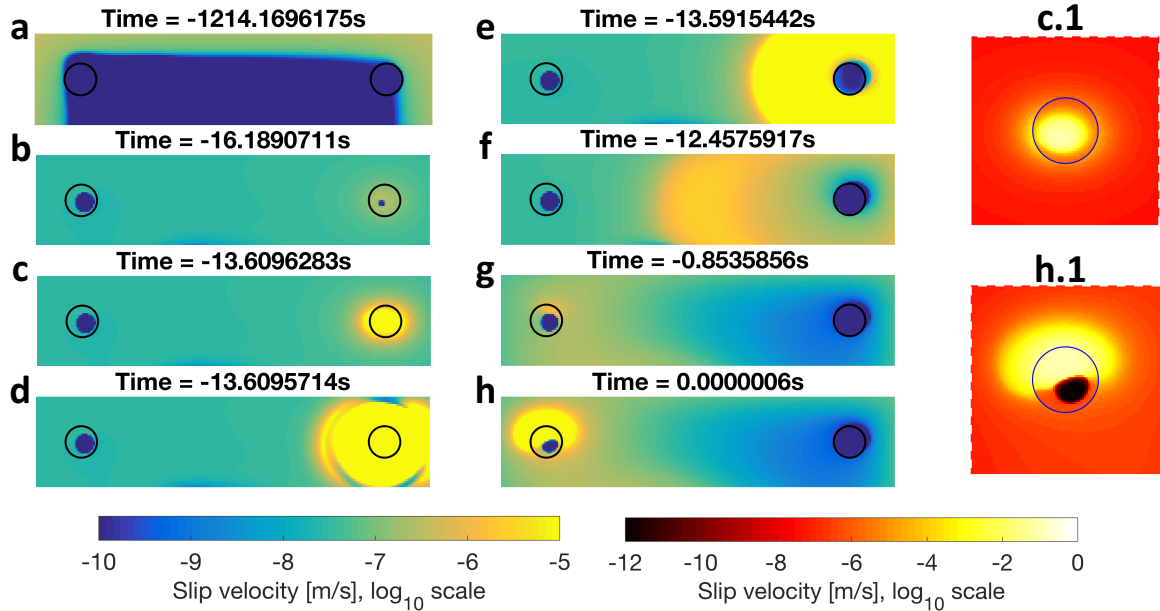


Figure 2.8.: Long-range triggering between intershocks via postseismic slip and resulting variability in intershock nucleation. Postseismic slip from the first intershock (right patch) travels a distance of 8.6 patch diameters between the two and accelerates the nucleation of the second intershock (left patch). **(a)-(h)** Slip velocity on a log scale for a simulation with the same properties as case B, except $D_p/\tilde{h}_p^* = 1.6$: **(a)** Early interseismic period; **(b)-(d)** Intershock nucleation and rupture at the right patch; **(e)-(g)** Resulting postseismic slip traveling to the left patch; **(h)** Triggered intershock nucleation of the left patch. The color scale for snapshots (a)-(h) is cropped to highlight the postseismic front, and the spatial domain shown is restricted to a strip of the seismogenic zone. Time in seconds is given above each snapshot, relative to the start time of the event in (h). **(c.1)** Nucleation snapshot associated with the intershock in (c) (analogous to panels in Figure 2.7). **(h.1)** Same for the intershock in (h). While (c.1) exemplifies regular intershock nucleation for this simulation, (h.1) shows how the accelerated loading from the postseismic slip of the first intershock allows the second intershock to nucleate earlier and with a smaller nucleation size, leaving the center of the patch locked. The patches of higher normal stress in panels (a)-(h), and (c.1) and (h.1) are outlined in black and blue, respectively.

100% of the formulaic nucleation size estimate \tilde{h}_p^* (from Equation 2.4), with values over 100% being unusual; therefore, our patches are more unstable than initially estimated, likely due to part of the nucleation being accommodated by the surrounding background region. A more comprehensive nucleation size calculation would require a weighted combination of the nucleation extents on and off the patch, or perhaps a linear dimension computed from the total nucleating area.

2.5. Rupture extent of foreshocks versus the larger-scale nucleation size

The intershocks presented in this work are, by definition, patch-initiated seismic events that are isolated, i.e., do not turn into mainshocks. Let us further consider the required separation of length scales needed for isolation, where a rearrangement of Equation (2.5) reveals

$$\frac{h_m^*}{h_p^*} = \frac{h_m^* D_r D_p}{D_r D_p h_p^*}. \quad (2.6)$$

For the main set of simulations, the instability ratio D_p/\tilde{h}_p^* is between 0.4 and 2.4 (Section 2.3), the relative rupture extent D_r/D_p is between approximately 1 and 9 (Section 3.2). As previously mentioned (Section 2.2), besides the patch instability ratio D_p/\tilde{h}_p^* and the spacing between the patches, the occurrence of (isolated) intershocks is dependent on the ratio of the mainshock nucleation size to the intershock rupture dimension h_m^*/D_r , which we call the isolation ratio. For a seismic event initiating on a patch to avoid immediately triggering a mainshock, h_m^* must be sufficiently larger than D_r .

The main set of simulations (Table 2.2) provides insight into the values of \tilde{h}_m^*/D_r that result in intershocks, ranging from $\tilde{h}_m^*/D_r \approx 31$ for the smallest events to $\tilde{h}_m^*/D_r \approx 1$ for the largest events (Figure 2.9a), with most values of \tilde{h}_m^*/D_r between

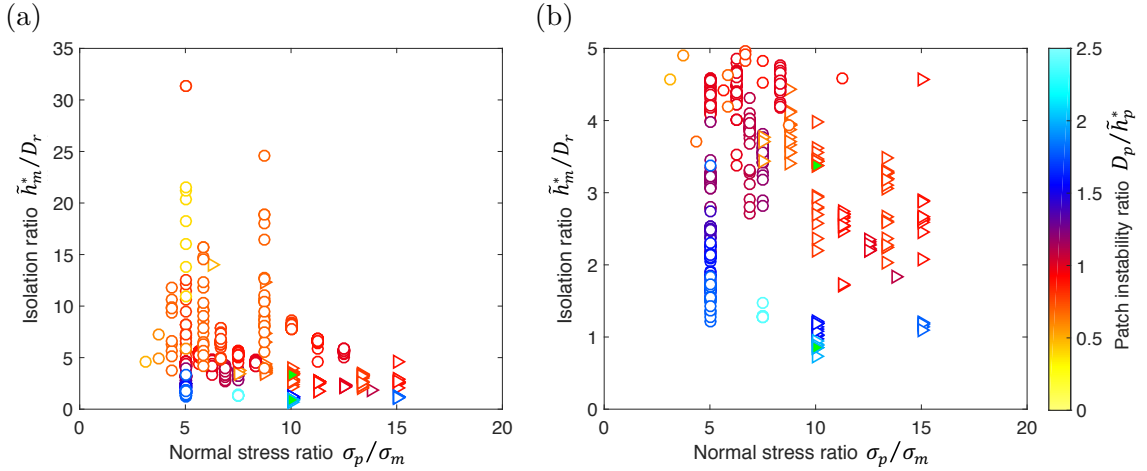


Figure 2.9.: Isolation ratio \tilde{h}_m^*/D_r for the main set of models. The data and marker identity scheme correspond to Figure 3.1. The two intershocks indicated by green-filled markers are analyzed further in Figure 2.10. (a) Values for all intershocks. The highest point, $\tilde{h}_m^*/D_r = 31.33$, is for an intershock that only partially ruptured the patch, i.e., $D_r/D_p < 1$, as seen in Figure 3.4a. (b) Same data as in (a) but zoomed into the isolation ratios between 0 and 5.

≈ 2 and 10. As expected, the lowest isolation ratios occur for the models with the highest patch instability ratios D_p/\tilde{h}_p^* (also the largest patches), as patches in these models have the most potential for initiating powerful ruptures. Interestingly, many of the corresponding isolation ratios are close to 1 and some are even slightly below 1 (Figure 2.9b), meaning that ruptures with D_r greater than but close to \tilde{h}_m^* can still avoid growing into a mainshock.

The unexpected observation of $\tilde{h}_m^*/D_r \approx 1$ still allowing for isolated intershocks in certain cases merits an investigation. We find that this occurs when the intershock is initiated early in the nucleation process, before a sufficiently large portion of the velocity-weakening region is loaded enough to be ready for a mainshock, making the stress distribution at the start of the intershock unfavorable for rupture growth; then seismic events with rupture extent D_r close to \tilde{h}_m^* can still arrest. Figure 2.10 provides a map of the ruptured area and both the slip rate V and shear stress τ at the start of the seismic event for an example of an intershock with $\tilde{h}_m^*/D_r < 1$. In this example, it is apparent that the low shear stress in the locked portion of the

fault, due to the previous mainshock, creates unfavorable conditions that stunt the rupture (Figure 2.10), preventing the event from growing into a mainshock. Thereby, \tilde{h}_m^*/D_r can be about 1 and still allow for intershocks but cannot be much smaller – $\tilde{h}_m^*/D_r = 0.74$ is the smallest that we have seen in our main set. Furthermore, in terms of their timing, the most foreshock-like events would occur in the later stages of the protracted nucleation of the mainshock, and therefore require a higher isolation ratio, significantly larger than 1.

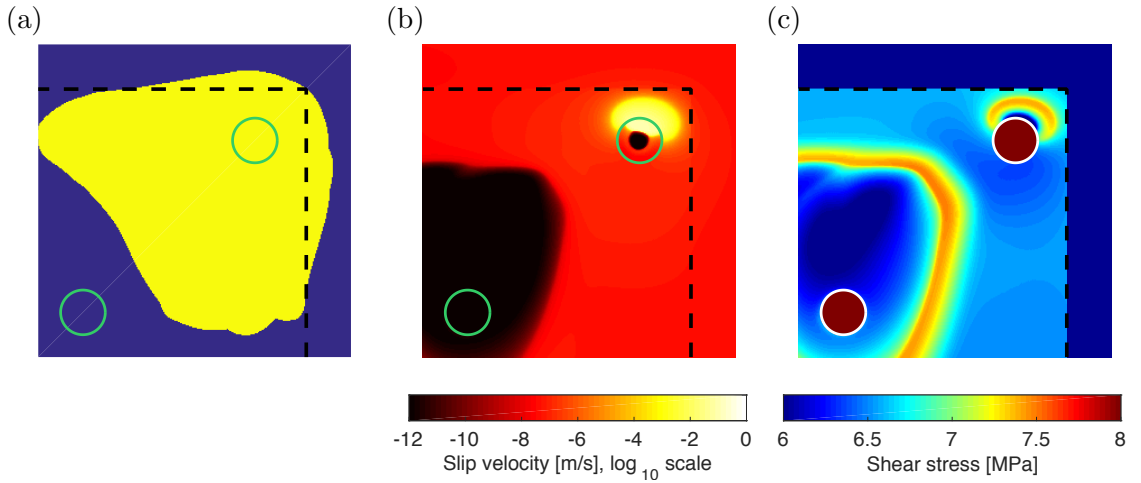


Figure 2.10.: Intershock rupture extent and initiation conditions for one case of low isolation ratio \tilde{h}_m^*/D_r . **(a)** The ruptured area of the event (yellow). **(b)** Snapshot of the slip velocity on a log scale. **(c)** The shear stress at the start of the intershock. The fault model has the same properties as case A (σ_p/σ_m , L_p/L_m , $\tilde{h}_m^*/\tilde{h}_p^*$), except the patch diameter is 2.5 times larger and, consequently, the patch instability ratio D_p/\tilde{h}_p^* is 2.0 instead of 0.8, and has $\tilde{h}_m^*/D_r = 0.85$. The color scale for the shear stress snapshot is cropped to highlight the fall-off in stress from the creeping section to the locked middle portion of the fault. In all subplots, the boundary between the velocity-weakening and velocity-strengthening region is indicated by a black dashed line, and the circular patch is outlined for clarity.

While the dependencies are difficult to express analytically, we suspect that the isolation ratio h_m^*/D_r for producing intershocks that are fully isolated from the upcoming mainshock is most strongly dependent on the following three factors: (1) the instability ratio of the patch D_p/h_p^* , where higher instability ratios generally correspond to more dramatic ruptures that can more strongly perturb the surrounding

region, thereby reducing the background nucleation size h_m^* ; (2) the instability ratio of the background seismogenic region W_{VW}/h_m^* , which indicates how easy it is to instigate dynamic rupture on a larger scale; and (3) the pre-intershock state of shear stress on the fault, which is a combination of the stress left over from previous events and the loading from the creeping region (e.g., Figure 2.10). Additional factors that can influence the stress state at the start of the event and thereby the h_m^*/D_r through D_r are the spacing between patches and the interaction between sequential intershocks via postseismic slip, but these two factors are beyond the scope of this study.

Recalling section 2.2 and Equation (2.6), the core of the separation of length scales is the separation between the nucleation size of the intershocks h_p^* and the nucleation size of the mainshocks h_m^* . The separation ratio $\tilde{h}_m^*/\tilde{h}_p^*$ for all of the models in both the main set and VBNS set fall between 6 and 25. However, as discussed in Section 2.3, two of the models did not produce intershocks. In particular, the case with sub-seismic patches had $\tilde{h}_m^*/\tilde{h}_p^* = 10$ (yellow filled-in triangle in Figure 2.3), and the case with overly strong patches had $\tilde{h}_m^*/\tilde{h}_p^* = 15$ (purple filled-in triangle in Figure 2.3). Clearly, more than just the nucleation size separation ratio must be considered in order to reliably predict the patterns of fault behavior.

2.6. Exploration of mainshock triggering by patch-initiated events

In an effort to further investigate the conditions needed for intershocks and mainshocks to occur within the same fault model, here we explore the lower limits of scale separation, specifically, cases in which patches produce events comparable to the nucleation size of the mainshock which may or may not remain isolated. To do so, we discuss the simulation results for a set of models in which the background normal

stress σ_m is decreased while the patch properties are maintained (σ_p , D_p , L_p , and thereby \tilde{h}_p^* and D_p/\tilde{h}_p^*), so that the separation ratio $\tilde{h}_m^*/\tilde{h}_p^*$ is systematically increased (Table 2.5). Initially designed to explore the effect of increasing $\tilde{h}_m^*/\tilde{h}_p^*$, the set is not quite suitable for this purpose, as the background instability ratio $W_{\text{VW}}/\tilde{h}_m^*$ simultaneously decreases, making it increasingly difficult for mainshocks to nucleate. Nonetheless, the models provide interesting insight regarding the potential of the largest intershocks to trigger larger-scale mainshocks versus remain isolated. We call this group the transition set, with the individual model named case T1-T6 (Table 2.5). The results presented here, especially case T1 and T2, also provide a scenario for suppressing intershocks with immediate triggering of the mainshock. In this situation, the patches have properties that are conducive for hosting seismic events but, when the patch ruptures, the rupture extent is too close to the background nucleation size, causing the seismic event to grow into a mainshock. This third example is in addition to the scenarios of (1) overly strong patches and (2) sub-seismic patches discussed in section 2.3 in reference to Figure 2.3.

The transition set has the same properties as the Variable Background Normal Stress (VBNS) set (Table 2.1, and Table 2.3), except the patches are larger ($D_p = 16$ cm) such that the patch instability ratio is $D_p/\tilde{h}_p^* = 3.2$ instead of 1.2. In the base model of this set, case T1, all patch-initiated seismic events instantly grow into mainshocks. As this pattern is not shared by the parallel model in the VBNS set, the higher patch size D_p , patch instability ratio D_p/\tilde{h}_p^* , and resulting higher relative rupture extents D_r/D_p (Figure 3.10c) in case T1 allow for immediate triggering of the mainshock. As the background instability is decreased in the subsequent transition set models, more complex behavior is observed.

The first two models (cases T1 and T2) produce no intershocks and the last two models (cases T5 and T6) are capable of producing multiple intershocks in the same mainshock cycle. In contrast, most intershocks rupturing an entire circular patch in

the intermediate two models (cases T3 and T4) are soon followed by a mainshock. Based on these qualitative observations, we divide the level of separation displayed by the individual events in the transition set simulations into three categories: (1) immediate triggering – full blending of a patch-initiated seismic event into a mainshock (Figure 2.11a), (2) delayed triggering – borderline isolation between the intershock and subsequent mainshock (Figure 2.11b), and (3) separated – full isolation between the intershock and mainshock (Figure 2.11c). The description of the levels of separation presented here is in line with our focus on the separation between intershocks and mainshocks, however, similar behaviors could also be observed in the interaction among intershocks.

Table 2.5.: Parameters for the individual models of the transition set. The descriptors listed in the last column are explained further in the text. Note that the properties listed in the second through the sixth column are also identical to those of the six models in the VBNS set.

Model name	σ_m [MPa]	σ_p/σ_m	\tilde{h}_m^* [m]	W_{vw}/\tilde{h}_m^*	$\tilde{h}_m^*/\tilde{h}_p^*$	Immediate triggering
Case T1	10.00	5	0.5	2.00	10	Always
Case T2	8.34	6	0.6	1.67	12	Always
Case T3	7.15	7	0.7	1.43	14	Intermediate
Case T4	6.25	8	0.8	1.25	16	Intermediate
Case T5	5.56	9	0.9	1.11	18	Sometimes
Case T6	5.00	10	1.0	1.00	20	Sometimes

Within the long-term simulation for a given fault model, the individual seismic events can span all three categories of separation. As the delayed triggering and separated categories, by definition, correspond to a higher level of event isolation than for the immediate triggering case, one way to classify the behavior of a fault model over the entire simulation is to assess how often patch-initiated events immediately trigger the mainshock. The last column in Table 2.5 describes simulations from the transition set by this perspective. In one end-member case, patch-initiated seismic

events always seismically grow into mainshocks (e.g., case T1), whereas simulations on the other side of the spectrum only sometimes (e.g., case T5), or in the end-member case, never, produce events starting on patches that continue as mainshocks (e.g., most if not all of the simulations in the main set). The scenario of delayed triggering for every mainshock is somewhat of a gray-area, so we label it as “intermediate” in Table 2.5, as this behavior highlights the boundary between events beginning as intershocks always and sometimes blending into the upcoming mainshock.

While seismic events in our simulations are defined based on our seismic velocity threshold of 0.1 m/s, for cases T3 and T4, it is clear from the slip velocity snapshots that the typical intershocks and following mainshocks are part of the same accelerated slip event, providing examples of delayed triggering. In particular, for an example from case T3, the event starts by rupturing a patch and then the slip decelerates enough (to approximately 7×10^{-4} m/s) to dip below the threshold briefly before accelerating again and continuing the event as a mainshock that ruptures the larger-scale seismogenic zone (Figure 2.11b), suggesting that the intershock and mainshock are strongly linked.

cases T5 and T6 both produce multiple intershocks in the same cycle, but case T5 has the most variety in style of intershocks and typically 3 or 4 per mainshock cycle. In this simulation, some of the mainshocks are connected to the last intershock by a similar deceleration effect as for the lower-level isolation, with maximum slip rates on the fault dipping down to the order of 10^{-5} to 10^{-3} m/s. For other mainshocks, the maximum slip rate returned to the background creeping rate of 4×10^{-8} m/s after the preceding intershock (e.g., Figure 2.11c).

Given the constant absolute patch parameters for this set of models, the resulting intershocks typically have similar values of relative rupture extent D_r/D_p , almost always in the range of 4.0 to 5.0. If we compare the respective background nucleation sizes \tilde{h}_m^* to the rupture extent D_r , using the common rupture ratio of approximately

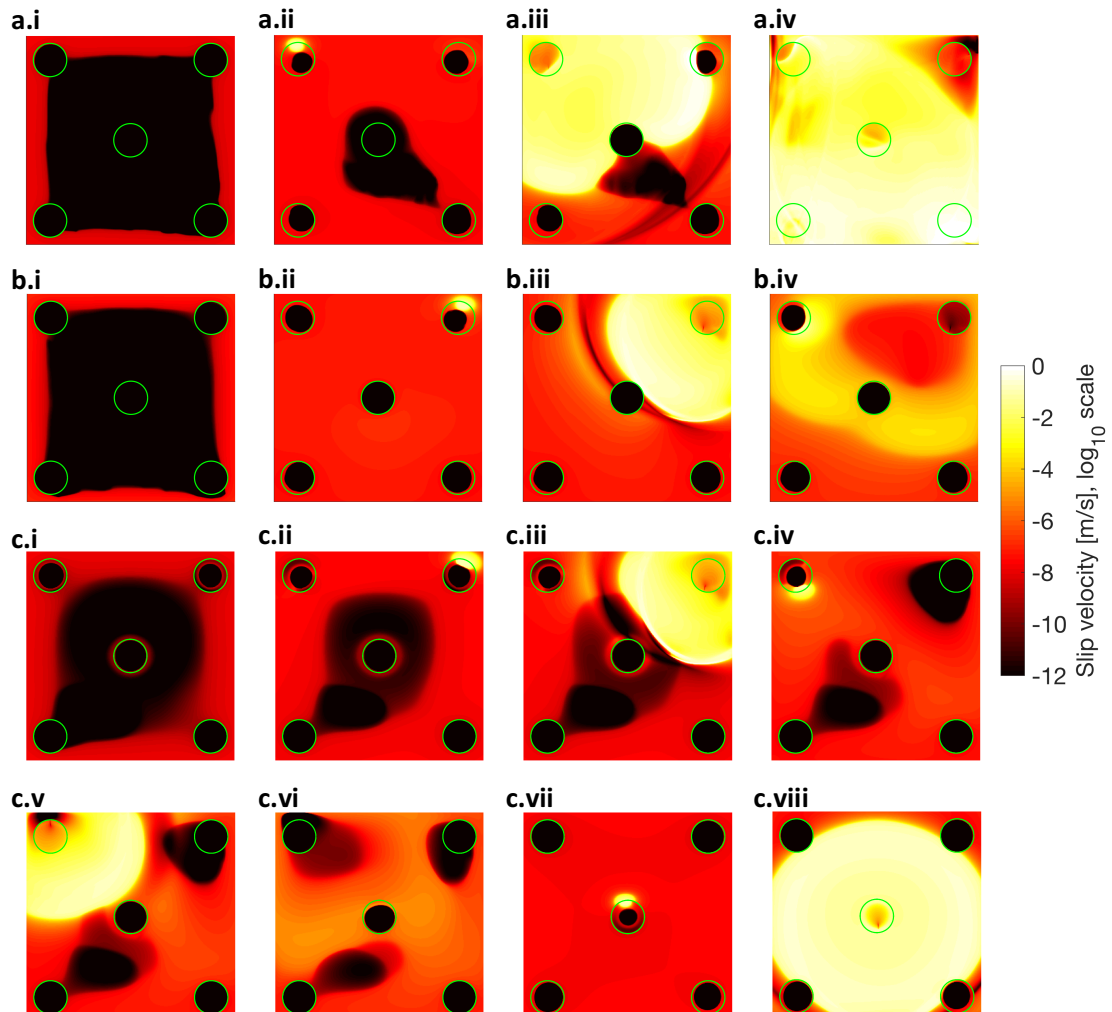


Figure 2.11.: Snapshots of slip velocity for examples of the three categories of separation between intershocks and mainshocks from the transition set of models. Each panel plots slip velocity over the velocity-weakening region on a log scale with the same color scale as Figure 2.5, with the circular patches outlined in green. **(a)** Immediate triggering: patch-initiated rupture grows into a mainshock (case T1). **(b)** Delayed triggering: intershock is followed by a mainshock, linked by the accelerated postseismic slip from the intershock (case T3). **(c)** Separated: after a sequence of intershocks, slip rates return to background rates before the mainshock begins (case T5). **(a.i)** Early interseismic period. **(a.ii)-(a.iv)** Initiation and rupture of mainshock. **(b.i)** Early interseismic period. **(b.ii)-(b.iii)** Initiation and rupture of intershock. **(b.iv)** Initiation of mainshock. Note the elevated postseismic slip rates left over from the intershock. The time difference between the seismic initiations in (b.ii) and (b.iv) is approximately 6 times longer than the duration of the mainshock. **(c.i)** Quiescence after the previous intershocks in this cycle. **(c.ii)-(c.iii)** Initiation and rupture of an intershock. **(c.iv)-(c.vi)** Initiation, rupture, and postseismic slip of the following intershock. **(c.vii)-(c.viii)** Initiation and rupture of the mainshock.

4.5, the isolation ratios \tilde{h}_m^*/D_r for cases T3-T6 are approximately 1.0, 1.1, 1.3, and 1.4, respectively. These values show that the difference in isolation ratio between the case of single intershocks and consecutive intershocks for the parameter range of the transition set is small, as further supported by the observation that even some mainshocks from the simulations with consecutive intershocks are only moderately separated from the previous intershock. Recalling the isolation ratios \tilde{h}_m^*/D_r reported for the main set (Figure 2.9), the lowest observed values of \tilde{h}_m^*/D_r in all sets so far that produce any intershocks is around 1. In order for our fault models to allow an intershock to be followed by another intershock, an isolation ratio of approximately 1.3 is needed for the transition set, which closely matches to the typical lower bound of 1.2 for the main set. In addition, the lowest observed instability ratio \tilde{h}_m^*/D_r for a single intershock is approximately 1 for the transition set (case T3), which is higher than the lowest \tilde{h}_m^*/D_r of 0.74 in the main set, providing further evidence that the patch instability ratio has an important influence on the potential for smaller-scale events that remain isolated.

One of the most interesting findings from this set of simulation is the phenomenon of a mainshock initiating over a length scale (approximately \tilde{h}_p^*) that is significantly smaller than its nucleation size \tilde{h}_m^* and proceeding to re-rupture a large area that was quasi-statically slipping during the nucleation (e.g., Figure 2.11a.i-a.iv). The features inherent to the transition set – significant heterogeneity provided by the patches in combination with the particularly low background instability ratio W_{VW}/\tilde{h}_m^* – make it difficult for the mainshock to nucleate on its own, hence, causing elevated rates of quasi-static slip over the majority (if not all) of the background velocity-weakening region (e.g., Figure 2.11b.ii). Then, when a potential intershock nucleates at one of the patches it can grow to the mainshock size, passing through the mainshock nucleation size along the way and re-rupturing the background region. This process can potentially explain the observations of the so-called “seismic nucleation phase” [Ellsworth

and Beroza, 1995], which is characterized by slow moment release at the start of the seismic event, and it is consistent with the Landers earthquake re-rupturing its foreshock area [*Dodge et al., 1995*]. Furthermore, the case of delayed triggering of the mainshock (i.e., a large foreshock before the mainshock that leaves behind slip at high quasi-static rates as the mainshock initiates, as seen in Figure 2.11b.iv) provides an even more intense example of this re-rupturing, and has the potential to cause the longest duration of the seismic nucleation phase.

3. Unexpectedly reasonable stress drops and the underlying rupture mechanics

Building on the models described in Chapter 2 that maintain a sufficient separation in length scales to host two scales of seismicity on the same fault, this chapter explores the stress drops of the resulting smaller-scale seismicity (intershocks). We find that, despite the highly-elevated compression assigned to the source patches, these foreshock-like events have reasonable stress drops, within the typically observed range of 1-10 MPa. This chapter presents the stress drops calculated for the asperity-type events and explores the underlying mechanics that lead to these reasonable and approximately constant stress drops, namely the intershocks rupturing significantly into the surrounding region, the aseismic stress release just prior to the start of the seismic event, and the heterogeneous distribution of shear stress change over the ruptured area. The chapter concludes with the derivation of a simplified stress drop calculation based on these findings, which further aids in understanding the reasonable stress drops.

This chapter is based on the second part of the manuscript in final stages of preparation, entitled, “Microseismicity on patches of higher compression during larger-scale

earthquake nucleation in a rate-and-state fault model” by Natalie Schaal and Nadia Lapusta.

3.1. Stress drops of intershocks

Section 2.4 provides examples of intershocks that have successfully nucleated on the circular patches of higher compression within the seismogenic zone. However, the question remains: do these smaller-scale seismic events have realistic stress drops in the range of what is observed? Based on the proportionality between the shear stress and normal stress through the friction coefficient, one would expect the stress drops to scale linearly with the normal stress and hence expect unreasonably high stress drops for the seismic events initiating on the patches of highly elevated normal stress. Calculating the slope for the expected trend in stress drops using the average mainshock stress drop from the 10 mainshocks in the homogeneous fault simulation (discussed in Figure 2.4a) divided by the background normal stress σ_m yields 0.20 for our main set of simulations.

Unexpectedly, our simulations show that the intershocks have near-constant stress drops, nearly independent from the patch normal stress, for a wide range of patch parameters (Figure 3.1). The computed stress drops have reasonable values, consistent with the typical range of 1-10 MPa from the lab [*McLaskey et al., 2014*] and the field [*Abercrombie, 1995*]. We compute the stress drops $\overline{\Delta\tau}^{\text{SD}}$ for the simulated events from their seismic moment M_0 and effective rupture radius $r = \sqrt{A_r/\pi}$, where A_r is the rupture area, using the standard expression for a circular crack model [*Eshelby, 1957; Kanamori and Anderson, 1975*]:

$$\overline{\Delta\tau}^{\text{SD}} = \frac{7}{16} \frac{M_0}{r^3}. \quad (3.1)$$

Note that the superscript “SD” here refers to the “stress drop,” which is a positive

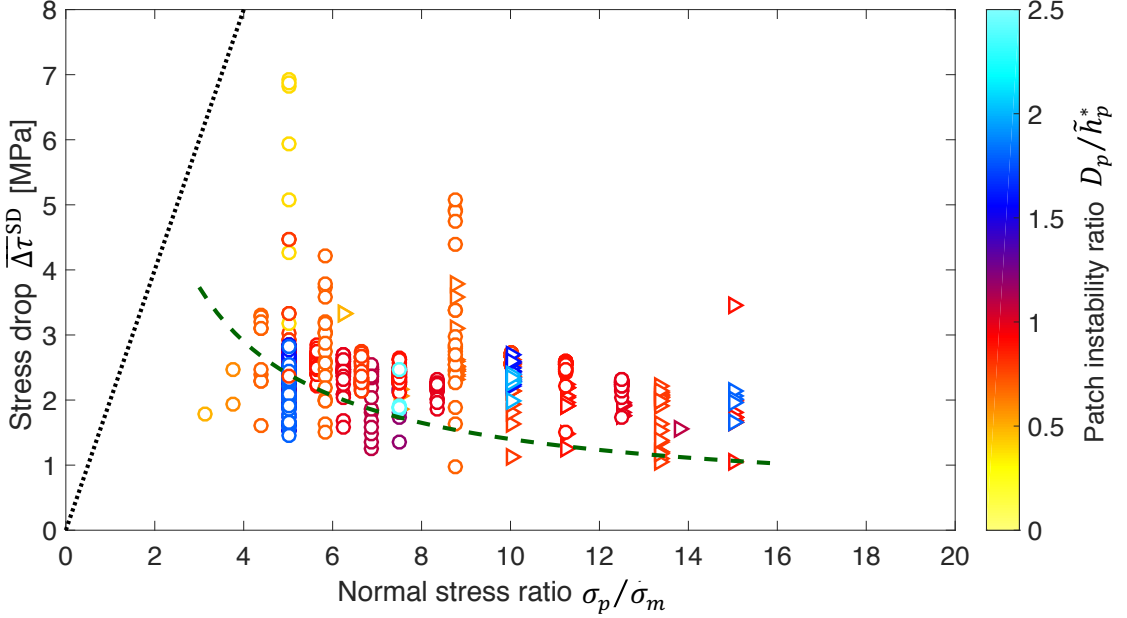


Figure 3.1.: Stress drops of intershocks as a function of the patch normal stress. For this set of models, the background properties (σ_m , L_m , a , and b) are kept constant and each simulation is run for the same simulated time, which typically produces 10 mainshocks cycles. Each marker represents an intershock, while each combination of outline color, marker type, and normal stress ratio σ_p/σ_m identifies a model. The outline color indicates the instability ratio of the patch D_p/\tilde{h}_p^* , with respect to the nucleation size estimate \tilde{h}_p^* (Equation 2.4). Circular markers indicate $L_p/L_m = 1/2$, whereas triangular markers indicate $L_p/L_m = 1$. The vertical spread in markers with the same identifying properties shows the range of stress drops observed for a given simulation with multiple intershocks. The black dotted line and the green dashed line show the approximate expected trend of $\overline{\Delta\tau}^{\text{SD}} = 0.2\sigma_p$, and the simplified stress drop calculation ($\overline{\Delta\tau}_a^{\text{SD}}$, Equation 3.5), respectively. The stress drops of the intershocks in our models are in the reasonable range of about 1-7 MPa and approximately constant, despite the range of variation in the patch normal stress.

quantity that represents the average difference in the shear stress before and after the event. The stress drops are computed using quantities estimated directly from our on-fault distributions and, in that sense, correspond to the actual (meaning an on-fault quantity instead of one inferred at a distance) stress drops. In Chapter 4, we will compare these values to the estimates obtained from the seismograms by typical seismological approaches.

In addition, note that the two simulations with the widest spread in the stress drops in Figure 3.1 (yellow and orange circles with $\sigma_p/\sigma_m = 5.00$ and 8.75 , respectively) have low instability ratios, resulting in events that just barely qualify as seismic, i.e., reach the slip rate of 0.1 m/s. This spread may indicate a sensitivity of the rupture area to the chosen seismic velocity threshold for these barely seismic events.

As initially mentioned in Section 1.2.2, our definition of any seismic quantity (including moment M_0 , rupture area A_r , etc., and quantities derived from these properties), is based on the criterion of the slip velocity V meeting or exceeding the threshold of 0.1 m/s. Our results may depend on the choice of this velocity threshold, however, the value that we are using is the current standard. We expect that our results under another reasonable value of the seismic velocity threshold would still be qualitatively the same, despite any potential quantitative differences. The exploration of velocity thresholds as well as other types of criteria for defining the realm of seismic behavior is an interesting topic for future work.

The stress drop value, given by Equation (3.1), is meant to be representative of the average distributed shear stress change over the entire seismically ruptured area. As can be seen from plotting the shear stress change over the fault for an inter-shock (Figures 3.2a-3.2b), the shear stress change over the ruptured area is quite heterogeneous, with most of the significant decrease in stress occurring within a close neighborhood in and around the patch. (Note that, in Figure 3.2, we plot stress changes in a more traditional sense: final values minus initial values, which makes

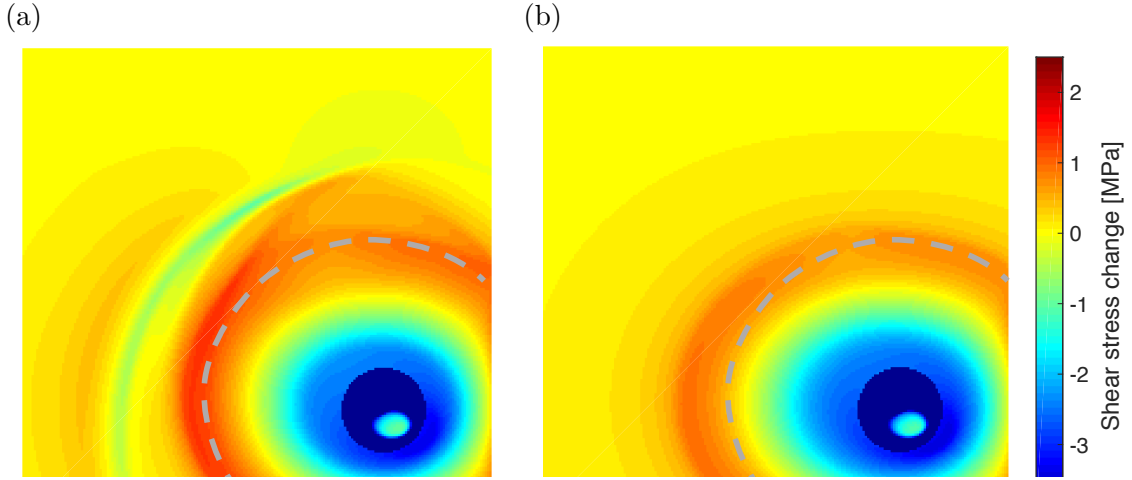


Figure 3.2.: Example of shear stress change due to an intershock. **(a)** Spatial distribution of shear stress change due to seismic slip for an intershock from case B. The plot is spatially cropped to one quarter of the seismogenic region, and the color scale is chosen to highlight the stress changes outside of the patch. Blues and greens show decreased stress, yellow corresponds to near-zero stress changes, and reds and oranges show increased stress. The patch with elevated normal stress is shown by the mostly dark blue saturated circle. The approximate rupture extent for this event is outlined by the gray dashed line, defined by the area that reaches or exceeds the seismic velocity threshold of 0.1 m/s. **(b)** The same event, color scale, and dashed rupture line as in (a), but the shear stress change is computed using the stress distribution at the time after the event when the seismic waves have left the area. The additional time that has elapsed for (b) compared to (a) is approximately 1.8 times the intershock duration and incorporates the effects of initial postseismic slip.

negative stress changes correspond to positive stress drops). In addition, there is some stress increase within the ruptured area, near where the rupture arrests. These distributed stress changes are combined as a weighted average into the stress drop $\overline{\Delta\tau}^{\text{SD}}$ of Equation (3.1). As proven in the work of *Madariaga* [1979], $\overline{\Delta\tau}^{\text{SD}}$ represents the average of the stress drop distribution weighted by the final slip distribution of a constant-stress-drop source model. Such a quantity is the most consistent value to compare to the seismological estimates of stress drops, which also use Equation 3.1, with the seismic moment M_0 and effective rupture radius $r = \sqrt{A_r/\pi}$ estimated from the far-field seismograms, as explained in Chapter 4.

The next two sections, 3.2-3.3, explore the key factors that lead to the unexpectedly

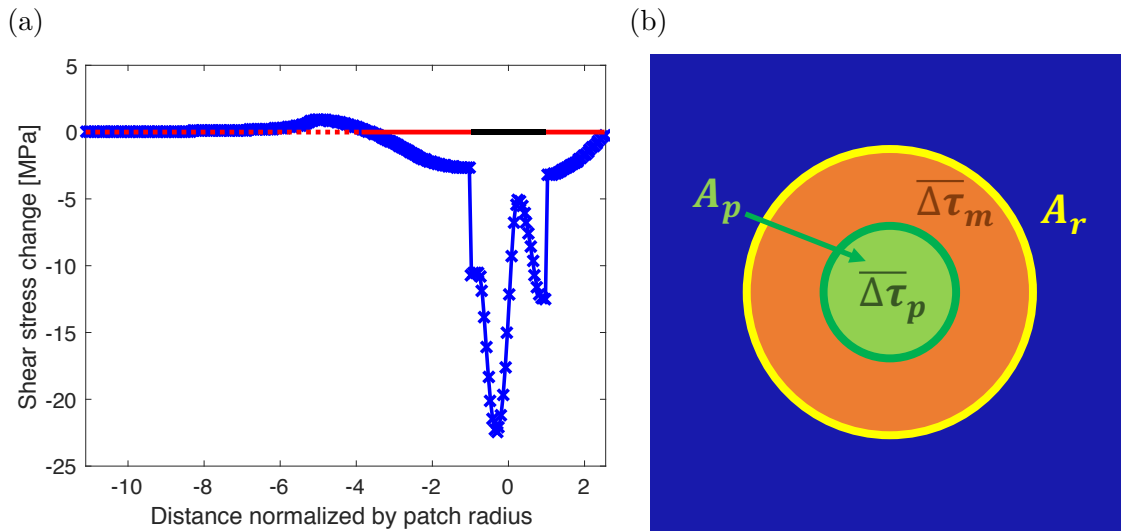


Figure 3.3.: Shear stress changes that are used to derive the simplified stress drop calculation. **(a)** Horizontal profile of the shear stress change for an intershock from case B (featured in Figure 3.2a) through the middle of the ruptured patch, shown as a blue line. The qualities of the horizontal line drawn at $y = 0$ indicate whether or not the points for the given part of the profile ruptured in the intershock: dotted red for the unruptured region, solid red for the ruptured area outside of the patch, and solid black for the ruptured area within the patch. **(b)** Diagram of the quantities required for calculating the simplified average stress drop $\overline{\Delta\tau_a}^{\text{SD}}$, including the average shear stress change on the patch $\overline{\Delta\tau_p}$ and off the patch $\overline{\Delta\tau_m}$, the area of the patch A_p , and the total ruptured area A_r . For the featured event, $\overline{\Delta\tau_p} = -10.06$ MPa, $\overline{\Delta\tau_m} = -0.76$ MPa, $D_r/D_p = 3.27$, and the average moment-based stress drop $\overline{\Delta\tau}^{\text{SD}}$ is 2.33 MPa.

reasonable and approximately normal-stress-independent stress drops, namely the extended rupture area of the intershocks and the aseismic stress release on the patches [Higgins and Lapusta, 2017]. Then, in Section 3.4, we propose a simplified model for estimating the stress drops of intershocks based on reasoning about the seismic stress changes on and off the patch (Figure 3.3), along with parameters derived from the trends in our simulation results.

3.2. Extended rupture area

One might expect that the rupture area of an intershock would be similar to the area of the patch. Instead, we observe that the intershocks can rupture far into the surrounding area (e.g., Figure 2.1, Figure 3.2a), with the rupture extent D_r depending on the properties of the patch and surrounding area (Figure 3.4). With the value of the background normal stress σ_m kept constant for this set of simulations, we find an approximately linearly increasing trend in the relative rupture extent D_r/D_p with respect to the patch normal stress σ_p (Figure 3.4, discussed further in Section 3.4). This behavior also has important sub-dependencies. For example, models with no L variation (triangles) or higher instability ratios (blue) have a larger relative rupture extent. Still, the overarching trend is what significantly contributes to moderating the stress drops: the higher the normal stress is on the patch, the relatively further the intershock rupture extends into the surrounding region. This surrounding region enters the average stress computation, yet experiences much lower stress changes that range from mild shear stress decreases (positive stress drops) to stress increases (negative stress drops) (Figure 3.2), thus helping to keep the (average) stress drops $\overline{\Delta\tau}^{\text{SD}}$ down (Equation 3.1).

In addition to the dependence on the elevated patch normal stress, the rupture extent should be determined by the response of the surrounding region to the stress

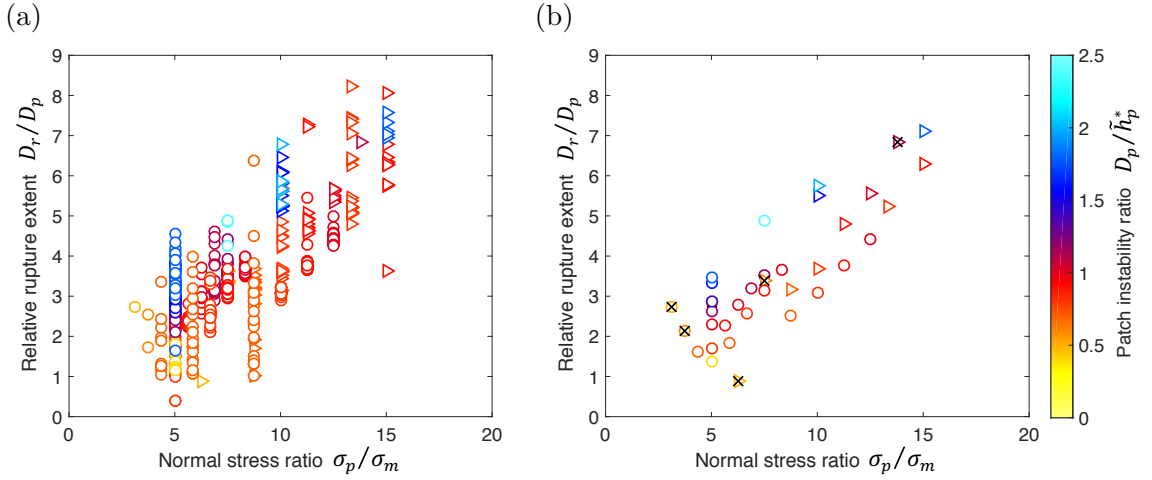


Figure 3.4.: Effect of the patch normal stress on the rupture extent. **(a)** Relative rupture extent values (effective diameter of ruptured area D_r normalized by the patch diameter D_p) corresponding to each data point in Figure 3.1, with the same identity scheme. A linear best fit line through the origin has slope γ of approximately 0.41. **(b)** Median values for each simulation in subplot (a), following the same identity scheme. Median markers for simulations with three or fewer intershocks are indicated by a black “x”. The relative rupture extent is approximately linearly dependent on the normal stress ratio σ_p/σ_m on the patch, although it is also affected by the instability ratio D_p/\tilde{h}_p^* (outline color) and characteristic slip ratio L_p/L_m (marker shape). The overall trend results in moderate stress drops $\overline{\Delta\tau}^{\text{SD}}$, even for highly compressed patches.

change from the expanding seismic event. The (mostly) stress decrease over the rupture area (Figure 3.2a) is balanced by a stress increase over the rest of the fault, decaying away from the edge of the event [e.g., *Kaneko et al., 2010*]. One can potentially determine D_r/D_p by considering the stress change “balance” over the fault, however, the stress change profiles differ from one case to another beyond the qualitative features discussed here (Figure 3.3a) and hence cannot be readily represented analytically.

3.3. Aseismic stress release

In addition to rupturing into the surrounding region, another contributing factor to the reasonable intershock stress drops is aseismic shear stress release. Patches close to

their own nucleation size can relieve a significant amount of their shear stress through aseismic slip, closely before the start of the seismic event (e.g., Figure 2.6, row D). This aseismic release is not included in the (seismic) stress drop $\overline{\Delta\tau}^{\text{SD}}$ calculation. The associated aseismic slip occurs due to the intershock nucleation process and can be quite significant. It was previously observed in models of velocity-weakening patches within a velocity-strengthening surrounding [e.g., *Chen and Lapusta, 2009; Lui and Lapusta, 2016*].

To further investigate this phenomenon, we define the average aseismic stress change to be the shear stress at the start of the seismic event minus the shear stress when the average shear stress is largest (before the event), averaged over the patch. Analogously, we define the average seismic stress change $\overline{\Delta\tau}_p$ as the shear stress on the patch at the end of the seismic event minus that at the start of the seismic event, averaged over the patch (Figure 3.3b). The average total stress change is then the sum of the average seismic and aseismic change for a given event. Whenever we report on values for the average seismic, aseismic, or total stress change, we only include intershocks that involve the entire patch to ensure that the average seismic and aseismic stress change are computed over the same patch area. While most of the simulated intershocks have more average seismic stress change than aseismic, some events have similar values of average seismic and aseismic, or even more average aseismic than seismic stress change (Figures 3.5-3.8).

It is reasonable to expect that the proportion of average stress change that is aseismic depends on the instability ratio (with one end-member case being a patch that is too small to ever produce seismic events such that all of its stress change is aseismic, e.g., *Chen and Lapusta [2009]*). Our results show that the fraction of stress relieved seismically is indeed dependent on patch instability ratio D_p/\tilde{h}_p^* , with the seismic fraction increasing, overall, with increasing patch instability ratio (Figure 3.6a), as expected.

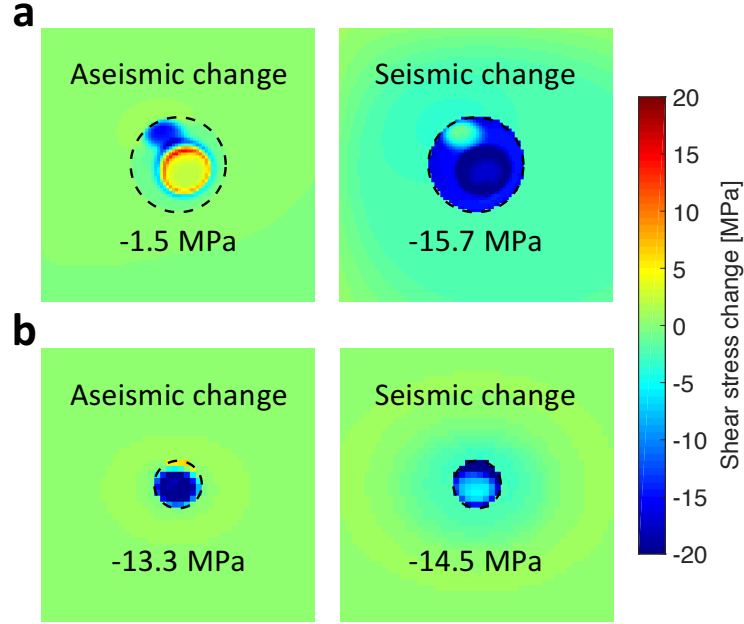


Figure 3.5.: Average aseismic and seismic stress change on the patches, which are outlined with a black dashed line. **(a)** Spatial distribution of aseismic and seismic stress change for event d.2 in Figure 2.7 (case C), labeled with values of the average aseismic and seismic stress change averaged over the patch. **(b)** Same for event a.3 in Figure 2.7 (case A).

For relative rupture extents D_r/D_p around 3.0 and above, widening stripes of constant seismic fraction (Figure 3.6b) for similar patch instability ratio D_p/\tilde{h}_p^* (outline color), regardless of characteristic slip distance ratio L_p/L_m (shape), imply that the seismic fraction is mostly determined by D_p/\tilde{h}_p^* for high enough D_p/\tilde{h}_p^* . We interpret this to reflect the stronger sensitivity of intershocks to the surrounding conditions, i.e., slip history, when initiating on patches that are less prone to instability. This influence creates more variability in the dynamics of the events, and thereby a wider range of the resulting seismic fractions for patches with lower instability ratio, and a tighter range for patches with higher instability ratio.

The dependence of average aseismic versus seismic stress change on the instability ratio is additionally influenced by the choice of properties assigned to the patch. Models with patches that have the same size D_p and instability ratio D_p/\tilde{h}_p^* , but for which the same nucleation size \tilde{h}_p^* is achieved by doubling both σ_p and L_p , produce

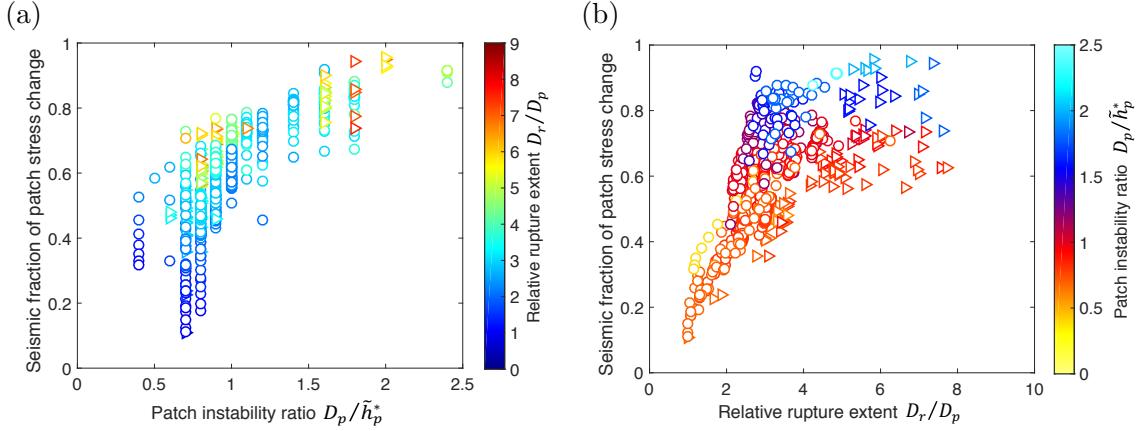


Figure 3.6.: Seismic fraction of average shear stress change on the patch, i.e., the ratio of the average seismic stress change to the total one. As the patch instability ratio D_p/\tilde{h}_p^* increases, the total average shear stress change transitions from being mostly aseismic to mostly seismic. **(a)** The dependence of the average seismic stress change fraction on the patch instability ratio. Unlike Figure 2.3, 3.1, and 3.4, the symbol color indicates relative rupture extent D_r/D_p . Since intershocks within the same simulation can produce different rupture extents, intershocks from the same simulation are no longer represented by the same color. **(b)** Seismic average stress change fraction versus relative rupture extent, colored by the patch instability ratio. The set of models as well as the identity scheme in this figure is the same as in Figure 3.1.

intershocks with a larger fraction of seismic stress change (Figure 3.7a). The factor by which the typical seismic fraction of average stress change goes up for models with doubled σ_p and L_p to maintain the same \tilde{h}_p^* decreases overall for increasing D_p/\tilde{h}_p^* (Figure 3.7b), again indicating that the seismic fraction is mostly determined by D_p/\tilde{h}_p^* for high enough D_p/\tilde{h}_p^* . For cases where the instability ratio D_p/\tilde{h}_p^* is low enough, the increase in seismic fraction with increasing patch normal stress σ_p can even flip whether the seismic or aseismic stress release is dominant.

Both the average seismic stress change $\overline{\Delta\tau_p}$ (Figure 3.8a) and total stress change (Figure 3.8b) on the patch for the simulated intershocks increase in magnitude with the increasing normal stress σ_p on the patch (recalling that σ_m is held constant). This is in line with the physical intuition that the shear stress changes should be proportional to the normal stress on frictional interfaces. As such, this intuition indeed applies to the patch, but not to the entire seismic event, which includes both

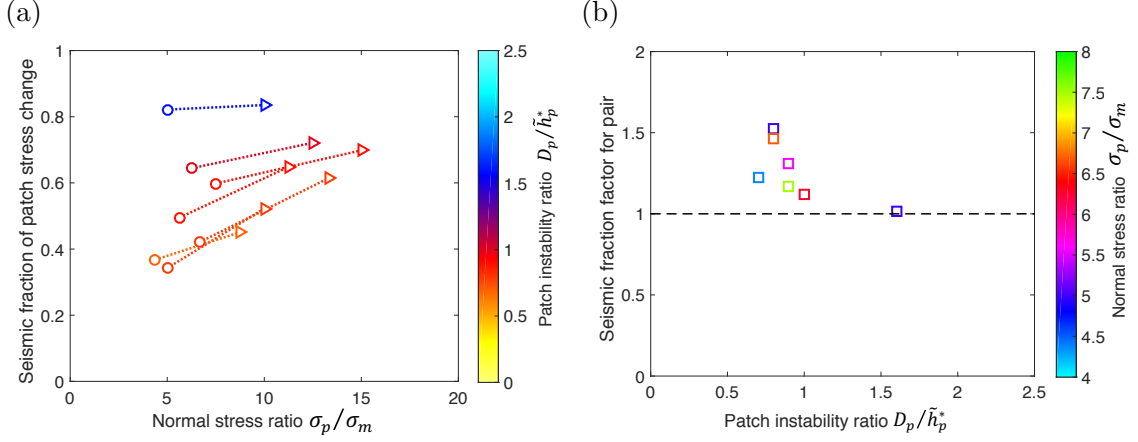


Figure 3.7.: Effect of simultaneously doubling σ_p and L_p on the seismic fraction of average shear stress change on the patch. **(a)** Median seismic average stress change fractions for pairs of simulations (connected by a dotted line) within the main set that have the same patch diameter D_p and patch instability ratio D_p/\tilde{h}_p^* , but for which the same patch nucleation size \tilde{h}_p^* (Equation 2.4) is achieved by a different combination of patch normal stress σ_p and patch characteristic slip distance L_p . Specifically, reviewing these pairs from left to right, the σ_p and L_p are simultaneously doubled to maintain the \tilde{h}_p^* . **(b)** Seismic fraction factor, i.e., the median seismic average stress change fraction of the paired simulation with the higher σ_p and L_p (triangles in (a)) over the median seismic average stress release fraction of the corresponding paired simulation (circles in (a)), versus patch instability ratio. The outline of these square markers is colored by the normal stress ratio of the paired simulation with the lower σ_p and L_p (circles in (a)). All values of the seismic fraction factor are greater than 1, which means that simultaneously doubling σ_p and L_p , for the same D_p and D_p/\tilde{h}_p^* , results in intershocks with consistently higher seismic fraction of the total average stress change.

the patch and the surrounding ruptured area, as discussed in Section 3.2.

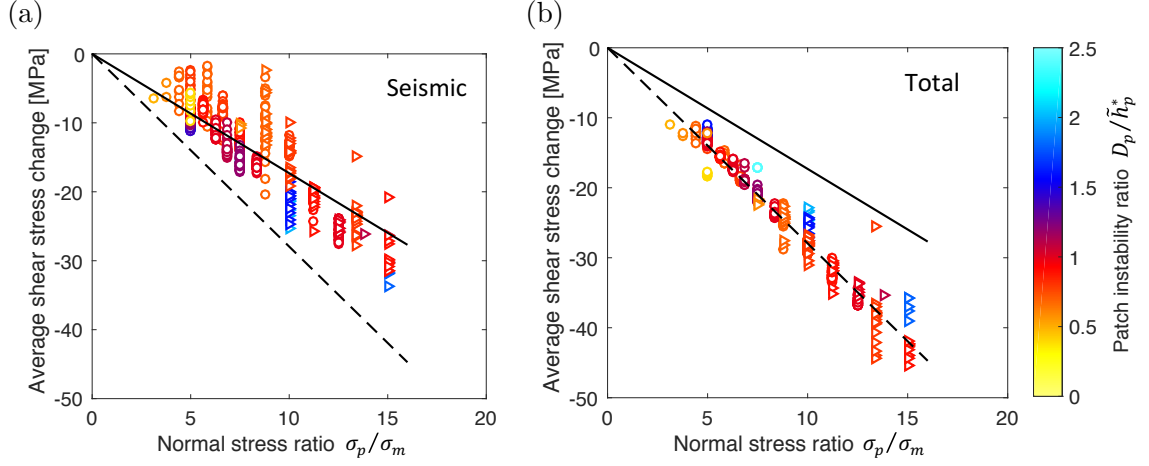


Figure 3.8.: Dependence of the seismic and total average shear stress change (on the patch) of the intershocks on the normal stress ratio for the main set of simulations. The simulation data and identifying marker features correspond to Figure 3.1. **(a)** Seismic average shear stress change plotted against the normal stress ratio σ_p/σ_m . The solid black line shows the best linear fit passing through the origin, $\overline{\Delta\tau_p} = -0.17\sigma_p$ (Equation 3.3). **(b)** Total average shear stress change versus normal stress ratio. The values for each intershock collapse along the black dashed trendline that passes through the origin, $\overline{\Delta\tau_{total}} = -0.28\sigma_p$.

Within the overall trend of the increasing magnitude of patch-averaged shear stress change with the increasing normal stress, there is a secondary dependence on patch instability ratio D_p/\tilde{h}_p^* . The patches with the highest instability ratios in our set (blue) tend to have more seismic and less total average stress change on the patch than the rest of the models (Figure 3.8), which would result in steeper and shallower slopes for the seismic and total stress change, respectively. This is because patches with higher instability ratios have their nucleation processes confined to a smaller fraction of the patch, and more of the patch experiences purely seismic stress change. Interestingly, despite resulting in more forceful ruptures on the patch, the total average stress change on the patch tends to be smaller for larger instability ratios, suggesting that the associated smaller nucleation sizes lead to less loaded patches before the rupture initiates (Figure 3.8b). The slope of the overall trend with respect to the normal stress σ_p is 0.17 and 0.28 for the seismic and total stress release, respec-

tively (Figure 3.8). Those values are quite similar to the expected slope of 0.20 for the stress drops $\overline{\Delta\tau}^{\text{SD}}$ based on the simulated mainshocks from a homogeneous model (Figure 3.1, black dotted line), and are related to the selection of the rate-and-state parameters a and b .

3.4. Simplified stress drop calculation

Profiles of the change in shear stress through the middle of the ruptured patch illustrate how the stress change varies spatially within the ruptured area (Figure 3.3a). While the profiles show that the stress change distribution is complicated, it is clear that the average change of stress on the patch $\overline{\Delta\tau}_p$ and off the patch $\overline{\Delta\tau}_m$ (Figure 3.3b) significantly differ, with the decrease in stress on the patch typically being much larger than the decrease outside. This heterogeneous distribution of the stress change results in the reported moderate stress drops $\overline{\Delta\tau}^{\text{SD}}$.

To gain further insight into the near-constant trend in stress drops $\overline{\Delta\tau}^{\text{SD}}$ with respect to the patch normal stress (Figure 3.1), we derive a simplified calculation for estimating the stress drop based on parameters from our simulation input and findings of Sections 3.2-3.3. Using a simple weighted average, we represent the area-based average stress drop $\overline{\Delta\tau}_a^{\text{SD}}$ by the combination of the shear stress changes on the patch and outside of the patch, within the ruptured area:

$$\overline{\Delta\tau}_a^{\text{SD}} = - \left(\overline{\Delta\tau}_p A_p + \overline{\Delta\tau}_m (A_r - A_p) \right) / A_r . \quad (3.2)$$

Assuming that both the patch and ruptured area are circular, one gets $A_p = \pi D_p^2/4$ and $A_r = \pi D_r^2/4$. Based on our simulation results, we assume the following approximate relationships:

$$\frac{D_r}{D_p} = \gamma \frac{\sigma_p}{\sigma_m}, \quad \overline{\Delta\tau}_p = -\eta_p \sigma_p, \quad \text{and} \quad \overline{\Delta\tau}_m = -\eta_m \sigma_m , \quad (3.3)$$

where γ , η_p , and η_m are taken as constants, but may depend on the model parameters. Inserting these relationships into Equation (3.2) results in

$$\overline{\Delta\tau}_a^{\text{SD}} = \left(\frac{\eta_p}{\gamma^2} \frac{\sigma_m}{\sigma_p} + \eta_m - \frac{\eta_m}{\gamma^2} \frac{\sigma_m^2}{\sigma_p^2} \right) \sigma_m, \quad (3.4)$$

revealing that the relation between the stress drops of intershocks and the normal stress ratio σ_p/σ_m in this approximation is dependent on the background normal stress σ_m and three constants that are likely dependent on the rate-and-state parameters, especially a and b . In the case of no patch of higher normal stress, one gets $\sigma_p = \sigma_m$, $A_p = A_r$, $\eta_p = \eta_m$, resulting in $\overline{\Delta\tau}_a^{\text{SD}} = \eta_m \sigma_m$ from Equation (3.4), which is expected.

For many intershocks in our models, the rupture dimension D_r is much larger than the patch diameter D_p , which leads us to another insightful simplification. In this case, $D_r \gg D_p$, so $A_r \gg A_p$, resulting in $A_r - A_p \approx A_r$. Applying this reduction to Equation (3.2) and inserting the relationships from Equation (3.3) gives

$$\overline{\Delta\tau}_a^{\text{SD}} = \left(\frac{\eta_p}{\gamma^2} \frac{\sigma_m}{\sigma_p} + \eta_m \right) \sigma_m. \quad (3.5)$$

For the main set of models in our study, the constants in Equation (3.5) can be calculated from linear fits for our simulation results: $\gamma \approx 0.41$ from Figure 3.4a, $\eta_p \approx 0.17$ from Figure 3.8a, and $\eta_m \approx 0.04$ from finding the average $\overline{\Delta\tau}_m$ (recalling that σ_m was held constant) (Figure 3.9). Using these constants results in $\overline{\Delta\tau}_a^{\text{SD}} = (\sigma_m/\sigma_p + 0.04) \sigma_m$, because $\eta_p/\gamma^2 \approx 1$ for this particular case. While the first term in this equation dominates for all of the models in this study, the second term would begin to dominate for $\sigma_p/\sigma_m > 25$.

The trend predicted by this equation (Figure 3.1, green dashed line) explains the main features of dependence on σ_p/σ_m , including the relatively low values of $\overline{\Delta\tau}^{\text{SD}}$ and the slight decrease of $\overline{\Delta\tau}^{\text{SD}}$ with σ_p/σ_m . It is important to note that the simplified stress drop calculation created here uses area-based averaging ($\overline{\Delta\tau}_a^{\text{SD}}$), whereas the

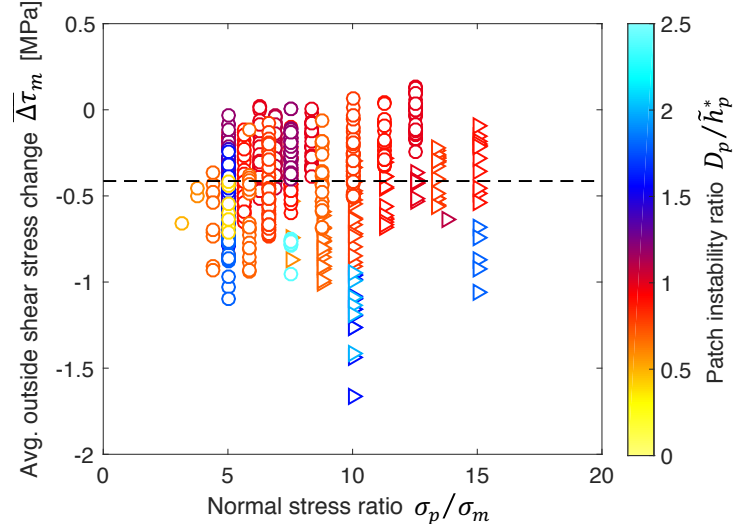


Figure 3.9.: Average shear stress change within the ruptured area outside of the patch $\overline{\Delta\tau_m}$ for intershocks in the main set. The black dashed line shows the mean value of approximately -0.4 MPa. Through dividing this value by the constant background normal stress σ_m of 10 MPa for this set, the coefficient η_m from Equation (3.3) is approximately 0.04.

stress drops computed in the simulations are moment-based ($\overline{\Delta\tau}^{\text{SD}}$, Equation 3.1), but the values of the two types of average stress drops are typically similar, with the area-based values usually smaller than the moment-based [Noda *et al.*, 2013].

Given that the background normal stress σ_m for models in the main set is held constant, we developed the Variable Background Normal Stress (VBNS) set (Section 2.3; Table 2.3) to test the dependence of stress drops on σ_m , illuminated by the simplified stress drop formulation $\overline{\Delta\tau}_a^{\text{SD}}$ (Equation 3.4). The stress drops $\overline{\Delta\tau}^{\text{SD}}$ for the VBNS set are well-approximated by the simplified estimate $\overline{\Delta\tau}_a^{\text{SD}}$ (Figure 3.10a) with the coefficients derived from the main set (Equation 3.5). Furthermore, we find that the relative rupture extents D_r/D_p for the intershocks from the VBNS set overlap well with the those from the main set (Figure 3.10c), although the coefficient γ derived for the VBNS set alone (Figure 3.10b) would be lower than that derived for the main set overall (which could simply be from the focus on a single patch instability ratio D_p/\tilde{h}_p^*).

The stress drops from the simplified estimate $\overline{\Delta\tau}_a^{\text{SD}}$ for both the main set and VBNS

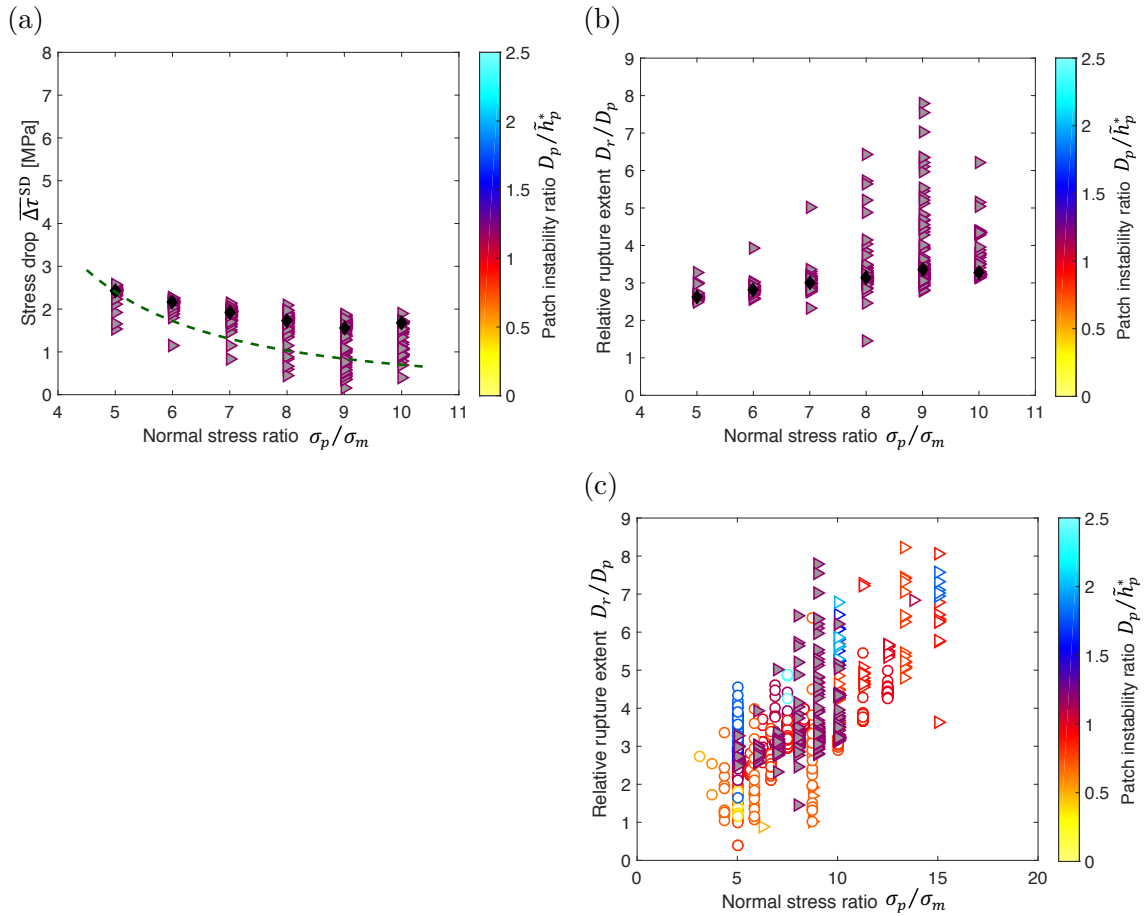


Figure 3.10.: Results for the Variable Background Normal Stress (VBNS) set of simulations. **(a)** Stress drops $\overline{\Delta\tau}^{\text{SD}}$ of the intershocks. The green dashed line shows the trend from the simplified stress drop calculation ($\overline{\Delta\tau}_a^{\text{SD}}$, Equation 3.5). Black diamonds indicate the median values for each simulation. **(b)** Effect of patch normal stress ratio σ_p/σ_m on relative rupture extent D_r/D_p for the VBNS set, with medians. **(c)** The relative rupture extents for the main set from Figure 3.4a with those from the VBNS set in (b) overlaid. For subplots (b) and (c), note that the two VBNS simulations with the highest normal stress ratio ($\sigma_p/\sigma_m = 9, 10$) each have one data point that is outside of the y-axis limits of these plots ($D_r/D_p = 12.8, 14.2$, respectively). The identity scheme for the data markers is the same as in Figure 2.3.

set fit well overall, but tend to decrease with the normal stress ratio σ_p/σ_m faster than the stress drops calculated for these events via the standard formulation $\overline{\Delta\tau}^{\text{SD}}$ (Figure 3.1, Figure 3.10a). The assumption, made for simplicity, that the coefficients γ , η_p , and η_m are constant contributes to this difference. As discussed in the previous sections, there is some evidence that these constants are additionally dependent on other parameters, for example, on the patch instability ratio D_p/\tilde{h}_p^* , with higher D_p/\tilde{h}_p^* , and hence, in general, higher σ_p/σ_m , corresponding to higher constants (e.g., blue symbols in Figure 3.4a, Figure 3.8a, and Figure 3.9). Still, our simplified stress drop calculation is successful in approximately matching the trend in stress drops $\overline{\Delta\tau}^{\text{SD}}$, especially given its simplicity.

4. Investigating seismological interpretations of asperity-type sources

This chapter begins with a description of the methods that we use to produce and analyze synthetic seismograms of the seismic events created in our 3D numerical simulations (Chapters 2 and 3), including how we derive estimates of the source properties (e.g., stress drop $\overline{\Delta\tau}^{\text{SD}}$ and moment M_0) from the spectra of the p- and s-waveforms using standard methods. Next, we discuss the theory behind classic idealized source models, in particular, the dynamic model of *Madariaga* [1976], and present additional idealized source models that we develop within our simulation framework. These sources are useful for comparison with the asperity-type sources that host intershocks in our main set of models (Section 2.3). We start by comparing parameters taken directly from the seismic spectra, specifically the normalized corner frequency k and fall-off rate n , and then proceed with a comparison of source properties, focusing on stress drops. In addition, we present explanations for any differences arising in the comparisons. The chapter concludes with a brief discussion of the seismological features of our asperity-type sources that may be characteristic.

The majority of this chapter is based on the manuscript in preparation by Na-

talie Schaal, Nadia Lapusta, and Yen-Yu Lin, entitled, “Seismological properties of asperity-type events in a rate-and-state fault model.” The production of the synthetic seismograms and the calculation of source parameters through spectral fitting is achieved using the software developed by Dr. Yen-Yu Lin, with some modifications by Natalie Schaal.

4.1. Producing synthetic seismograms

We produce far-field synthetic seismograms for the seismic sources in our simulated fault models at a variety of receiver locations, i.e., stations. The displacement \mathbf{u} in the far-field due to body waves radiated from a seismic point source i in a uniform linear elastic medium is given by [e.g., *Aki and Richards, 2002*]:

$$\mathbf{u}_i(\mathbf{x}, t) = \frac{1}{4\pi\rho c_p^3} \mathbf{A}^p \frac{1}{R_i} \dot{M}_0 \left(t - \frac{R_i}{c_p} \right) + \frac{1}{4\pi\rho c_s^3} \mathbf{A}^s \frac{1}{R_i} \dot{M}_0 \left(t - \frac{R_i}{c_s} \right), \quad (4.1)$$

where ρ is the material density, c_p and c_s are the speeds of the p- and s-waves, respectively, \dot{M}_0 is the moment rate, R_i is the distance between the source and receiver stations, and $\mathbf{A}^p = \sin 2\theta \cos \phi \hat{\mathbf{r}}$ and $\mathbf{A}^s = \cos 2\theta \cos \phi \hat{\boldsymbol{\theta}} - \cos \theta \sin \phi \hat{\boldsymbol{\phi}}$ are the radiation patterns for the far-field p- and s-waves, respectively. The coordinate system for Equation (4.1) is shown in Figure 4.1a. The seismic source is located in the x_1 - x_2 plane, centered at the origin, with the slip in x_1 -direction. The angles θ and ϕ (in combination with the distance in the radial direction) give the receiver location in spherical coordinates. With respect to the fault plane, θ gives the off-fault orientation (for example, $\theta = 0^\circ$ and $\theta = 90^\circ$ correspond to directions perpendicular to and in the plane of the fault, respectively), and ϕ gives the rotation about the source. As this coordinate system is defined relative to the plane of the fault, it is independent of the absolute fault orientation (i.e., independent of dip and rake angles), which is in contrast to observational coordinate systems typically used for describing the

moment tensor [e.g., Figure 4.20 in *Aki and Richards, 2002*], and sometimes creates confusion between source modelers and observational seismologists. The definition of θ and ϕ in the coordinate system that we use (Figure 4.1a) is the same as that of *Madariaga [1976]* (his Figure 1) and *Kaneko and Shearer [2014]* (their Figure 1a); however, *Madariaga [1976]* refers to θ as “azimuth” and *Kaneko and Shearer [2014]* refer to it as “take-off angle.” Thus, to avoid further confusion, we simply refer to the angles as θ and ϕ .

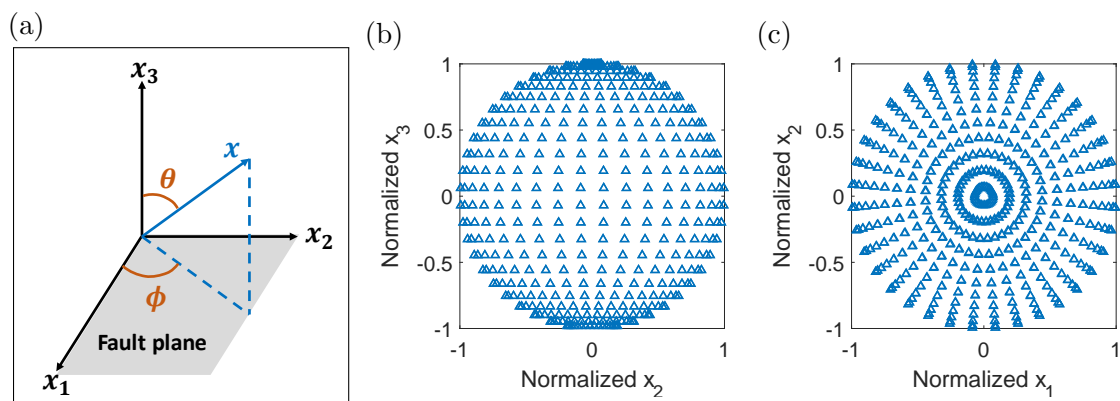


Figure 4.1.: The assumed coordinate system and focal sphere stations for the production of synthetic seismograms. **(a)** Coordinate system. For vertical strike-slip faults, as an example, the Earth’s surface would be parallel to the x_1 - x_3 plane. The earthquake source is in the x_1 - x_2 plane, with the strike slip in the x_1 -direction. **(b)**-**(c)** Distribution of the 864 unique receiver locations over the focal sphere, which are evenly spaced in θ and ϕ .

In constructing our synthetic seismograms, we calculate $\mathbf{u}(\mathbf{x}, t)$ at a given receiver location \mathbf{x} as a sum of $\mathbf{u}_i(\mathbf{x}, t)$ over all spatial cells i of our simulated earthquake source for the duration of the seismic event. Note that the calculation of the seismogram contribution from each individual cell $\mathbf{u}_i(\mathbf{x}, t)$ is carried out with respect to the local coordinate system of Figure 4.1a centered on the cell, as the slip at each cell is treated like a point source, according to Equation 4.1. Then, the coordinate system for the sum is fixed at the center of the source (for homogeneous models and asperity-type sources, this is taken to be the center of the seismogenic zone and center of the patch of higher normal stress, respectively), as we “stack” the time-shifted contributions of

the individual cells to account for the finite size of the source.

To calculate the moment rate \dot{M}_0 , we re-sample the slip rate data output from our 3D BIM simulations to have a constant time step and only keep values greater than or equal to our seismic velocity threshold of 0.1 m/s. This selection ensures that the source properties derived from the resulting seismograms can be consistently compared to those derived directly from the simulated fault motion, as they are both under the same definition of seismic slip. To analyze the p- and s-wave data separately, we take the p- and s-waveforms to be the first and second term of Equation (4.1), respectively – at the far field, the two waveforms are naturally separated by their arrival times. The spectrum of the waveforms is then computed by taking the Fourier transform of the magnitude of the respective far-field displacement terms.

We generate the synthetic seismograms over a focal sphere of receiver locations (Figure 4.1). To ensure that the station measurements are far-field as well as to provide consistency in the comparison between different sources, the radius of the focal sphere is chosen to be 50 times the average rupture dimension D_r of the source. However, we often plot the focal sphere over normalized distance, such that its radius is unity (Figure 4.1b-4.1c), in line with the standard. While restricting our analysis to a small set of neighboring stations on the sphere would provide partial azimuthal coverage for a given fault orientation and serve to represent the limitations of seismological observations on natural faults, in this work, we mainly consider the focal sphere as a whole. This allows us to compare the spherically-averaged seismologically derived quantities for our sources to those from classical works [e.g., *Madariaga, 1976; Sato and Hirasawa, 1973*] as well as more recent investigations [*Kaneko and Shearer, 2015*]. Note that the approach relies on a simplifying assumption that the bulk material through which the radiated waves from the source travel is homogeneous and linear elastic. This standard assumption allows us to avoid both scattering and attenuation, making our analyses more tractable. The assumption also makes our analyses the best-case

scenarios for identifying source properties and any characteristic features.

4.2. Deriving source properties from seismograms

4.2.1. Spectral fitting

To seismologically deduce the source properties of the simulated seismic events, we take the standard approach of spectral fitting [*Abercrombie, 1995; Ide and Beroza, 2001; Ide et al., 2003; Shearer et al., 2006; Allmann and Shearer, 2007; Hardebeck and Aron, 2009; Baltay et al., 2011; Kwiatek et al., 2011; Lin et al., 2012; Denolle and Shearer, 2016; Uchide and Imanishi, 2016*]. We fit a single corner frequency, Brune-type [*Brune, 1970*] function to the spectra of the p- and s-waveforms from our synthetic displacement seismograms, given as:

$$A(f) = \frac{\Omega_0}{1 + (f/f_c)^n}, \quad (4.2)$$

where Ω_0 is the spectral amplitude plateau for low frequencies, f_c is the corner frequency (in Hertz), which is inversely related to the duration of the seismic event, and n is the fall-off rate of the spectrum above the corner frequency, sometimes called the high-frequency fall-off rate. The standard approach is to assume $n = 2$, often referred to as the “omega squared model,” and simply fit for the corner frequency f_c and plateau Ω_0 . We fit the spectral function given in Equation (4.2) to our displacement spectra with fall-off rate fixed as $n = 2$, as well as with n allowed to vary as a fitting parameter. We call these two considerations the “constant $n = 2$ fit” and “variable n fit,” respectively.

In addition to the two single-corner-frequency spectral functions described above by Equation (4.2), other spectral functions have been proposed that have two corner

frequencies, f_{c1} and f_{c2} . One of these such spectral functions is given by

$$A(f) = \frac{\Omega_0}{\sqrt{1 + (f/f_{c1})^n} \sqrt{1 + (f/f_{c2})^n}}. \quad (4.3)$$

The case with $n = 2$ was originally proposed by *Haskell* [1964] and is used by *Denolle and Shearer* [2016]. Equation (4.3) could also be used with n allowed to vary. Another double-corner-frequency spectral function potentially relevant to our sources is one that we developed, and it is given as

$$A(f) = \frac{\Omega_{01}}{1 + (f/f_{c1})^2} + \frac{\Omega_{02}}{1 + (f/f_{c2})^2}. \quad (4.4)$$

This function is simply a superposition of two events of different sizes, each represented by a “constant $n = 2$ ” single-corner-frequency shape. The function given by Equation (4.4) was inspired by the shape of the p-wave spectra for some of our asperity-type sources, observed at certain receiver locations.

In the course of our investigation, we find that the three double-corner-frequency spectral functions (Equation 4.3 with $n = 2$ or variable n , and Equation 4.4) typically either converge to their single-corner-frequency counterparts or the value of the second corner frequency f_{c2} provides an unreliable fit. While we plan to explore this fit behavior more in future work, here, we focus the discussion on the fit results from the two single-corner-frequency spectral functions (Equation 4.2 with $n = 2$ or n varies), as in the example of event S1 (Table 4.1) shown in Figure 4.2. As a reference, the completed nucleation of this event is also shown in b.1 of Figure 2.7. For ease of discussion, the asperity-type seismic events highlighted in the seismological analysis presented in this chapter are given names in the form “event S#,” and their properties are listed in Table 4.1.

Before fitting with each of the five spectral functions, the displacement spectrum is first re-sampled at a rate of $\Delta \log(f) = 0.1$ to provide even weighting in the log

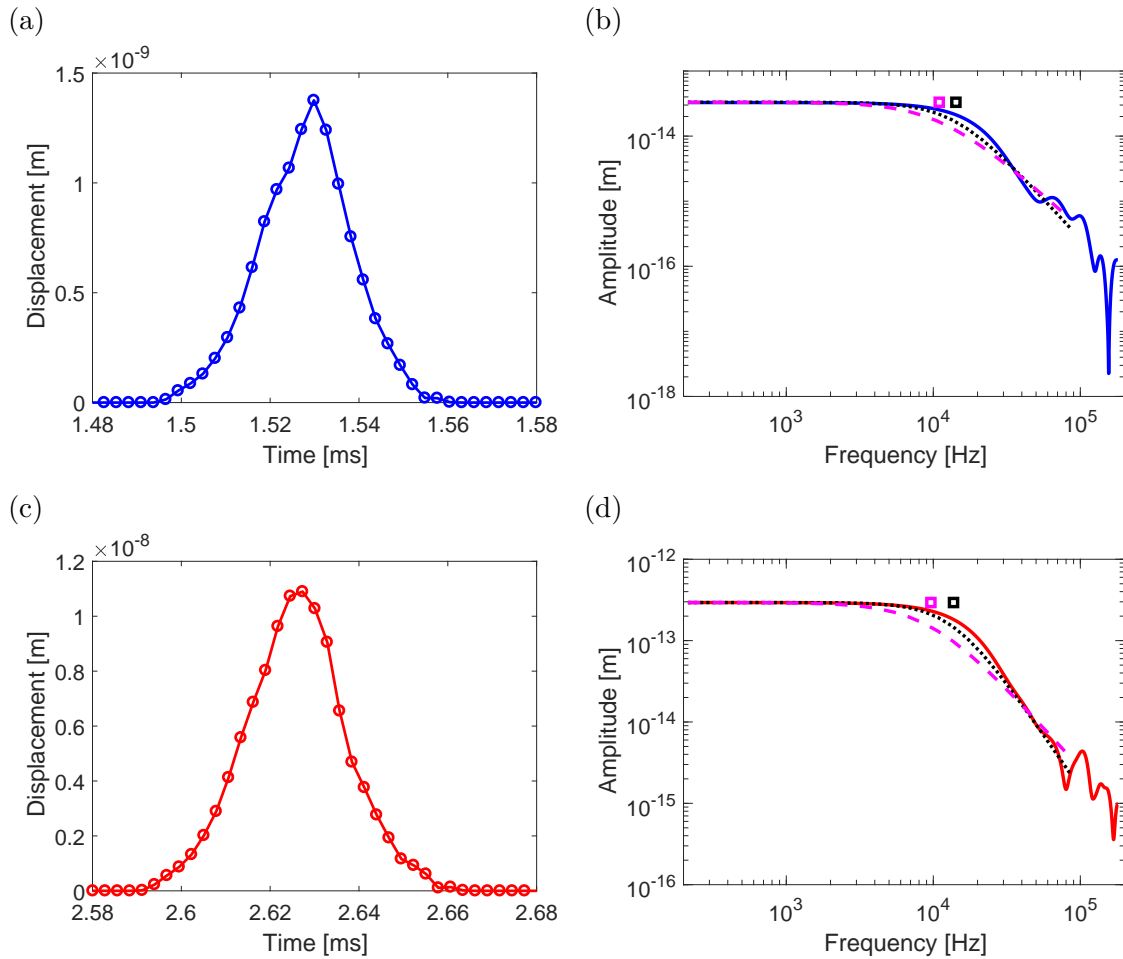


Figure 4.2.: Waveforms and spectral fits for event S1 calculated for station on the sphere located at $\theta = 26.5^\circ$ and $\phi = 55^\circ$. **(a)** P-waveform. **(b)** The spectrum of the p-waveform in (a) is shown as a solid blue line. The constant n (fit error $ER = 0.11$) and variable n ($ER = 0.05$, $n = 2.48$) fits are shown as a dashed magenta and dotted black line, respectively. The corresponding corner frequencies to the fits are shown by correspondingly colored squares. **(c)** S-waveform. **(d)** Spectrum of the s-waveform in (c), with the same color scheme for the fits as (b) (constant n fit error $ER = 0.13$, variable n fit error $ER = 0.04$ with $n = 2.64$).

Table 4.1.: Properties of the simulated asperity-type seismic events highlighted in Chapter 4. The non-dimensional fault model parameters listed in the second to fifth columns are as defined in Section 2.2–2.3. The moment magnitude M_w and stress drop $\overline{\Delta\tau}^{\text{SD}}$ are calculated directly from the 3D BIM simulation results using Equation (4.8) and Equation (3.1), respectively.

Event	D_p/\tilde{h}_p^*	σ_p/σ_m	L_p/L_m	D_r/D_p	M_w	$\overline{\Delta\tau}^{\text{SD}}$ [MPa]
S1	1.2	5.00	1/2	2.59	−3.78	2.46
S2	1.0	5.00	1/2	2.18	−4.06	2.74

scale and thereby avoid favoring the higher frequency side of the spectrum (due to the original higher density of data points in that region) in the fit. Then, parameters in each of the five spectral functions are determined from the p- and s-wave spectra, separately, by means of a nonlinear least-squares fitting method (“nlinfit” function in Matlab), using a Levenberg-Marquardt scheme [Marquardt, 1963]. For the single-corner-frequency spectral functions, we have also tested the nonlinear fit method against a grid search and found that the two methods result in very similar values for the fitted parameters while requiring significantly different computation times. Furthermore, the increased number of fitting parameters inherent in the more complex models can make the grid search method impractical. Thus, we proceed with the nonlinear fit method for its efficiency.

The nonlinear fitting method requires initial conditions and a spectral fitting range as inputs. Initial values for the fitting parameters are estimated from visual inspection of sample spectra for the given event, with 1 over the duration T of the seismic event taken from the 3D BIM simulations as an approximate reference estimate of the first corner frequency f_{c1} . The log-resampled spectra are fit up to the frequency f_{max} , which is taken to be $10/T$ (i.e., 10 times the predicted approximate corner frequency) or 50% of the Nyquist frequency associated with the constant-time-step re-sampled slip rate data used to calculate the displacement waveforms (Equation 4.1), whichever is lower. The inspiration for the multiplication factor of 10 comes from the situation

in observational seismology of the spectra of $M_w 2$ events with corner frequencies around 10 Hz being fit up to roughly 100 Hz [e.g., *Abercrombie, 1995; Ide et al., 2003*]. While seismologists are mainly limited by the sampling frequency of their seismometers, which is further reduced by considerations of the signal-to-noise ratio, here, we impose the 50% of the Nyquist frequency rule to ensure that we are avoiding any numerical noise at the highest frequencies. This ignored portion of the spectrum is relatively small on a log scale.

For almost all of the models of asperity-type sources that we seismologically analyze here, the value of n determined from fitting the spectra of the p- and s-waveforms is greater than 2. The trade-off between the corner frequency f_c and fall-off rate n in fitting any of the spectral functions presented thereby generally results in fits with variable n having higher f_c than their constant n counterparts (e.g., Figure 4.2b and 4.2d).

4.2.2. Calculating source properties from spectral parameters

For all of the spectral functions presented here, the seismologically derived moment M_0 and corner frequency \hat{f}_c (referencing f_{c1} for double-corner-frequency spectral functions) can be used to calculate the source radius according to

$$r = \frac{kc_s}{\hat{f}_c}, \quad (4.5)$$

and the stress drop from inserting Equation (4.5) into Equation (3.1), resulting in

$$\overline{\Delta\tau}^{\text{SD}} = \frac{7}{16} \left(\frac{\hat{f}_c}{kc_s} \right)^3 M_0. \quad (4.6)$$

The parameter k in both Equation (4.5) and (4.6), known as the normalized corner frequency, is a constant that relates the representative corner frequency \hat{f}_c to the

source dimension. The value of k is specific to the given theoretical model for how the source ruptures and the type of waveform being analyzed. For a single station, k depends on the direction between the source and the receiver (e.g., angles θ and ϕ). However, in practice, the angles are often not known. As such, usually a spherically averaged value of k is used together with any averaged corner frequency \hat{f}_c . On natural faults, since full spherical coverage of the source would not be available, typically the value of \hat{f}_c used is an average of f_c over the nearby surface stations. Table 4.2 summarizes the values of k_p and k_s derived from simple classical crack models, along with the updated model from *Kaneko and Shearer [2014]*, which feature a circular source expanding axi-symmetrically from its center with a constant rupture speed and constant stress drop. These reported values assume the full spherical average for \hat{f}_c , to be used in calculating the source radius or stress drops using Equation (4.5) and (4.6), respectively.

Table 4.2.: Theoretical values of average k for p- and s-wave spectra for classical idealized and updated source models. v_r is the assumed rupture velocity of the seismic source. k_p/k_s provides the expected p-to-s corner frequency ratios f_c^p/f_c^s for the given theoretical models.

k_p	k_s	k_p/k_s	Assumed v_r	Reference for theoretical model
N/A	0.37	N/A	∞	<i>Brune [1970]</i>
0.32	0.21	1.52	$0.9c_s$	<i>Madariaga [1976]</i>
0.42	0.29	1.45	$0.9c_s$	<i>Sato and Hirasawa [1973]</i>
0.38	0.26	1.46	$0.9c_s$	<i>Kaneko and Shearer [2014]</i>

The seismic moment M_0 can be calculated from the displacement spectrum of the p- or s-waveform as

$$M_0 = \frac{4\pi d \rho c_\alpha^3 \Omega_0^\alpha}{F^\alpha}, \quad (4.7)$$

where α corresponds to either “p” or “s”, Ω_0^α is the low-frequency spectral amplitude, F^α is the α -wave radiation pattern, d is the source-to-receiver distance, where the source location is at the origin of the coordinate system (Figure 4.1), ρ is the material

density, and c_α is the α -wave speed [Brune, 1970; Kaneko and Shearer, 2014].

There are two types of s-waves present: horizontal (sh) and vertical (sv). When we refer to the “s-wave,” we mean the sh-wave. While analysis of the sh- and sv-waveforms in our study generally produce similar results, we choose to focus on the sh-wave, in line with Lin *et al.* [2012], because the amplitude of its radiation pattern is larger than that of the sv-wave, and also because there are fewer nodal planes to avoid in the placement of our stations (radiation patterns for the p-, sh-, and sv-waves are shown in Figure 4.3; Figure 3 of De Martin *et al.* [2010], for example, provides another way to plot these patterns.)

If the source assumptions inherent in the chosen spectral analysis approach (e.g., choice of k) accurately describe the source, then the source parameters derived from the p- and s-wave spectra (i.e., r , M_0 , and $\overline{\Delta\tau}^{\text{SD}}$) would match. Often, the analysis of both spectra produces different values, which are then averaged or discussed separately.

To assess the accuracy of these seismological methods in determining the source properties of a seismic event, we compare the stress drop $\overline{\Delta\tau}^{\text{SD}}$ and moment estimated from the seismograms to the values derived directly from the fault behavior in our 3D BIM simulations (Section 4.5). Furthermore, we discuss potential explanations for the resulting differences in the seismologically and directly calculated source properties.

4.3. Scaling the simulated source to different moment magnitudes

We would like to utilize the simulated results from the laboratory-scale fault models described in Section 2.3 to investigate the seismological properties of our asperity-type sources for event sizes relevant to field observations on natural faults. Typical intershocks (i.e., microseismicity between mainshocks) in our meter-scale models have

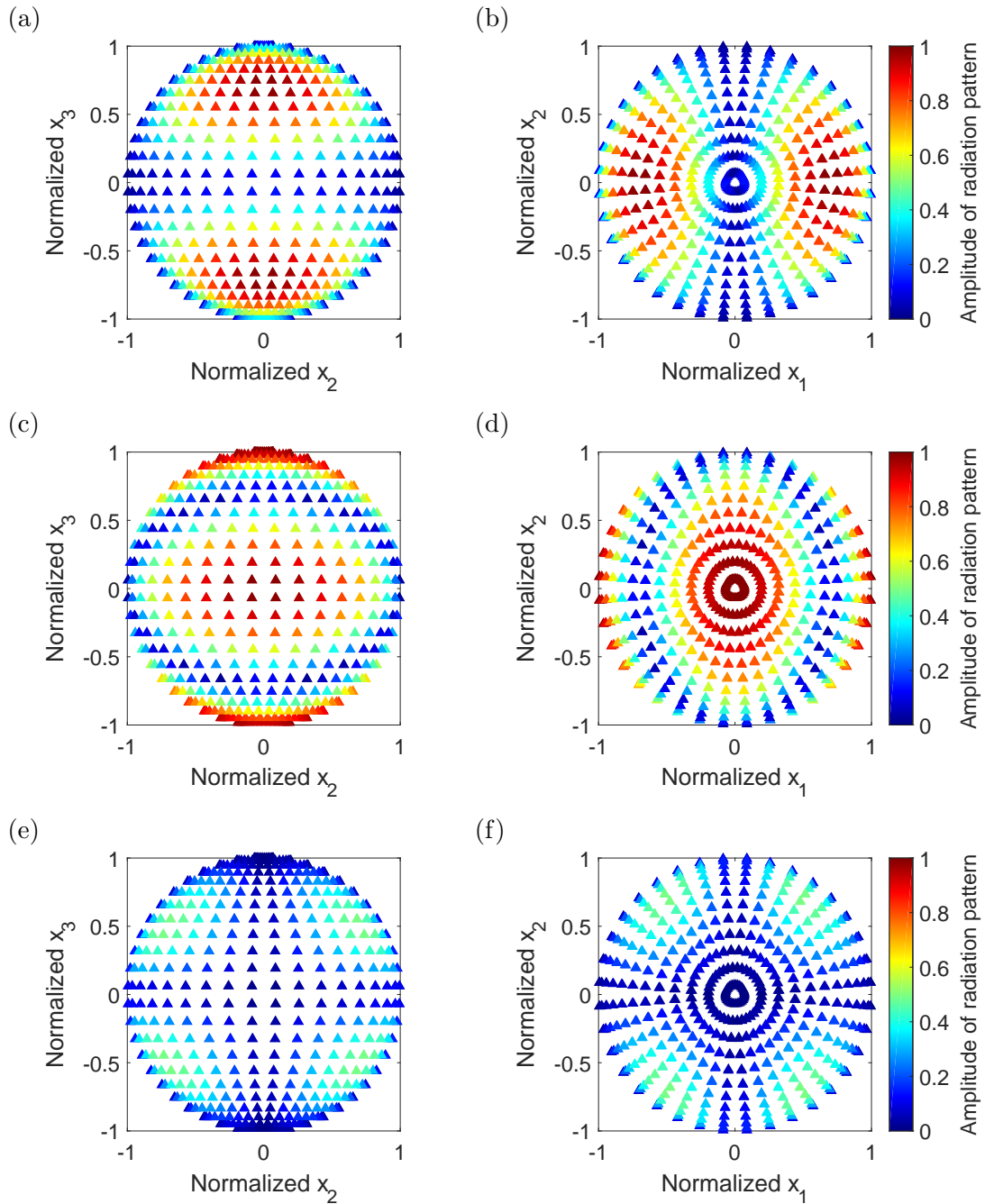


Figure 4.3.: Radiation patterns over the 864 focal sphere stations. (a)-(b), (c)-(d), and (e)-(f) show the radiation patterns of the p-wave, sh-wave, and sv-wave, respectively. The station (triangle) color indicates the absolute value of the radiation pattern amplitude at that station location. The two columns of subplots provide two views of the focal sphere, corresponding to Figure 4.1.

M_w around -4 , where the moment magnitude M_w is a translation of the seismic moment M_0 in units of Nm to a log scale, given by the following relation [*Kanamori, 1977*]:

$$M_w = (\log M_0 - 9.1) / 1.5 . \quad (4.8)$$

To bring these models up to the scale of the smallest events of about M_w 2 typically studied on natural faults, we multiply all length dimensions as well as the characteristic slip distance of the friction law by 10^3 . Assuming that the rupture velocity v_r of the seismic event is the same, then the duration is also increased by a factor of 10^3 . Seismic moment, defined as [*Aki, 1966*]:

$$M_0 = \mu A \bar{\delta} , \quad (4.9)$$

consequently scales up by a factor of 10^9 , as the shear modulus μ is scale-independent, the average slip scales with the source dimension for the same stress drop, and hence the product of the ruptured area A with the average slip $\bar{\delta}$ provides the factor of 10^3 cubed. The seismic moment increase by the factor of 10^9 translates into a moment magnitude increase of 6, resulting in scaled events with M_w 2 (Equation 4.8).

As such, the quantities associated with our fault models and seismic events should scale in a predictable way. Still, the mechanics problem that we solve numerically is nonlinear, and so simulations with scaled-up lengths and slip parameters may produce different results. To confirm our scaling assumptions, we conduct a simulation for the larger version of a lab-scale fault model with the spatial dimensions scaled by the factor of 10^3 and the characteristic slip distance L of rate-and-state friction scaled by 10^3 (the difference is consistent with the expected increase in L between the bare-rock experiments in the lab and ruptures on natural faults that occur in gouge layers), keeping all other parameters the same. The two models, the smaller-scale one and the larger-scale one, have the same non-dimensional properties, including normal stress

ratio σ_p/σ_m , characteristic slip distance ratio L_p/L_m , patch instability ratio D_p/\tilde{h}_p^* , nucleation size ratio $\tilde{h}_m^*/\tilde{h}_p^*$, relative rupture extent D_r/D_p , and isolation ratio \tilde{h}_m^*/D_r .

We indeed find that the resulting scaled-up source has nearly identical rupture speed and stress changes, resulting in quite similar dynamics and seismological properties (Figure 4.4). While the nonlinearity of the problem does result in slight differences between the dynamics (e.g., Figure 4.4a), as expected, they are too small to be relevant to our conclusions. In contrast, the outcome of the comparison could have been very different in models in which there is a feedback between the amount of slip and the constitutive response, as would be the case in models with additional dynamic weakening due to shear heating. In those models, higher shear heating for larger slips could significantly modify the evolution of shear stresses on the fault and hence cause significant quantitative and even qualitative differences, but this is not the scenario of our models. Overall, this shows that the analysis of our lab-scale events has direct implications for small events on nature faults. Note that the main seismologically-derived quantities that we analyze in the following are non-dimensional, including the normalized corner frequency k , p-to-s corner frequency ratio f_c^p/f_c^s , and fall-off rate n .

4.4. Comparison of seismologically-derived spectral parameters from the asperity-type sources to idealized models

4.4.1. Idealized Source Models (ISMs)

As we explore the seismological features of our asperity-type earthquake sources, we start by making a comparison with the standard sources assumed in seismological analyses. These standard sources attempt to mimic a conceptual case of an axi-

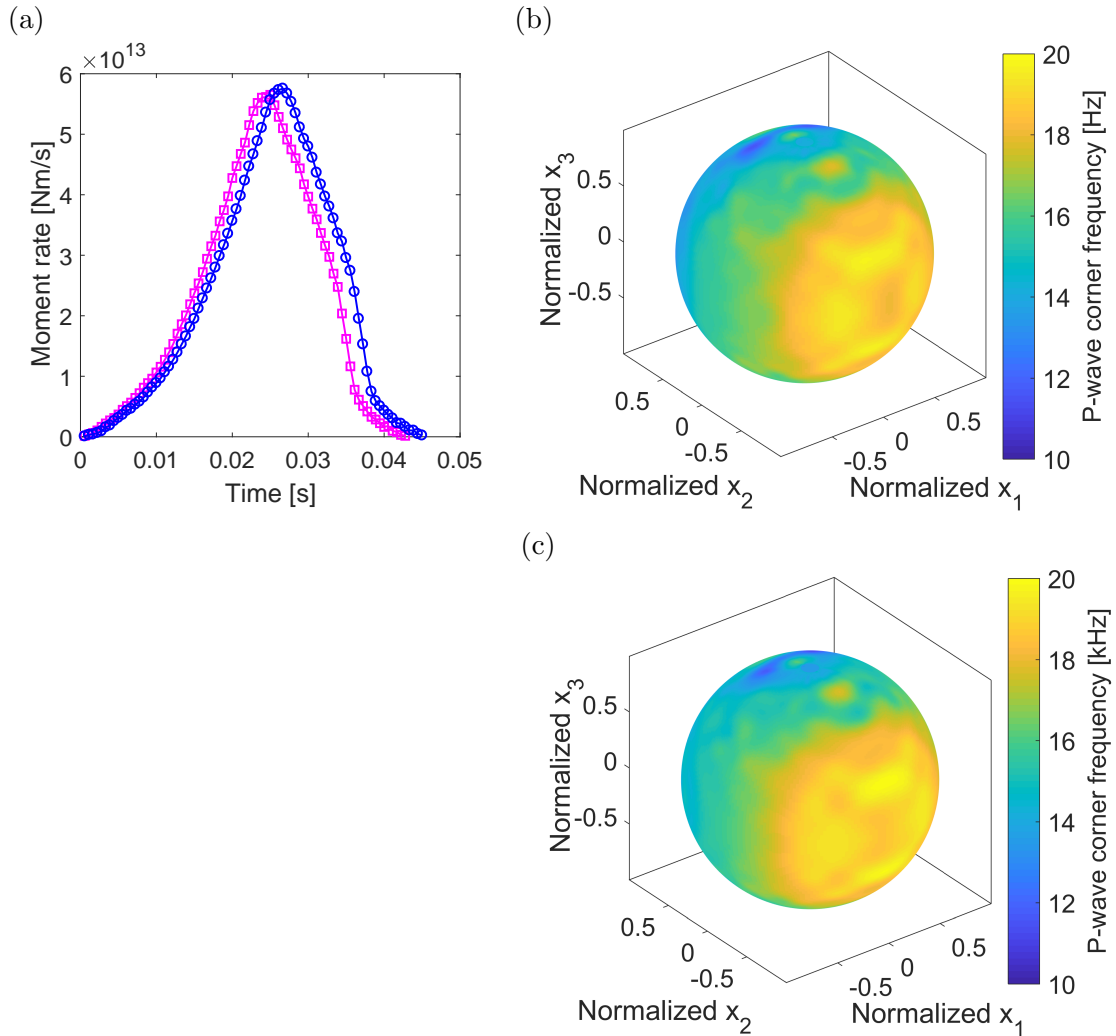


Figure 4.4.: Comparison between dynamic events in models with spatial and slip-related scales different by a factor of 10^3 . **(a)** Moment rate for an intershock. Magenta squares and blue circles indicate the data from an asperity-type event with M_w 1.92 and M_w -4.06 (event S2) in the km-scale and lab-scale fault model, respectively. For comparison on the same scale, the data from the lab-scale event is scaled by 10^3 in time and 10^6 in moment rate. **(b)** and **(c)** show the interpolated focal sphere for the p-wave corner frequency f_c^p calculated from the constant $n = 2$ fit for the km-scale and lab-scale event, respectively. The distribution is very similar, with the corner frequencies for the lab-scale event 10^3 times higher than those for the km-scale event, as expected (note that Hz vs. kHz are shown in the two panels).

symmetric shear rupture starting at a point and spreading on a planar surface in an elastodynamic space with a constant rupture speed v_r and constant shear stress drop until a final size is reached, resulting in a circular source, as envisioned by *Kostrov* [1964], who developed a semi-kinematic mathematical solution to this idealized crack problem. Unfortunately, his scenario is not completely physical for a number of reasons. First, it envisions an abrupt slip arrest once the rupture reaches the desired perimeter. In any physical model, the rupture arrest at the perimeter would send healing phases that would eventually arrest the rupture in the middle of the slipping region, but not before causing additional slip and a redistribution of shear stress, with more slip in the center of the source and systematic variations in stress drop which would no longer be strictly constant. Second, it is difficult to keep the rupture speed constant, since, for the simplest case of a constant fracture energy, the rupture would accelerate to the limiting speeds as it propagates, which would be different in the Mode III and Mode II directions, being c_R and c_s , respectively [e.g., *Freund*, 1990]. If one desires to produce a physical model with a completely uniform rupture speed, one would need to come up with fault resistance laws that result in just the right changes in the fracture energy as the rupture grows, which would need to vary along the rupture circumference, negating the apparent “simplicity” of the underlying source. Third, the model as is would result in an infinite shear stress outside of the ruptured perimeter, which is non-physical. Any regularization of the problem (e.g., through a cohesive zone model) would result in a region of varying stress change at the perimeter of the crack, the extent of which would depend on the regularization (e.g., the cohesive zone assumptions).

Nonetheless, given the philosophical appeal of this “simple” model in seismology, several works attempted to produce a numerical kinematic or dynamic version of it, with the goal of obtaining the resulting synthetic seismograms and establishing the link between the source properties and seismogram properties. This resulted

in several Kostrov-like models, which we refer to as Idealized Source Models (ISMs), including the widely used kinematic solution of *Sato and Hirasawa* [1973] and dynamic solution of *Madariaga* [1976], as well as a more recent model by *Kaneko and Shearer* [2014]. Since all of these models address the non-physical features of the underlying conceptual model in a different way, they all differ slightly in terms of their rupture dynamics – including slip, rupture speed, and stress drop distribution over the circular earthquake source – and hence differ in terms of their synthetic seismograms and relation to the source properties, as documented in Table 4.2.

Here, we develop our own ISMs to facilitate the comparison between the various features of these standard earthquake sources that currently guide seismological analyses and our more complex intershock sources. The creation of our own ISMs allows us to make a more consistent comparison with our more complex sources, as all models would use similar assumptions about the rupture arrest, crack-tip behavior etc., which differ in the currently available ISMs.

In comparing to classical ISMs, we mainly reference the source of *Madariaga* [1976] (with $v_r = 0.9c_s$) because he was the first one to produce a dynamic Kostrov-like source and his version is commonly used [e.g., *Abercrombie*, 1995; *Shearer et al.*, 2006; *Allmann and Shearer*, 2007; *Hardebeck and Aron*, 2009; *Kwiatek et al.*, 2011]. The first ISM that we develop aims to represent the Madariaga-like ISM as closely as possible. Due to numerical limitations, we cannot make the event initiate at a point as the ideal source would, and so we force it to start over an area equal to one nucleation size \tilde{h}^* (by prescribing increased shear stress) in the middle of a circular velocity-weakening region that is approximately 13 times larger in diameter than \tilde{h}^* . The rupture proceeds with an average local rupture speed \bar{v}_r^{loc} of $0.9c_s$ (Figure 4.5d). The instability ratio of $D_{\text{VW}}/\tilde{h}^* = 13$ is chosen to balance the goal of making the event initiation as point-like as possible with the necessity of resolving the crack tip well. The stress change over our ISM has an approximately constant value of

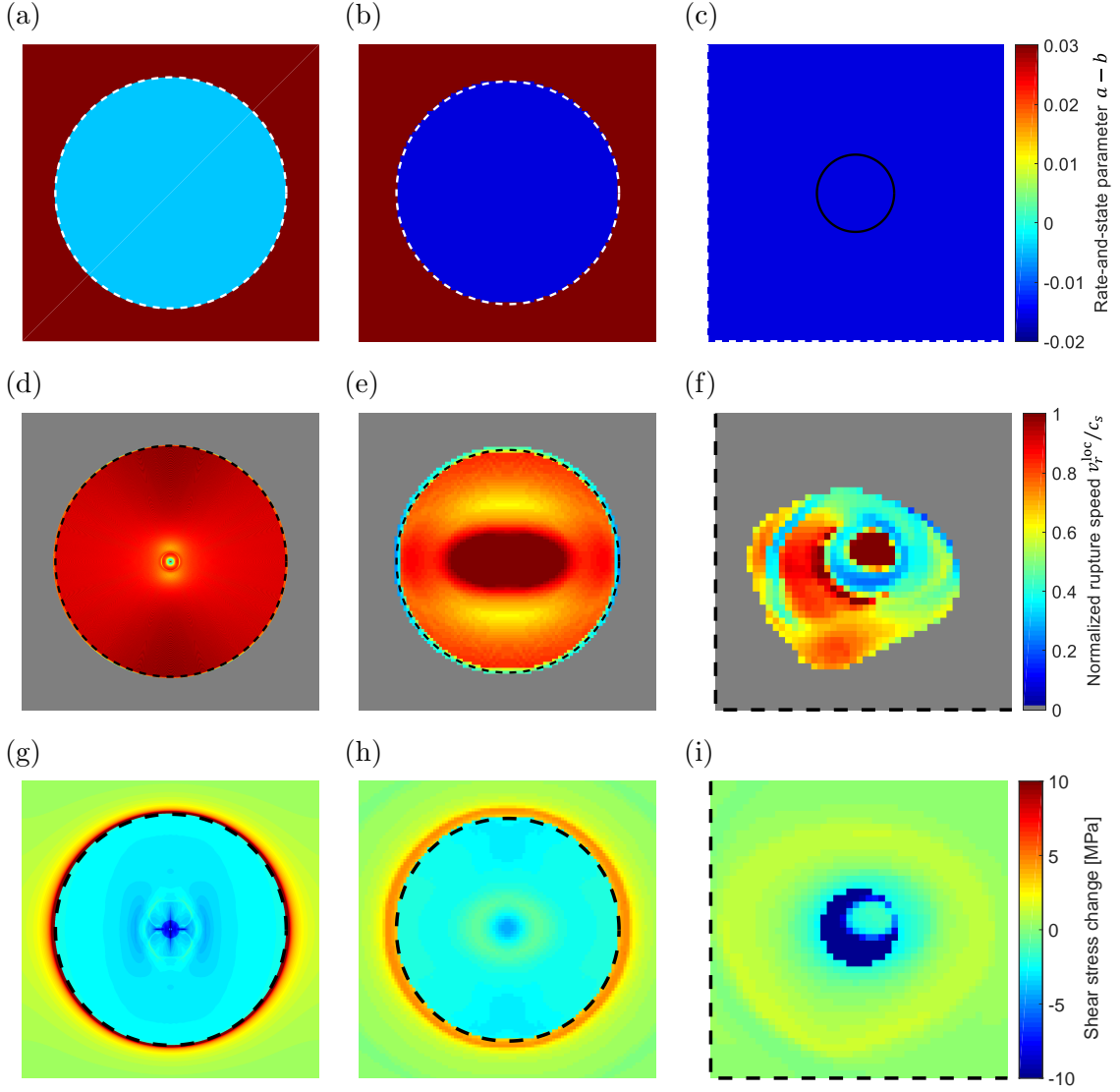


Figure 4.5.: Source models for our Madariaga-like ISM (column 1), RES-like ISM (column 2), and asperity-type event S1 (column 3). **(a)-(c)** The distribution of the rate-and-state parameter $a - b$ over each fault model, zoomed in to focus on the source area. The velocity-weakening zone is outlined with a white dashed line, and the velocity-strengthening region ($a - b > 0$) is maroon on the color scale. In (c), the asperity is outlined in black (see Table 4.1 for properties). **(d)-(f)** The local rupture velocity v_r^{loc} , calculated as the inverse gradient of the rupture times for each fault cell within the ruptured area, normalized by the shear wave speed c_s . The gray color indicates cells outside of the ruptured area. The velocity-weakening zone is now outlined with a black dashed line. **(g)-(i)** The shear stress change for the seismic event.

approximately -3 MPa over most of the ruptured area, corresponding to a stress drop of about 3 MPa, but differs from the ideal Kostrov solution, as expected. It differs at the nucleation location due to higher shear stress there and at the edges due to our friction law resulting in an equivalent of a non-zero cohesive zone size (Figure 4.5g).

We also develop another ISM. Inspired by the occurrence of Repeating Earthquake Sequences (RESs) on natural faults and the related fault models of *Chen and Lapusta* [2009] and *Lui and Lapusta* [2016], we create a RES-like ISM. The instability ratio of the circular velocity-weakening region in this model $D_{\text{VW}}/\tilde{h}^*$ is 3, which allows the seismic event to initiate in a more natural way, as the radial creeping front from the velocity-strengthening region moves inward on the seismogenic zone and collapses in the center (recall that instability ratios in this work are reported in reference to the mode III nucleation size, and so the ratio for mode II would be smaller – see Equation 2.4). In developing this RES-like ISM, instability ratios $D_{\text{VW}}/\tilde{h}^*$ less than 3 were also explored, but those models had a ring-like initiation as the seismic slip initiated at the edges of the nucleated area and/or had an average local rupture speed \bar{v}_r^{loc} that was slower than $0.9c_s$.

Similarly to our Madariaga-like ISM, the RES-like ISM has a stress change that is approximately constant over most of the ruptured area (Figure 4.5h). However, its rupture speed is more inhomogeneous (Figure 4.5e), although the average local rupture speed \bar{v}_r^{loc} is still $0.9c_s$, which is in part due to the high values in the middle from the almost in-place acceleration of slip at the start of the seismic event. An asperity-type source (event S1) from our simulations discussed in Chapter 2 and 3 has a more asymmetrical rupture area, heterogeneous rupture speed with a lower average value ($\bar{v}_r^{\text{loc}} = 0.74c_s$), strong heterogeneity in the stress change, and a more gradual arrest (Figure 4.5).

Let us consider the slip behavior of these sources. Following *Madariaga* [1976], we

compare the normalized slip over time at six output points along a horizontal line (mode II direction) from the center to the edge of the seismogenic zone (velocity-weakening region) to the digitized data from Figure 4 in *Madariaga* [1976], as shown in Figure 4.6. For our Madariaga-like ISM, the comparison (Figure 4.6a) reveals that

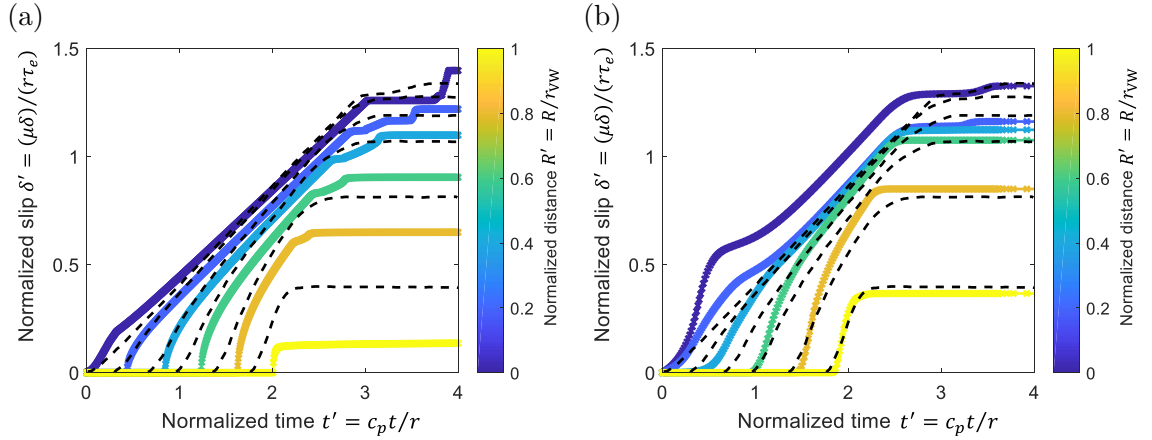


Figure 4.6.: Comparison of the normalized horizontal source slip profiles of our ISMs to the model from *Madariaga* [1976] for (a) the Madariaga-like ISM and (b) the RES-like ISM (the same events featured in the first two columns of Figure 4.5). Black dashed lines indicate the digitized source data presented in Figure 4 of *Madariaga* [1976] for normalized radial distances $R' = R/r = 0$ (dark blue), 0.2, 0.4, 0.6, 0.8, and 1.0 (yellow). In our ISMs, the events rupture slightly into the surrounding velocity-strengthening region, and so the ruptured radius r is slightly larger than that of the velocity-weakening region r_{VW} . For comparison with our ISMs, the slip data is plotted for the same values of R' as in *Madariaga* [1976], but with respect to r_{VW} , indicated by the plotting color. The slip and time information is also normalized following *Madariaga* [1976]. For effective stress τ_e , the moment-based stress drop from Equation (3.1) is used.

slip profiles near the center of the source (blues) match Madariaga’s results the best, while the profiles near the edge of the source (yellows) have lower values. However, the shape and height of the profiles for our Madariaga-like ISM are reminiscent of those from the source model described by Figure 7 in *Kaneko and Shearer* [2014]. The slip profiles for our RES-like ISM (Figure 4.6b), on the other hand, match well the profiles near the edge of the source, but the profiles near the center of the source are matched less well. We suspect that these differences in the slip profiles near the edge of the seismogenic zone reflect differences in how the events arrest, which is, in turn, affected

by the conditions of slip when the event initiates – for example, the Madariaga-like ISM starts at the center of the velocity-weakening region while the majority of the patch is locked, creating a sharper transition in slip behavior where the event arrests (Figure 4.5d); whereas all of the fault is creeping when the event initiates in the RES-like ISM, allowing for a smoother arrest near the edges of the seismogenic zone as those areas were already matching the slip in the velocity-strengthening region, making it easier to slip further (Figure 4.5e).

Now that we have compared the dynamics of our ISMs in Figure 4.5 and Figure 4.6, we can explore how these differences in source behavior translate into trends in seismological properties, such as normalized corner frequency k and high-frequency fall-off rate n . The original Madariaga source is associated with a specific trend in normalized corner frequency $k = rf_c/c_s$ with θ (a rearrangement of Equation 4.5, with corner frequency f_c taken at a given receiver location) and it is independent of ϕ due to its axi-symmetry (Figure 4.7a, solid blue line for p waves, red dashed line for s waves). The original Madariaga source is commonly linked to a single-corner-frequency spectral model with $n = 2$, despite the fact that the values of k determined by *Madariaga* [1976] are for the fit in which n was adjusted and varied with θ . That is why we compare our ISM models to that of *Madariaga* [1976] for both the case where $n = 2$ is imposed and the case in which n is adjusted to provide a better fit. For $n = 2$, we find that both the k_p and k_s for our Madariaga-like ISM deviate significantly from Magariaga’s original values (Figure 4.7a). When we instead calculate k_p and k_s using a variable n fit, the similarity is much higher (Figure 4.7b). Our k results from the variable n fit are also quite similar to those from the source model of *Kaneko and Shearer* [2014] (Figure 4.7c), who used the variable n fit as well.

Like for the Madariaga-like ISM, the k versus θ trends for the RES-like ISM deviate significantly from the digitized data of *Madariaga* [1976] for the constant n fit (Figure 4.8a), and follow the digitized trend more closely for the variable n fit (Fig-

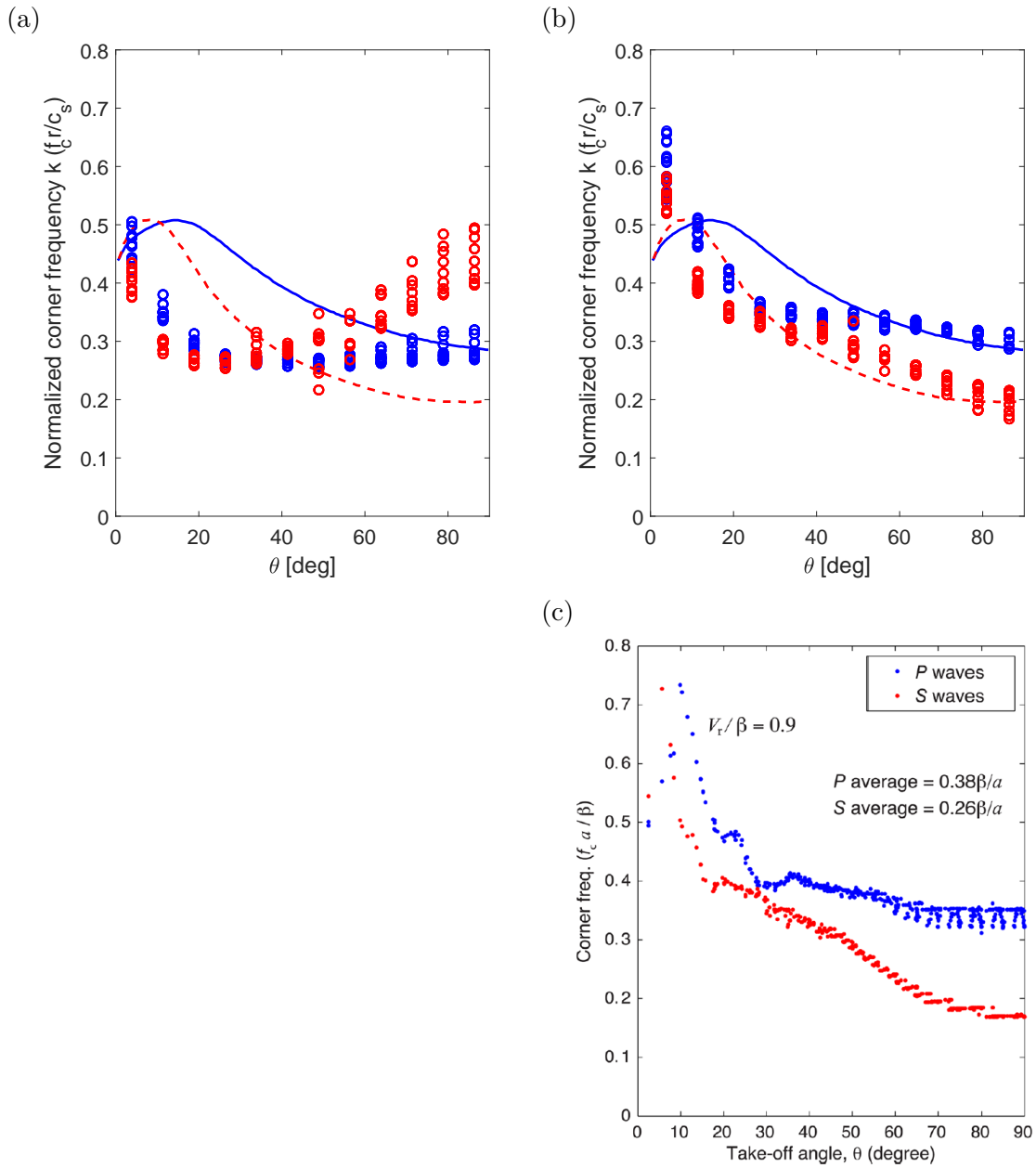


Figure 4.7.: Comparison of trends in k vs. θ for our Madariaga-like ISM. The solid blue line and dashed red line represent normalized corner frequencies k_p and k_s over θ from the digitized data of Figure 11 in *Madariaga* [1976]. The blue and red circles indicate the values of k_p and k_s for our Madariaga-like ISM over the section of the focal sphere with θ between 0° and 90° for (a) the constant $n = 2$ fit and (b) the variable n fit. (c) The same values for the model from *Kaneko and Shearer* [2014] (their Figure 4a, reproduced with permission from Oxford University Press). Note that any spread in the data points for a given θ indicates dependence of k on ϕ .

ure 4.8b). In comparison, we find that k trends from both the constant and variable n fits for the RES-like ISM match Madariaga’s data even better than our Madariaga-like ISM does. However, the RES-like ISM has more ϕ -dependence, indicated by the somewhat wider spread in the data points for a given θ . This is not surprising, given that our RES-like ISM is not as axi-symmetric (Figure 4.5e).

The comparison shows that our Madariaga-like ISM and RES-like ISM are indeed similar to both the model in *Madariaga* [1976] and the model in *Kaneko and Shearer* [2014]. At the same time, it highlights the difficulty in reproducing the idealized model of *Kostrov* [1964], as the results are similar but not identical even when significant care is taken to adhere to its properties as much as possible.

Furthermore, these results suggest that the current seismological practices are inconsistent, in that they use the spectral fit with $n = 2$ to analyze the natural data but then adopt the values for k from an adjustable n method from *Madariaga* [1976]. Using the wrong values of k should already result in mis-estimation of the stress drop, even if the natural events were exactly like Madariaga’s source.

Let us now consider an asperity-type source, event S1. The trends in k values vs. θ are now clearly different from the standard Madariaga model for both the constant and variable n fits (Figure 4.9). Furthermore, there is a wide variation with ϕ for both k_p and k_s . Such differences indicate that the events would not be properly characterized with the standard analysis. We analyze these difference further in Section 4.4.2, by exploring simplified models that still have heterogeneous shear stress change, and in Section 4.5, by comparing seismologically-derived stress drops for asperity-type events to their counterparts computed directly from the on-fault behavior in our 3D BIM simulations.

In addition to comparing trends in the normalized corner frequency k with angle θ , we also study the trends in fall-off rate n_p and n_s for the spectra of the p- and s-waves, respectively. For our Madariaga-like ISM, the fall-off rates vary over θ , but for a small

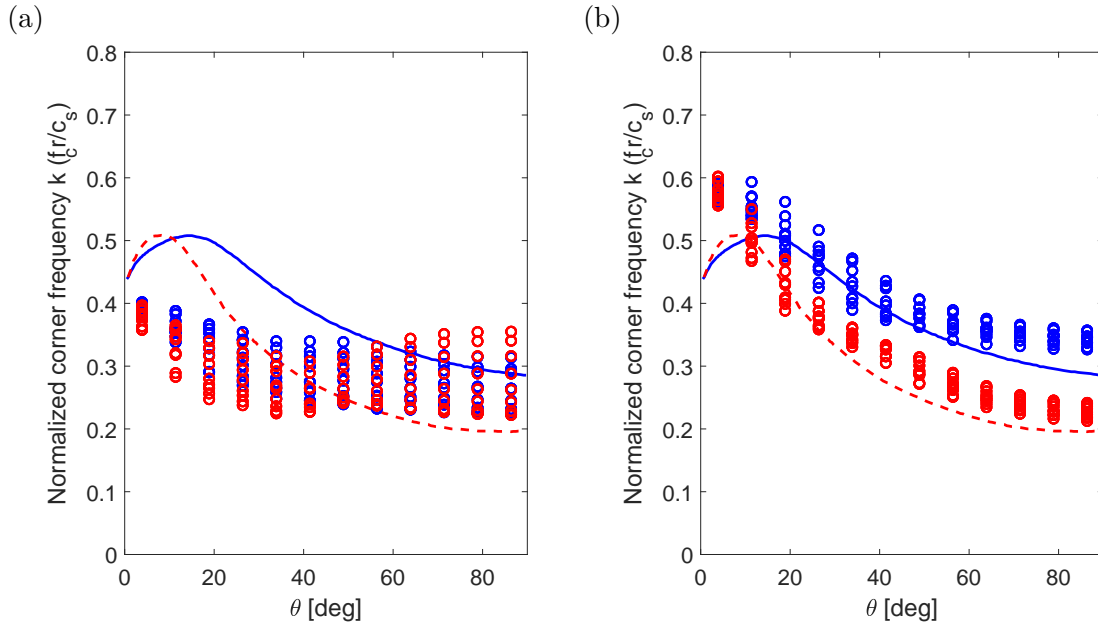


Figure 4.8.: Comparison of trends in k vs. θ for our RES-like ISM. Identity scheme and digitized data from *Madariaga* [1976] is the same as in Figure 4.7. (a) Constant $n = 2$ fit. (b) Variable n fit.

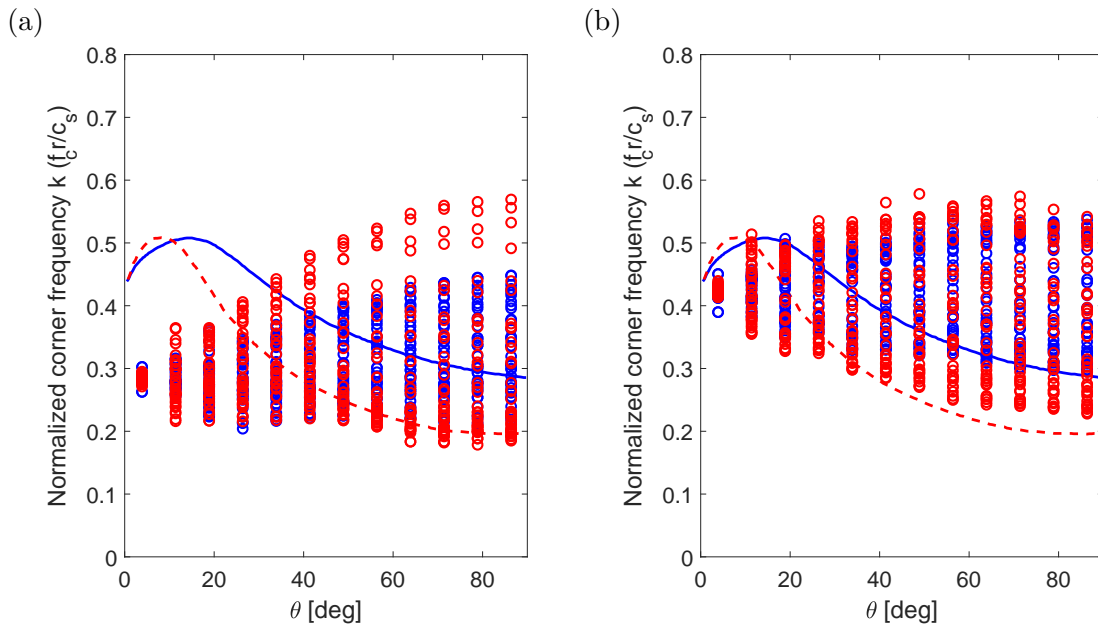


Figure 4.9.: Comparison of trends in k vs. θ for an asperity-type source (event S1), analogous to Figure 4.8. (a) Constant $n = 2$ fit. (b) Variable n fit.

range near the commonly assumed value of $n = 2$ and show slight dependence on ϕ (Figure 4.10a). This is consistent with the discussion in *Madariaga* [1976], which used variable n fit, but direct comparison is not possible as no plot of n was provided. The fall-off rates n for our RES-like ISM exhibit a similar but amplified trend, with a larger variation in n with θ that is quite similar to that from the source model of *Kaneko and Shearer* [2014] (Figure 4.10b). For example, small values of θ have values of n reaching above $n = 3$ in both. However, our RES-like ISM produces a somewhat wider spread with respect to ϕ (Figure 4.10c). Finally, the results for the asperity-type event S1 show: (1) a different trend of higher values of n for all values of θ , with most values above 2 and a spherically-averaged values $n_p = 2.58$ and $n_s = 2.53$ (Table 4.4), and (2) an even wider spread with respect to ϕ (Figure 4.10d).

4.4.2. Centered Asperity-Type Source Models (CATSMs)

Since the distribution of the five circular patches of higher normal stress within the seismogenic region in the models described in Chapter 2 creates additional complexity in the nucleation and subsequent rupture of these patches as intershocks (including the asymmetric proximity of the velocity-strengthening region around a given patch), here, we develop four additional asperity-type source models under simplified conditions. These new models involve a hybrid of the RES-like and asperity-type environments, and we call them Centered Asperity-Type Source Models (CATSMs) (Table 4.3). If the trends in the seismologically-derived properties of our usual asperity-type sources, in contrast to the Idealized Source Models (ISMs), also appear for the CATS Models, then this correlation would suggest that the trends are due to the shared nature of the heterogeneous normal stress, and hence heterogeneous stress change, instead of other factors produced by the additional complexity of our usual sources.

The Centered Asperity-Type Source Models are created by placing a circular patch

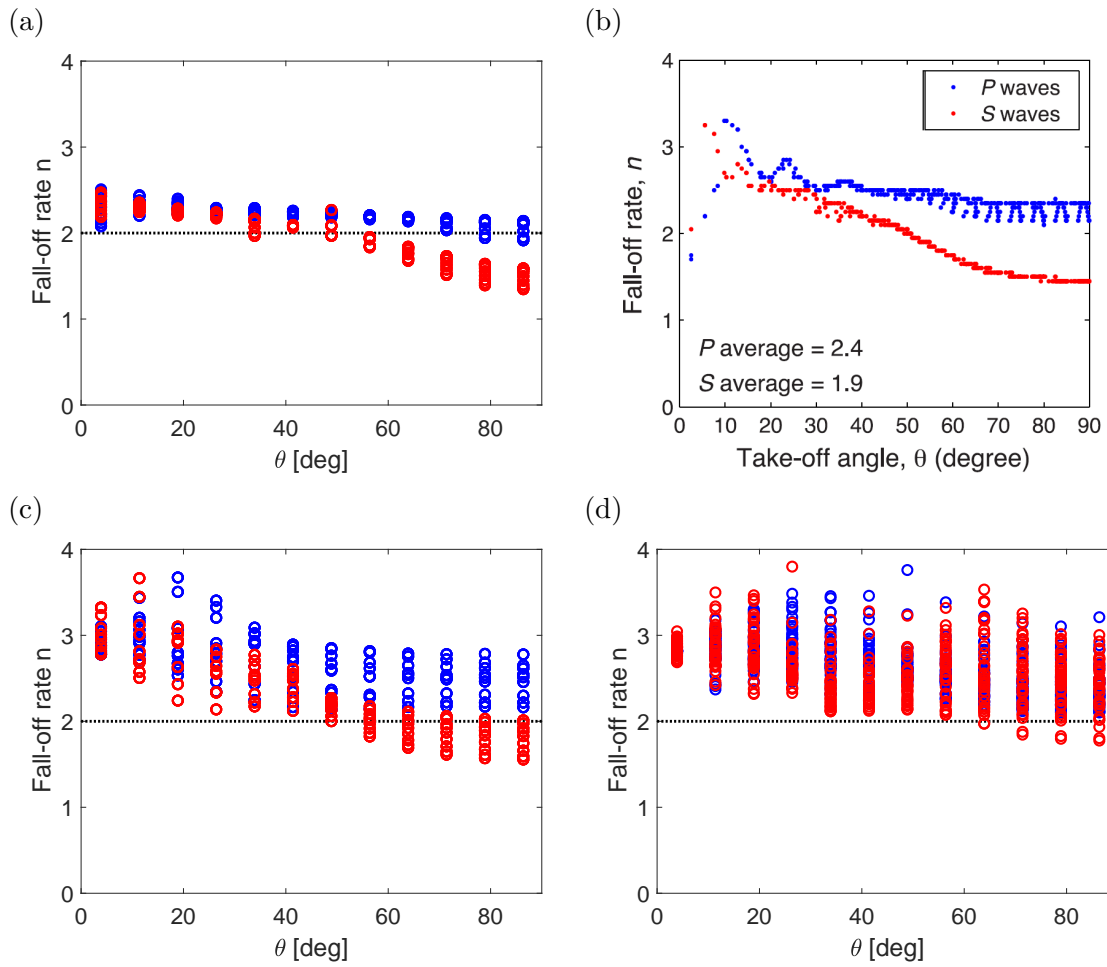


Figure 4.10.: Comparison of trends in the fall-off rate n vs. θ for a variable n spectral fit for different source models. **(a)** Our Madariaga-like ISM. **(b)** Model from *Kaneko and Shearer [2014]* (their Figure 5a, reproduced with permission from Oxford University Press). **(c)** Our RES-like ISM. **(d)** Asperity-type event S1. Blue and red markers indicate the results from the p- and s-wave spectra, respectively, and the black dotted line highlights the common assumption of $n = 2$.

Table 4.3.: Properties of the Centered Asperity-Type Source Models (CATSMs). The stress drops $\overline{\Delta\tau}^{\text{SD}}$ are calculated directly from the 3D BIM simulation results. All of the CATSMs have a patch instability ratio D_p/\tilde{h}_p^* of 1.0, and a background instability ratio $D_{\text{VW}}/\tilde{h}_m^*$ of 0.75.

Model name	σ_p/σ_m	L_p/L_m	D_r/D_p	$\overline{\Delta\tau}^{\text{SD}}$ [MPa]
CATSM 1A	5.0	1	3.26	2.43
CATSM 1B	5.0	1/2	2.26	2.37
CATSM 2A	10.0	1	4.29	2.31
CATSM 3A	15.0	1	5.27	2.13

of higher normal stress in the center of a circular velocity-weakening zone, surrounded by a velocity-strengthening region. These models have the same background frictional properties and general geometry of our RES-like ISM, except the diameter of the velocity-weakening region is reduced, such that the background instability ratio $D_{\text{VW}}/\tilde{h}_m^*$ is 0.75. This allows for the centered asperity to be slowly loaded in a symmetric way. CATSM 1A, 2A, and 3A have a normal stress ratio σ_p/σ_m of 5, 10, and 15, respectively. The ‘‘A’’ indicates that the characteristic slip distance ratio L_p/L_m equals 1, whereas CATSM 1B has $L_p/L_m = 0.5$ (still with $\sigma_p/\sigma_m = 5$). In each CATSM, the diameter of the patch D_p is chosen such that the instability ratio D_p/\tilde{h}_p^* is 1.0 (Table 4.3).

Comparing the resulting simulated events in the CATSMs to our usual asperity type events, for example, event S1 (Figure 4.5i), reveals that the CATSMs do preserve the main qualitative features of the shear stress changes over the event, including the larger shear stress decrease on the patch of higher normal stress (Figure 4.11a-4.11d). The corresponding shape of the ruptured area is indeed more symmetric, although there is still a systematic asymmetry related to the different rupture dynamics in the Mode II and Mode III directions. These additional sources enable the consideration of the effects of the heterogeneous stress distribution with reduced asymmetry in the source shape. The average local velocities \bar{v}_r^{loc} in the models are similar at

approximately $0.7c_s$ (comparing Figure 4.11e-4.11h to Figure 4.5f).

Next, we investigate the spectral properties of the far-field seismograms based on the CATS Models. For the fit using constant $n = 2$, the somewhat flat trend in normalized corner frequency k versus θ from the RES-like ISM (Figure 4.8a) and example asperity-type event S1 (Figure 4.9a) is preserved in the trends for the CATSMs (Figure 4.12). In addition, the trend of increasing spread of k with θ (i.e., ϕ -dependence) observed for event S1 also manifests for the CATSMs, to a higher extent for the CATSMs with higher normal stress ratio σ_p/σ_m (e.g., CATSM 3A). However, the ϕ -dependence is stronger for event S1, due to more asymmetry, as expected.

For the fit with variable n , unlike the Madariaga-like (Figure 4.7b) and RES-like ISMs (Figure 4.8b), but like the example asperity-type event (Figure 4.9b), the values of k and trends with θ have a large discrepancy from the digitized data of *Madariaga* [1976] (blue solid and red dashed lines). Again, there is significant ϕ -dependence for higher θ , but not as intense as that of event S1. (Figure 4.13)

Finally, investigating the fall-off rate n for the CATSMs (Figure 4.14), we find that the values of n are nearly constant with θ and systematically larger than 2, again with some dependence on ϕ . These features are in common with the asperity-type event, but not with the various ISMs, including our Madariaga-like ISM, RES-like ISM, and ISM of *Kaneko and Shearer* [2014] (Figure 4.10b), in which the values of n approach and then decrease below 2 as the angles θ increase above 45° .

To summarize, two features of the CATSMs are similar to the asperity-type source S1 and therefore may be characteristic features of the asperity-type events: (1) values of n systematically higher than 2 for all angles and (2) similar non-dimensional corner frequencies k for all angles.

The spherically-averaged values (Equation 4.10) of k_p and k_s for the constant $n = 2$ and variable n fits, as well as the values of n_p and n_s for a variety of representative source models are listed in Table 4.4. This list includes values for the Idealized

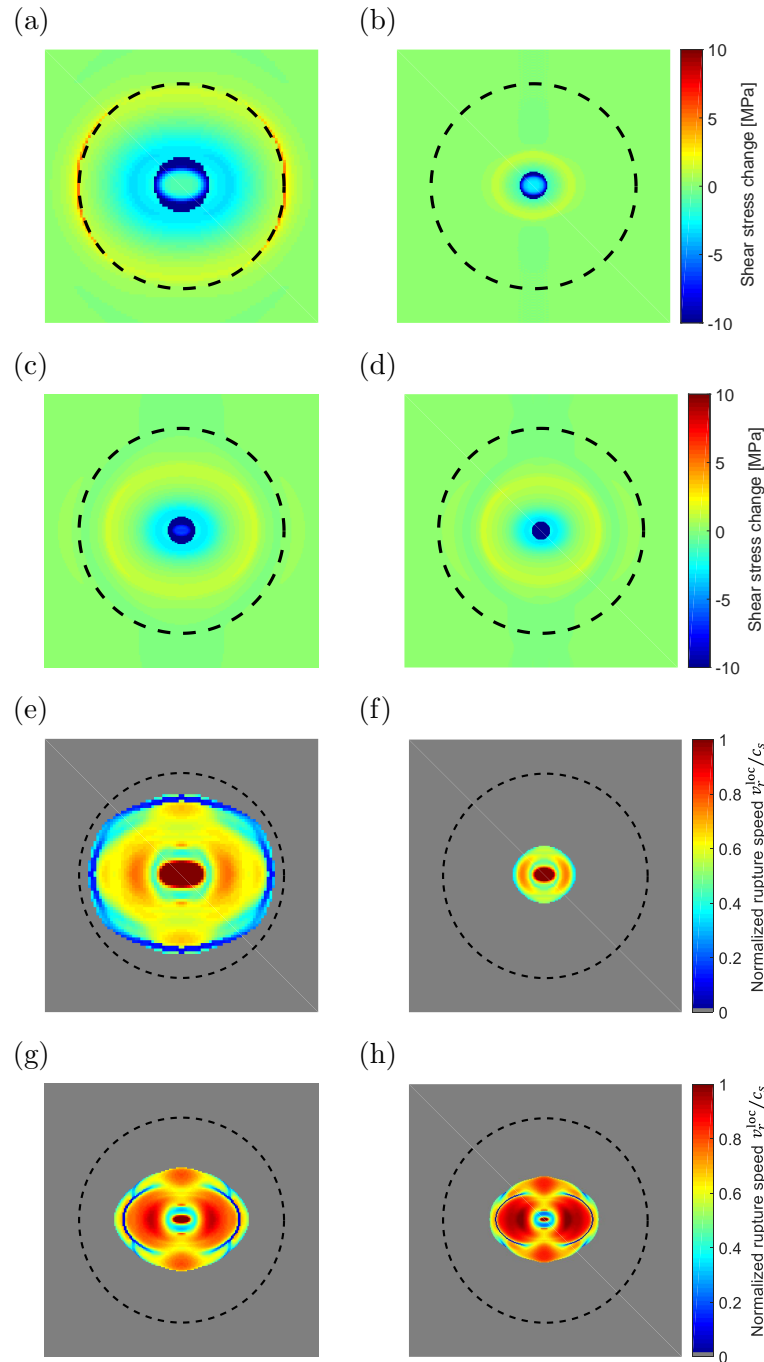


Figure 4.11.: Representative earthquake ruptures for the Centered Asperity-Type Source Models (CATSMs). The distribution of **(a)**-**(d)** shear stress change and **(e)**-**(h)** local rupture velocity v_r^{loc} normalized by the s-wave speed c_s , for a seismic event in CATSM 1A, 1B, 2A, and 3A, respectively, analogous to the second and third rows of Figure 4.5. The velocity-weakening zone is outlined with a black dashed line, and the spatial domain is cropped to focus on the source area. For **(e)**-**(h)**, the gray color indicates cells outside of the ruptured area, and the average local rupture velocity \bar{v}_r^{loc} is $0.63c_s$, $0.70c_s$, $0.65c_s$, and $0.71c_s$, respectively.

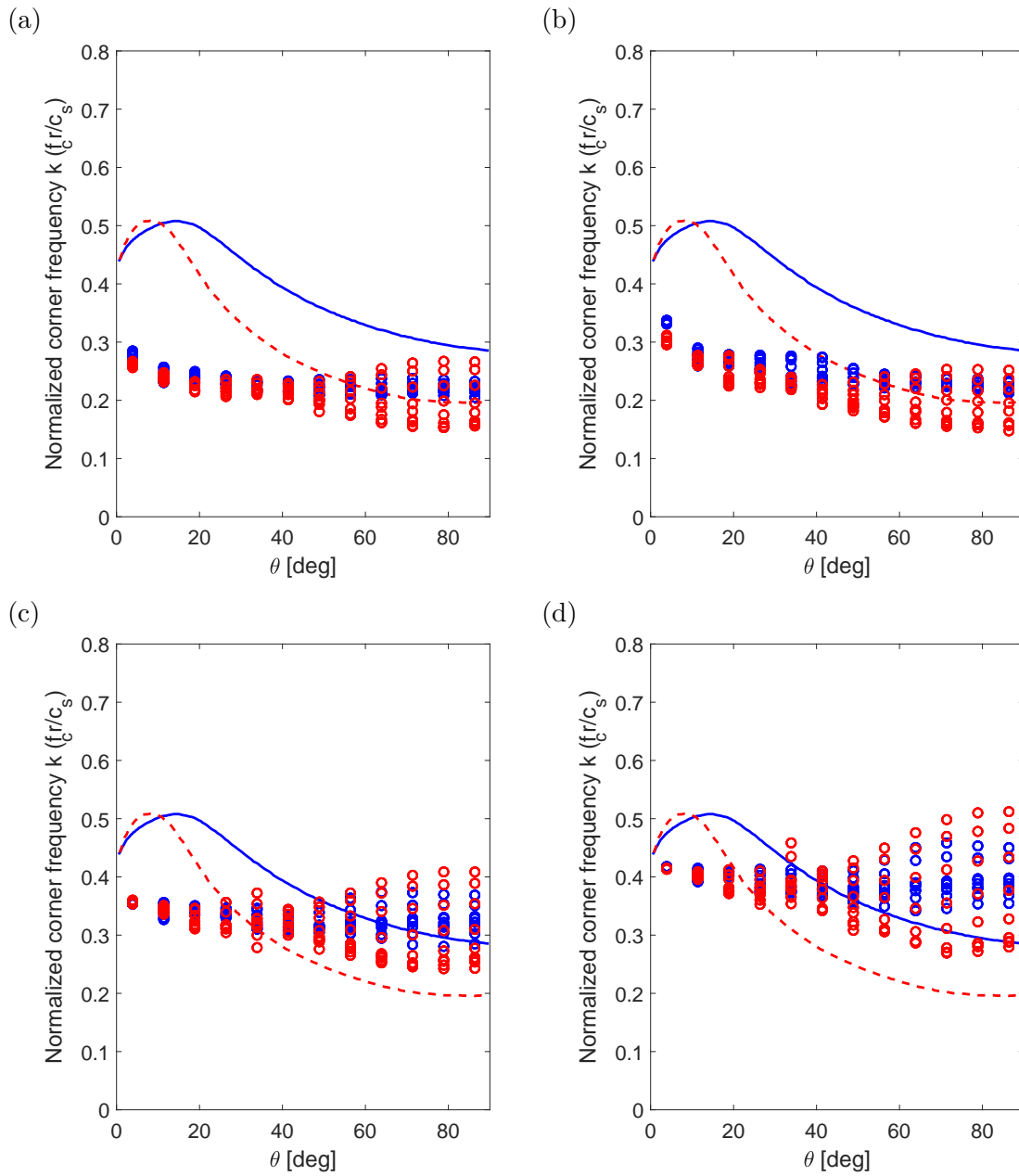


Figure 4.12.: Comparison of trends in k vs. θ for the CATSMs using the constant $n = 2$ fit. The solid blue line and dashed red line represent normalized corner frequencies k_p and k_s over θ from the digitized data of Figure 11 in *Madariaga [1976]*. The blue and red circles indicate the values of k_p and k_s for a given CATS Model over the section of the focal sphere with θ between 0° and 90° . (a) CATSM 1A. (b) CATSM 1B. (c) CATSM 2A. (d) CATSM 3A.

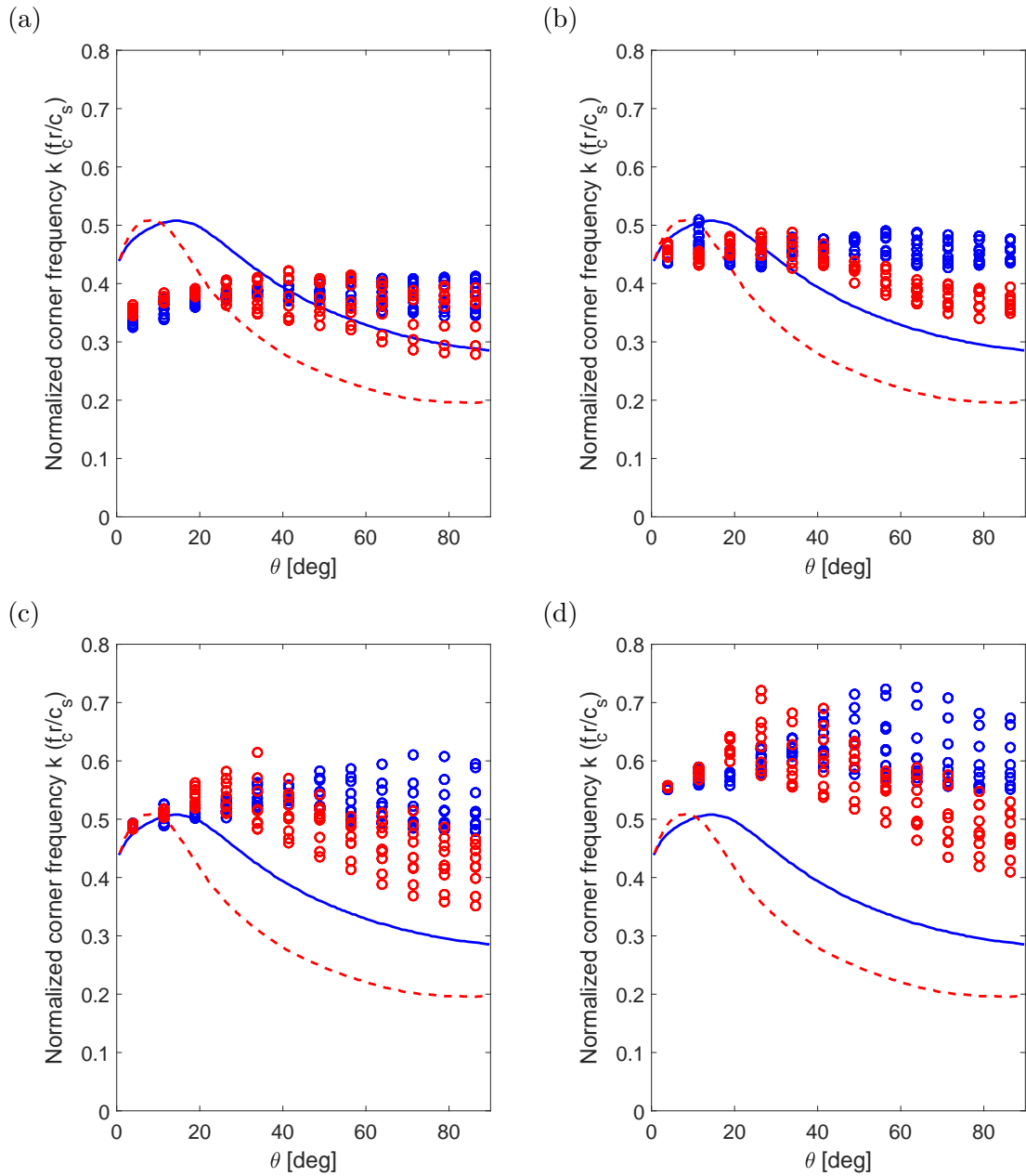


Figure 4.13.: Comparison of trends in k vs. θ for the CATSMs using the variable n fit, analogous to Figure 4.12. (a) CATSM 1A. (b) CATSM 1B. (c) CATSM 2A. (d) CATSM 3A.

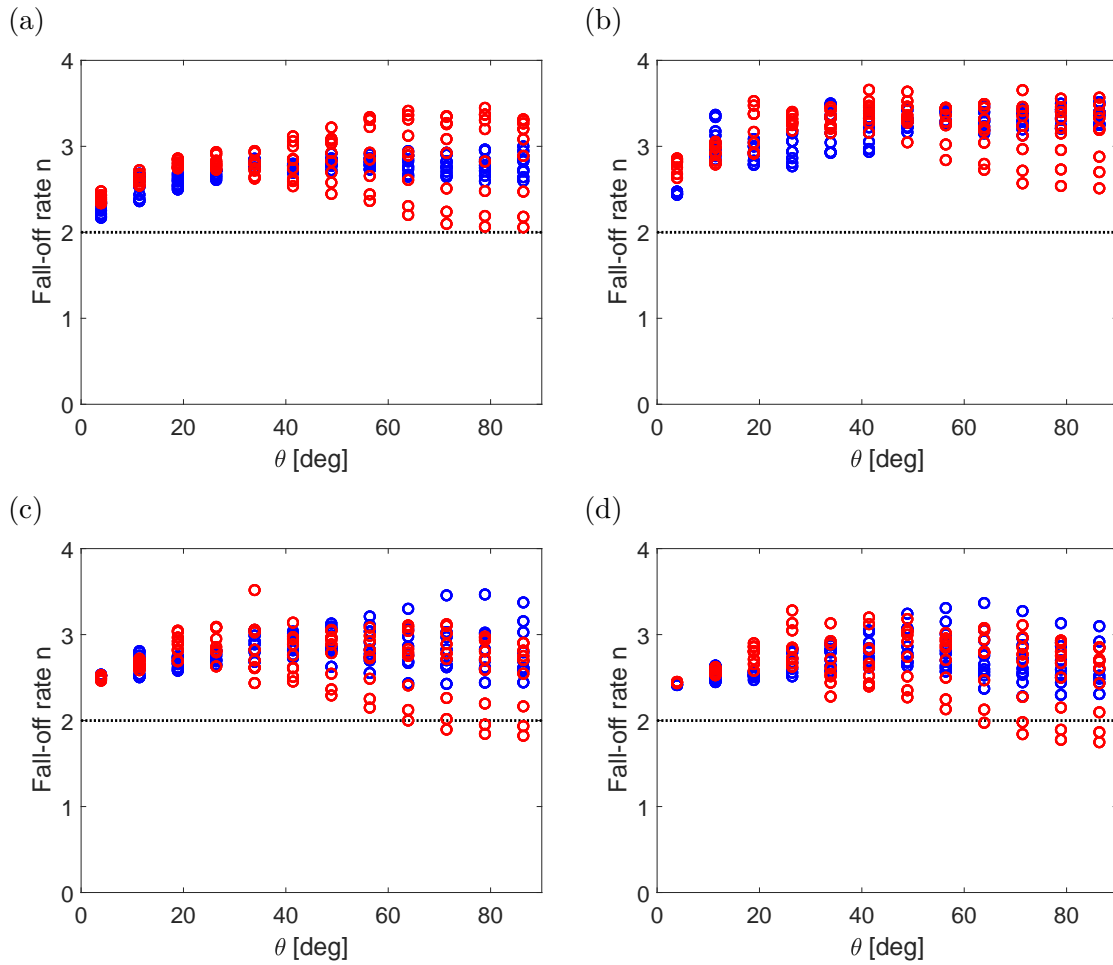


Figure 4.14.: Comparison of trends in the fall-off rate n vs. θ for a variable n spectral fit for the CATSMs, analogous to Figure 4.10. (a) CATSM 1A. (b) CATSM 1B. (c) CATSM 2A. (d) CATSM 3A.

Table 4.4.: Summary of seismologically-derived non-dimensional quantities for different source models. Reported values for the normalized corner frequency k are calculated from the spherically-averaged corner frequency \hat{f}_c over the focal sphere (Equation 4.10). Values for the spectral fall-off rate n are also spherically averaged. The second and third columns display the results of the constant $n = 2$ fit, while the fourth through seventh columns refer to the variable n fit. The quantities reported for the first nine models were calculated for a single event, whereas the values given in the last row are averages over 57 asperity-type events (3 events from 19 heterogeneous fault models from the main set). The homogeneous model refers to the fault set-up from the main set without any asperities (introduced in Figure 2.4a).

Event or model name	$k_p^{n=2}$	$k_s^{n=2}$	$k_p^{n \neq 2}$	$k_s^{n \neq 2}$	n_p	n_s	Figures
Madariaga-like ISM	0.30	0.32	0.36	0.27	2.27	1.82	4.7a, 4.7b, 4.10a
RES-like ISM	0.27	0.27	0.41	0.33	2.56	2.23	4.8, 4.10c
<i>Kaneko and Shearer</i> [2014]	N/A	N/A	0.38	0.26	2.4	1.9	4.7c, 4.10b
CATSM 1A	0.22	0.20	0.38	0.37	2.76	2.86	4.12a, 4.13a, 4.14a
CATSM 1B	0.24	0.20	0.46	0.41	3.24	3.22	4.12b, 4.13b, 4.14b
CATSM 2A	0.32	0.31	0.53	0.47	2.82	2.68	4.12c, 4.13c, 4.14c
CATSM 3A	0.39	0.36	0.61	0.54	2.72	2.63	4.12d, 4.13d, 4.14d
Homogeneous model	0.23	0.21	0.38	0.32	2.67	2.51	4.22a, 4.22c
Event S1	0.31	0.30	0.41	0.39	2.58	2.53	4.9, 4.10d
Asperity-type events	0.33	0.32	0.42	0.40	2.59	2.60	4.22

Source Models, Centered Asperity-Type Source Models, and sources from the main set in Chapter 2, which are analyzed further with respect to their seismologically-derived source properties next, in Section 4.5. The table indicates that the spherically-averaged n tend to be the highest for the asperity-type events, but perhaps not enough to be clearly distinguishable from other types, for example, our RES-like ISM. Thus, it is unlikely that the spherically average n could be used to reliably differentiate between different sources.

Note that the spherically averaged n is not the most relevant practically. For example, for a vertical strike-slip source and observations on the surface, the closest stations with the best signal-to-noise ratio will be used, emphasizing angles between 45° and 90° . The difference between n in our models is largest for that range of angles, opening the possibility that a more targeted average can be more revealing about differences between various models.

4.5. Comparison between stress drops derived from seismological and direct methods

In line with our effort to investigate the seismological properties of our asperity-type sources, we continue by calculating the seismologically-derived stress drops and comparing them to those calculated directly from the fault slip in our 3D BIM numerical simulations. Using Equation (4.6), we calculate the seismological estimates of the stress drops from the moment M_0 and corner frequency f_c from both constant n and variable n spectral fits to the p- and s-wave spectra at each station on the focal sphere, assuming $k_p = 0.32$ and $k_s = 0.21$ from the theoretical model of Madariaga (Table 4.2). This means that four seismologically-derived estimates of the stress drop are calculated per receiver location. For each of these estimates, an average of the stress drops over the focal sphere is computed, using the standard formula from *Sato*

and Hirasawa [1973] for a spherically weighted average:

$$\hat{g} = \frac{\int_0^{\pi/2} g(\theta) \sin \theta \, d\theta}{\int_0^{\pi/2} \sin \theta \, d\theta} \approx \frac{\sum_{i=1}^N g_i \sin(\theta_i)}{\sum_{i=1}^N \sin(\theta_i)} \quad (4.10)$$

of a given variable g , where i spans the stations, numbered from 1 to N , within $0 < \theta < \pi/2$. For the stress drops, as well as any other quantity that we report as a spherical average (e.g., k , n , etc.), we compute the result given by Equation (4.10). Then, in the case of stress drops and any other seismologically derived source property for which we have an equivalent “direct” value, we conduct the comparison via the ratio of the spherically-averaged seismological value to the direct one. The direct stress drop is calculated from Equation (3.1), using on-fault values of different variables, where the moment M_0 is given by Equation (4.9), and r is the effective radius of the ruptured area that is defined by the seismic velocity threshold of 0.1 m/s, as reported in Section 3.1.

The central group of seismic events analyzed in the remainder of this chapter is composed of 57 intershocks from the main set of simulations explored in Chapter 2-3. These 57 events are taken from a subset of 19 simulations that span the full range of model parameters, in terms of normal stress ratio σ_p/σ_m and patch instability ratio D_p/\tilde{h}_p^* . For each of these simulations, 3 events are chosen to represent some variety within the simulated intershocks, in terms of relative rupture extent D_r/D_p , shape of ruptured area, and relative timing within the recurrence interval of the mainshocks (i.e., occurring right after a mainshock, between two other intershocks, or right before a mainshock). For clarity in the remainder of this discussion, we call the 57 representative asperity-type events the main subset.

Further seismic events outside of the main subset are analyzed for comparison. This additional group includes our Madariaga-like ISM, RES-like ISM, and a mainshock from the homogeneous fault model (the second mainshock presented in Figure 2.4a),

and we call this group of three the homogeneous set. The final small group that we analyze here are the Centered Asperity-Type Source Models (CATSMs).

We start our comparison of stress drops by calculating the spherical average of the stress drops derived from the spectra of the p-wave for a constant $n = 2$ fit over the focal sphere, and comparing those results to the “direct” stress drops, for the main subset of asperity-type events (Figure 4.15). The seismically estimated stress drops significantly differ from the direct ones, as quantified more in the following. Furthermore, instead of the approximately constant stress trend in direct stress drop with respect to normal stress on the patch, the seismologically-derived stress drops for this standard fitting approach increase approximately linearly (Figure 4.15a), although within the reasonable values between 1 and 10 MPa.

To explore the reasons behind the difference in trends from the seismologically and directly derived stress drops, we employ the homogeneous set and CATSMs for reference, as they are less complex than the asperity-type sources of the main subset. Considering the same type of quantities as in Figure 4.15a, the seismological stress drops for the homogeneous set range between a fraction of 0.4 (homogeneous mainshock) and 0.9 (Madariaga-like ISM) of the direct stress drops (Figure 4.16a). Similarly, the stress drops for the CATS Models with $\sigma_p/\sigma_m = 5$ are also underestimated by the seismological analysis, but, as the normal stress ratio σ_p/σ_m is increased, the seismological stress drops also increase linearly, and even overestimate the direct stress drop by a factor of 1.9 for the CATSM with $\sigma_p/\sigma_m = 15$. For the stress drop comparison from the remaining three types of seismological analysis (variable n fit for the p-wave, constant $n = 2$ fit for the s-wave, and variable n fit for the s-wave), we continue to see a linearly increasing trend for the “A” CATS Models (i.e., with $L_p/L_m = 1$), with even further overestimations of the direct stress drops, and now the stress drops for the homogeneous set are also overestimated. Interestingly, the stress drop comparison for the two CATSMs with the same σ_p but different L_p (CATSM 1A

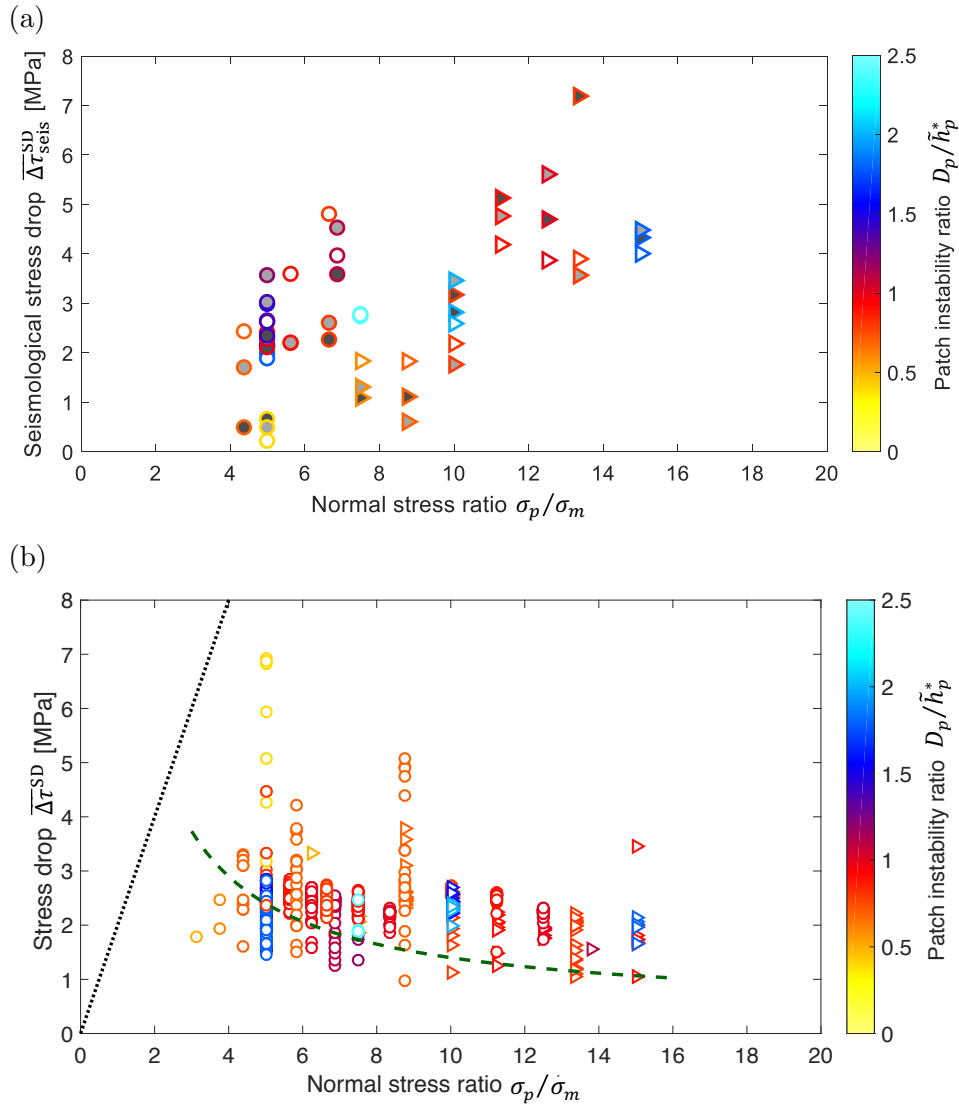


Figure 4.15.: Comparison of trends in stress drop with patch normal stress ratio calculated seismologically and directly. **(a)** Seismological stress drop $\overline{\Delta\tau}_{seis}^{SD}$ spherically averaged over the focal sphere derived from the p-wave spectrum for the constant $n = 2$ fit as a function of the patch normal stress σ_p (recalling that the background normal stress $\sigma_m = 10$ MPa was held constant). The plotted data is from the main subset: three asperity-type events from the subset of 19 simulation of the main set are identified in the same way as the majority of figures in Chapter 3, using triangles for $L_p/L_m = 1$ and circles for $L_p/L_m = 1/2$, respectively, with the outline color indicating the patch instability ratio D_p/\tilde{h}_p^* . The fill colors dark gray, light gray, and white effectively number the three representative events per simulation. **(b)** Stress drops from the main set in Figure 3.1, repeated here for comparison with (a). Unlike the actual stress drops in (b), which are calculated directly from fault distributions in our simulations, the stress seismologically-derived stress drops show a linearly increasing trend with the patch normal stress.

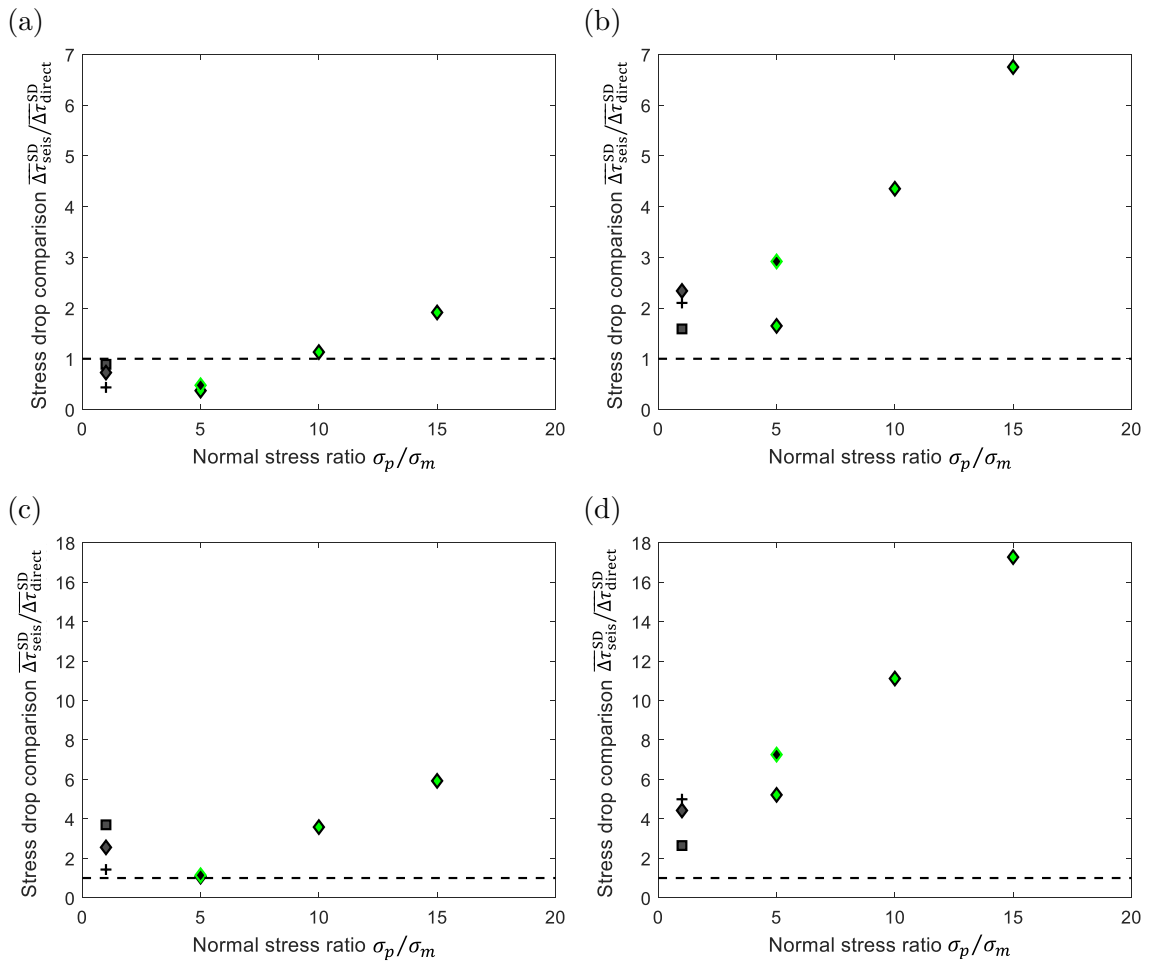


Figure 4.16.: Comparison of the seismologically-derived to the direct stress drop for the homogeneous set and CATSMs. In this as well as many of the upcoming figures, the marker identity scheme is as follows: the homogeneous set is identified by a dark-gray fill and black outline, with markers for the Madariaga-like ISM, RES-like ISM, and homogeneous mainshock shown as a square, diamond, and plus, respectively; the CATSMs are identified by diamond markers, with a green fill and black outline for CATSM 1A-3A, and the reverse color scheme for CATSM 1B. (a) and (b) show the stress drop comparison of $\overline{\Delta\tau}_{\text{seis}}^{\text{SD}}$ to $\overline{\Delta\tau}^{\text{SD}}$ for the p-wave spectra, using the constant $n = 2$ and variable n fit, respectively. (c) and (d) are analogous to (a) and (b), for the s-wave spectra. A black dashed line highlights the ratio of 1, which would indicate a perfect match between the spherically-averaged seismological and directly derived quantities.

and 1B) result in almost identical values when calculated from the constant $n = 2$ fit (Figure 4.16a and 4.16c), but they are no longer similar for the variable n fit (Figure 4.16b and 4.16d), specifically with the CATSM with the smaller patch nucleation size estimate \tilde{h}_p^* having a higher overestimation of the stress drop. This implies that the constant $n = 2$ versus variable n spectral fitting approaches interpret the heterogeneity of the CATSMs differently, with the constant $n = 2$ fit not distinguishing the effects of non-constant characteristic slip distance L . Still, overall, this trend of increasingly overestimated stress drops with a dependence on the patch normal stress ratio σ_p/σ_m by the seismological analysis for the CATSMs (Figure 4.16) sheds light on the similar trend observed for the asperity-type sources of the main subset.

As expected based on our previous analysis (Figure 4.15a and Figure 4.16), when we plot the stress drop comparison $\overline{\Delta\tau}_{\text{seis}}^{\text{SD}}/\overline{\Delta\tau}^{\text{SD}}$ for all of the models in the homogeneous set, CATSMs, and main subset together, most of the stress drops are overestimated across the four types of seismologically-derived stress drops (from combination of p-wave and s-wave spectra, constant and variable n fits) (Figure 4.17). Note that the small group of events with underestimated stress drops are from models with $D_p/\tilde{h}_p^* \approx 0.5$, with the events being barely seismic by our velocity threshold of 0.1 m/s. These are also the events with higher direct stress drops than the majority of the main set. The overall overestimation of the stress drop is particularly apparent for calculations based on the s-wave spectra and, in all cases, the results continue to suggest that the seismological overestimation of the stress drops increases with increasing normal stress ratio σ_p/σ_m . As such, as we investigate the methodological reasons for this overestimation, we focus on analyzing quantities derived from the s-wave spectra.

Let us consider the individual ingredients from the seismological estimates that are combined to produce a stress drop estimate in Equation (4.6), which are the seismic moment and the source dimension. It is known that the seismic moment is robustly determined from the spectral analysis, and our study confirms that, as the

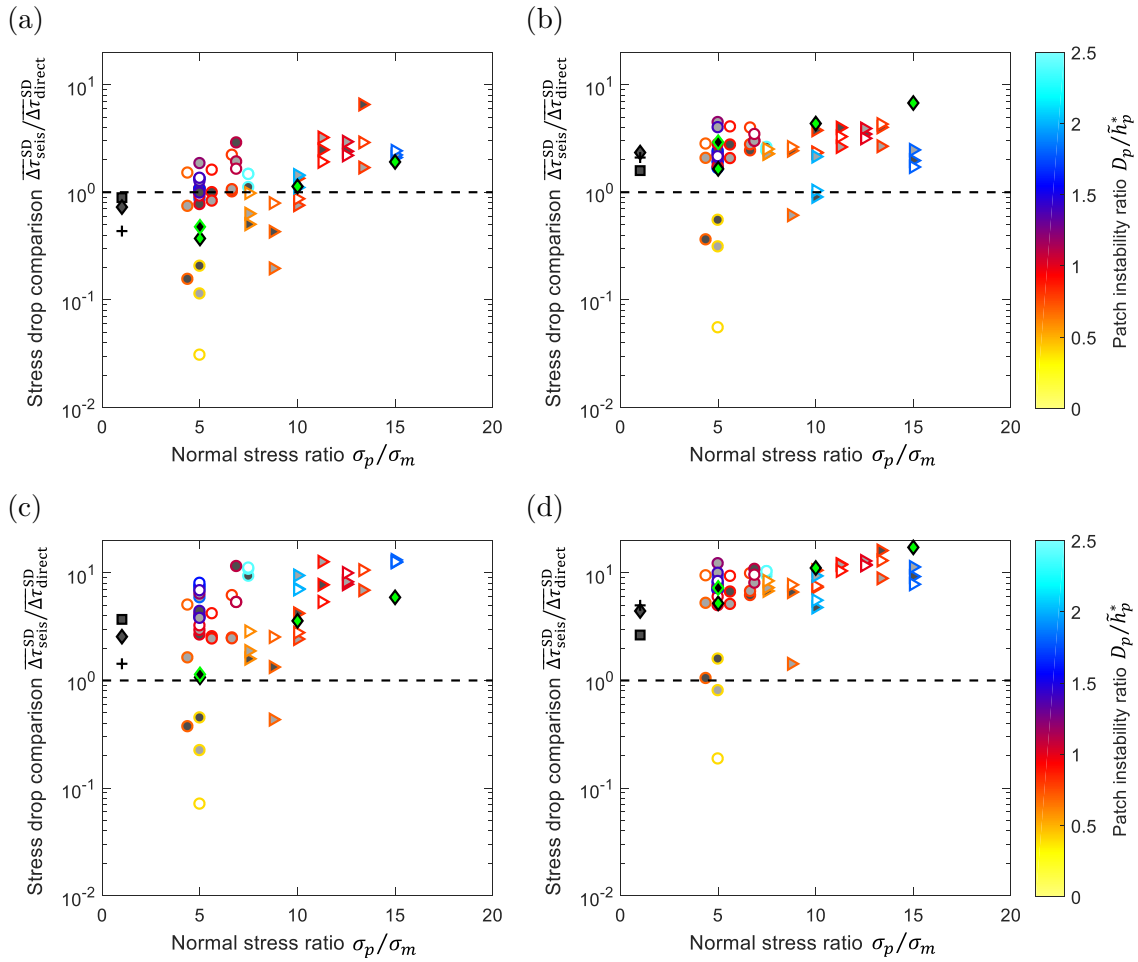


Figure 4.17.: Comparison of seismologically-derived to direct stress drops. This figure is analogous to Figure 4.16, except now we also include the data from the main subset, and the stress drop comparison $\overline{\Delta\tau}_{\text{seis}}^{\text{SD}}/\overline{\Delta\tau}_{\text{direct}}^{\text{SD}}$ is given on a log scale from 0.01 to 20. For the asperity-type events in the main subset, as in Figure 4.15a, the marker shape and outline color indicate L_p/L_m and D_p/\tilde{h}_p^* , respectively. (a) and (b) show the stress drop comparison for the p-wave spectra, using the constant $n = 2$ and variable n fit, respectively. (c) and (d) are analogous to (a) and (b), for the s-wave spectra. A black dashed line highlights the ratio of 1, which would indicate a perfect match between the seismologically and directly derived quantities.

seismically estimated moment matches well with the moment calculated directly from our simulations (Figure 4.18). The source dimension is considerably more uncertain, as it is calculated via Equation (4.5), based the corner frequency determined from the chosen spectral fitting and the assumed value of k from the chosen theoretical model. Any deviation in the seismological estimate of the source radius from the

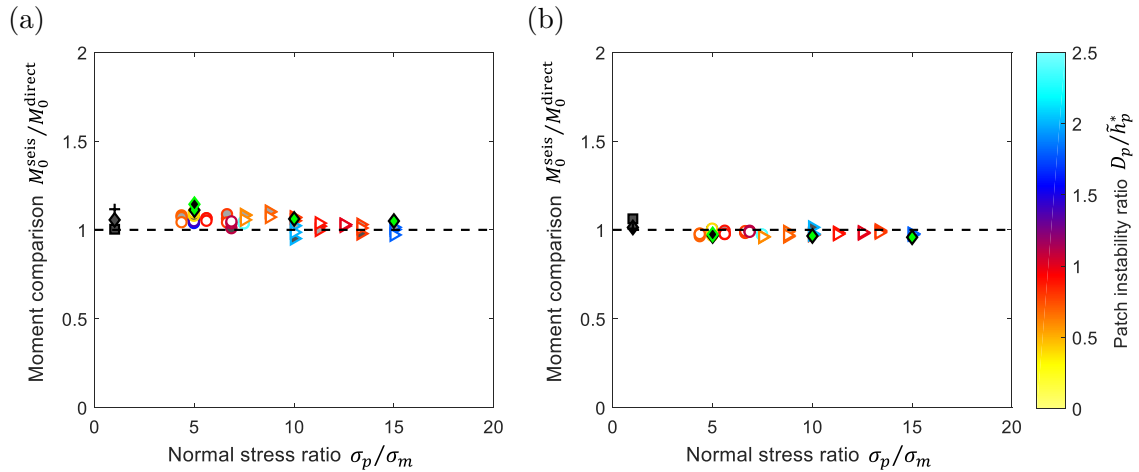


Figure 4.18.: Comparison of seismic moment calculated from the s-wave spectra to the direct calculation from our simulations. (a) and (b) show the comparison for the constant $n = 2$ and variable n fit, respectively, both of which result in a good estimate.

true source radius is cubed in calculating the stress drop. Therefore, small differences in radius can cause large discrepancies in stress drop. As given by the examples of the constant $n = 2$ and variable n fit to the s-wave spectra (Figure 4.19), the seismologically-derived radius typically underestimates the direct calculation of the source radius, for both the heterogeneous and homogeneous source models. From the variable n fit, for example, the radius is usually underestimated by a factor of 2, which would translate into a factor of 8 difference in stress drop.

Recalling the theory behind the idealized source models, the seismic rupture is assumed to start at a point in the center of a circular seismogenic region and propagate axi-symmetrically at a constant rupture speed v_r . This means that the assumed source radius is given by $r = v_r t_d$, where t_d is the source duration. The duration is linked to

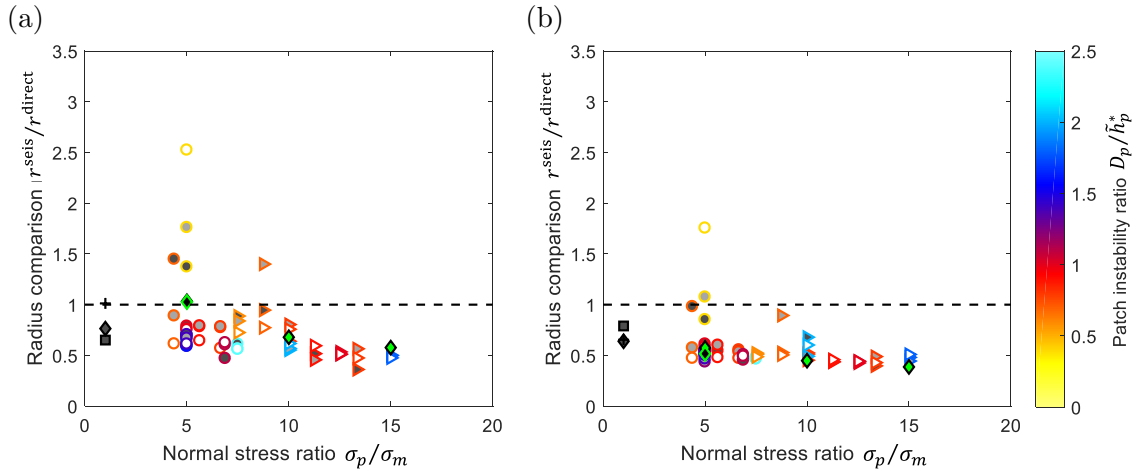


Figure 4.19.: Comparison of source radii calculated from the s-wave spectra to the direct calculation from our simulations. **(a)** and **(b)** show the radius comparison for the constant $n = 2$ and variable n fit, respectively.

the corner frequency f_c . In the standard analysis, the rupture velocity is assumed to be $0.9c_s$. The global rupture velocity from our simulations, calculated as $v_r = r/t_d$, is typically smaller by a factor of 2. As such, the standard analysis would overestimate our rupture velocities by about a factor of 2, just by the typical assumption. We can also compare the seismologically estimated source durations to the direct duration from the simulations. The results show that the source duration is systematically underestimated (Figure 4.20). In the case of the corner frequencies derived from the variable n fit to the s-wave spectra, the source duration is typically underestimated by approximately a factor of 4.

In summary, the seismological calculations of the source properties of our asperity-type sources, using the theoretical model of *Madariaga* [1976] for $v_r = 0.9c_s$, typically overestimate the rupture velocity of the source v_r by a factor of 2 and underestimate the duration t_d by a factor of 4, which combines to underestimate the source radius by a factor of 2 and hence overestimate the stress drops by a factor of 8. These are representative values that explain the bulk of the discrepancy, with the mis-estimation systematically varying for the sources with different degree of heterogeneity.

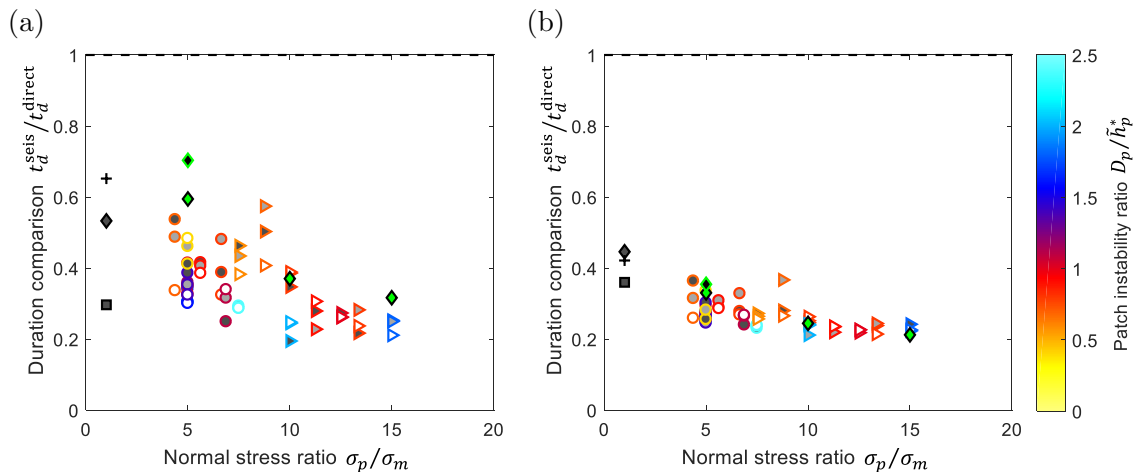


Figure 4.20.: Comparison of source durations calculated from the s-wave spectra, given by $t_d = k/(0.9f_c)$, to the direct calculation from our simulations. **(a)** and **(b)** show the duration comparison for the constant $n = 2$ and variable n fit, respectively.

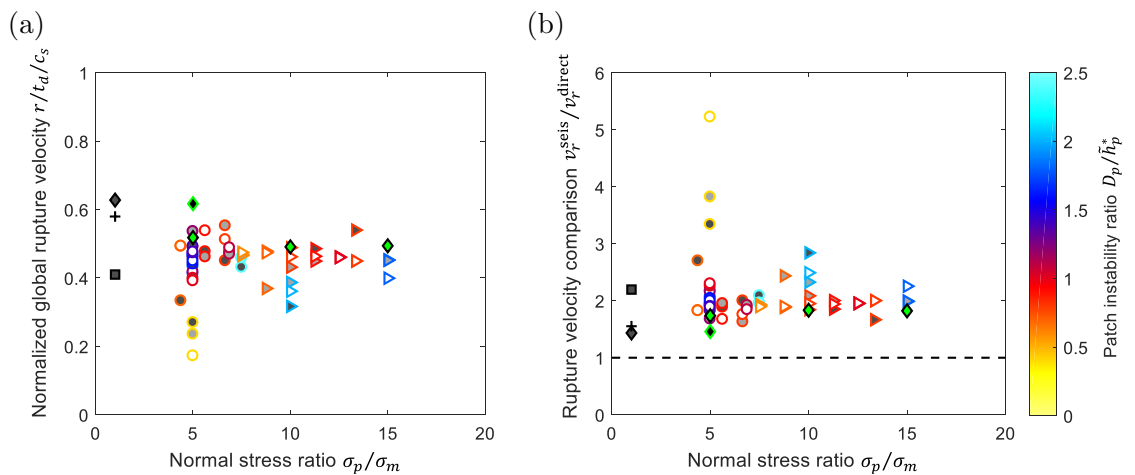


Figure 4.21.: Comparison of the seismologically assumed rupture velocity $v_r = 0.9c_s$ and the direct global rupture velocity. **(a)** The global rupture velocity as a fraction of the shear wave speed c_s , calculated directly from the ruptured radius r and duration t_d . **(b)** Comparison of the rupture velocity assumed in the seismological analysis to the one in (a), calculated directly from our simulations.

4.6. Exploration of potentially characteristic features

Armed with the methods for producing synthetic seismograms and calculating the seismologically derived source properties of our simulated seismic events, we consider potentially characteristic seismological signatures of our asperity-type sources. To do so, we analyze the p- and s-wave displacement spectra over the focal sphere as well as for single receiver stations, when appropriate, and calculate spherically-averaged quantities (Equation 4.10). As discussed in Section 4.4 and with some of the values listed in Table 4.4, two quantities of interest are the spherically-averaged normalized corner frequency k and the fall-off rate n . In practical scenarios, the source radius is not known from other observations and, hence, some value of k needs to be assumed in order to derive source properties from the displacement spectra. This motivates our emphasis on continuing to explore trends in fall-off rate n , as it can be readily calculated from the seismograms.

As can be seen from the values listed in Table 4.4 and discussed in Section 4.4, the first trend in seismological properties that could be characteristic for asperity-type source is fall-off rates n that are significantly higher than 2 and higher than those typically observed for more homogeneous sources. As noted at the end of Section 4.4, the spherically averaged values may not be the most relevant for comparing different models, as they are not represented in observations and tend to minimize the difference between the models we considered, and we plan to consider other averaged quantities in the future.

To explore further whether higher spherically averaged n are characteristic for asperity-type models, we plot them against properties inherent to the asperity-type sources (Figure 4.22), such as the normal stress ratio σ_p/σ_m (Figure 4.22a and 4.22c) and the relative rupture extent D_r/D_p (Figure 4.22b and 4.22d). We find that the spherically averaged values of n seem to decrease with the increasing σ_p/σ_m and D_r/D_p . Note that σ_p/σ_m and D_r/D_p are related (Figure 3.4). This decrease in n

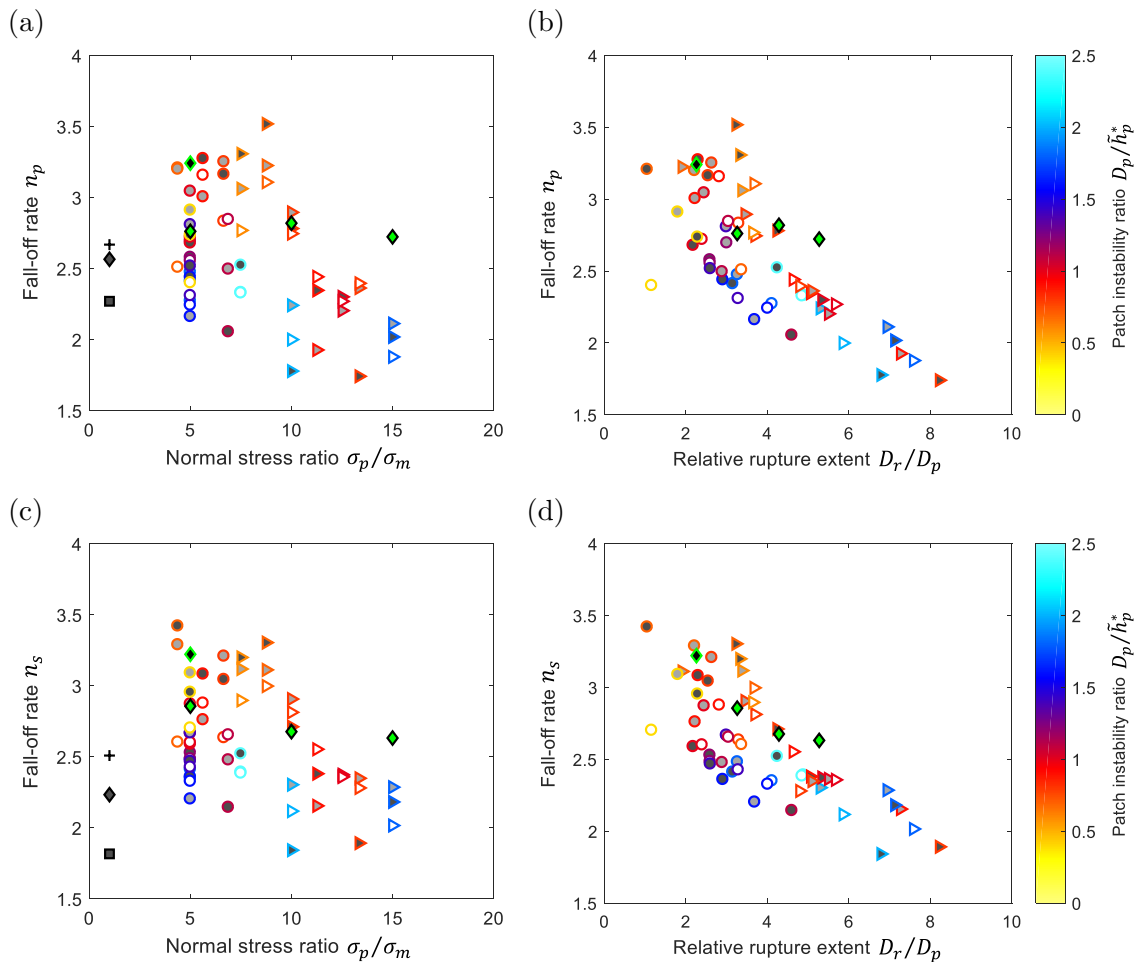


Figure 4.22.: The dependence of the spherically averaged spectral fall-off rate n on the normal stress ratio and relative rupture extent for the same set of sources that were analyzed in Section 4.5, i.e., the homogeneous set, CATS Models, and main subset based on (a)-(b) p-waveforms and (c)-(d) s-waveforms. The identity scheme matches Figure 4.17. There is no homogeneous set data included in the subplots against D_r/D_p , because D_p is undefined for homogeneous sources.

may be due to the larger relative rupture extent making the heterogeneity in stress change over the ruptured area less noticeable, as the patch of higher normal stress makes up a smaller portion of the ruptured area. Our fitting procedure adds to this possibility, since the spectral fit only considers frequencies up to 10 times higher than the corner frequency. This exercise further confirms that the spherically averaged n are not promising as the distinguishing factor between different source models.

Another quantity of interest to explore is the p-to-s corner frequency ratio f_c^p/f_c^s . As indicated in column 3 of Table 4.2, the expected p-to-s corner frequency ratio is typically around 1.5 for an assumed rupture speed of $v_r = 0.9c_s$. Additional studies have also reported values of f_c^p/f_c^s greater than 1. For example, *Molnar et al. [1973]* reported that f_c^p is systematically larger than f_c^s , and that values of the corner frequency ratio measured teleseismically typically fall between 1 and 2. *Abercrombie [1995]* used a set of four models for fitting the spectra and reported average values of f_c^p/f_c^s around 1.3. In the study of *Yang and Ben-Zion [2016]*, f_c^p/f_c^s was reported to be approximately 1.5, and they also saw values greater than 2.

In contrast, for our asperity-type events, the values of the p-to-s corner frequency ratio f_c^p/f_c^s are closer to 1 (Figure 4.23). For the variable n fit, the values of f_c^p/f_c^s for the homogeneous set (i.e., Madariaga-like ISM, RES-like ISM, and homogeneous mainshock) are systematically higher than the values for all of the usual asperity-type events (main subset) and the CATS Models (Figure 4.23c). Furthermore, the trend in f_c^p/f_c^s for the asperity-type events persists and even improves with both increasing σ_p/σ_m and D_r/D_p .

While all of the values of the spherically-averaged f_c^p/f_c^s for the combination of sources from the main subset and CATSMs range from 1.00 to 1.25 for the constant $n = 2$ fit and from 0.92 to 1.18 for the variable n fit (Figure 4.23), the value calculated for the Madariaga-like ISM falls even lower for the constant $n = 2$ fit, and the value for the RES-like ISM is not far behind (Figure 4.23a), requiring further investigation,

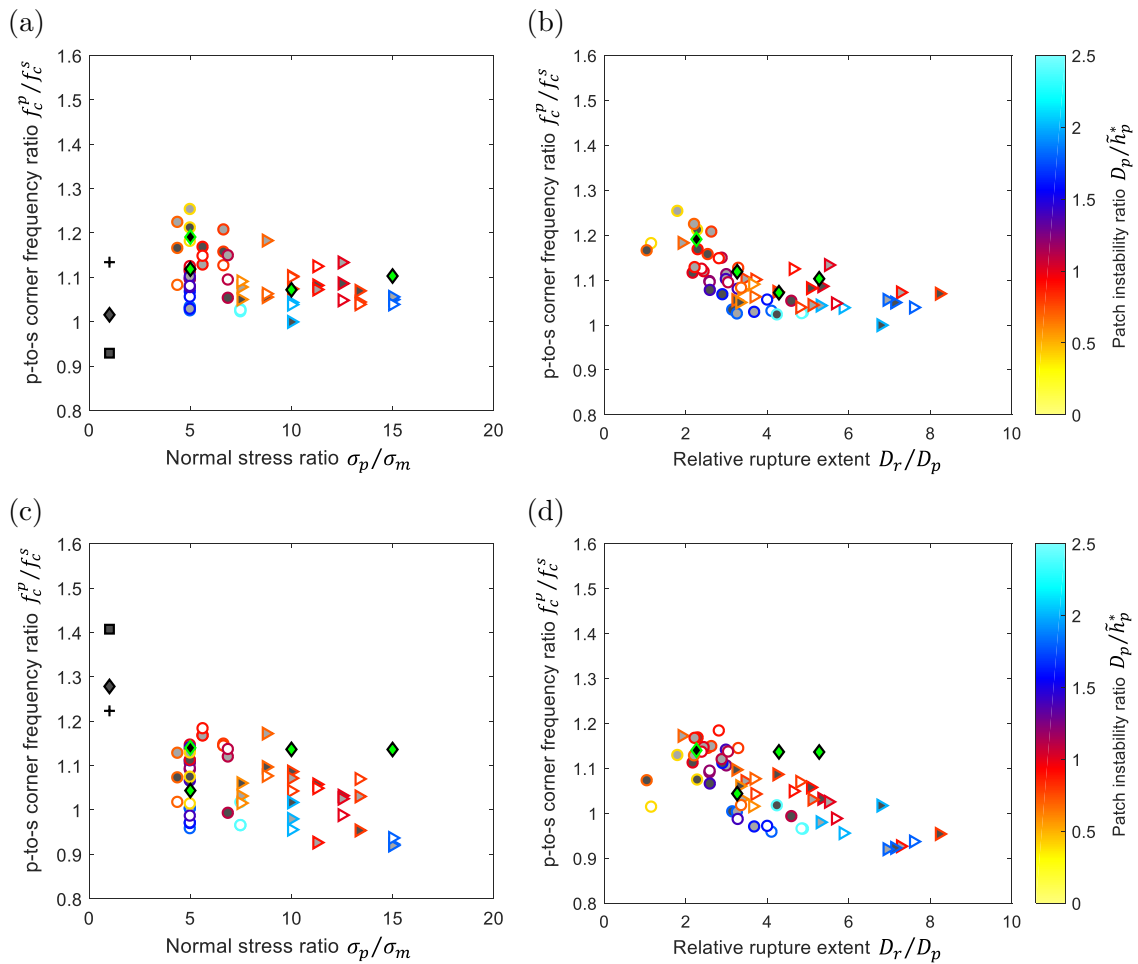


Figure 4.23.: The dependence of p-to-s corner frequency ratio f_c^p/f_c^s on patch properties. (a) and (b) show the spherically-averaged value of f_c^p/f_c^s derived using the constant $n = 2$ fit versus the normal stress ratio σ_p/σ_m and relative rupture extent D_r/D_p , respectively. (c) and (d) are analogous to (a) and (b), except f_c^p/f_c^s was derived using the variable n fit. The corresponding values of n for this fit are shown in Figure 4.22.

in particular with respect to using fixed n versus constant n spectral fits. Overall, there is potential for the low p-to-s corner frequency ratios f_c^p/f_c^s being characteristic for asperity-type events.

For both candidates for potentially characteristic seismologically observable features of asperity-type events that we have identified so far – namely, high fall-off rate n and low p-to-s corner frequency ratio f_c^p/f_c^s – future work involves exploring the connection between these trends and properties of the source for more relevant station averages as well as investigating whether or not these spectral features are uniquely related to asperity-type events.

5. Conclusions and outlook

5.1. Conclusions

5.1.1. Heterogeneous fault models and the mechanics of intershocks

The rate-and-state fault models with patches of elevated normal stress can indeed produce isolated smaller-scale seismicity – intershocks – driven by the slow slip of the mainshock nucleation, for reasonable parameters. These patch-initiated seismic events represent both foreshock-like and aftershock-like events. For intershocks to occur, i.e., for smaller-scale seismicity to remain isolated from the mainshocks as distinct events, we find that a significant separation in nucleation length scales is needed. In our models, this is achieved by a significant increase of normal stress on the patch, by up to a factor of 15, and, in some cases, and additional decrease in the characteristic slip distance.

Contrary to the expectation that much higher normal stress on the patch would produce unreasonably high stress drops, our intershock sources produce reasonable stress drops that are nearly constant over the explored range of the patch normal stress. Moreover, they match the typical stress drops observed in the laboratory and the field. This potentially surprising but crucial behavior is achieved by two main mechanisms: (1) ruptures extending into the surrounding region, and (2) aseismic

stress release just prior to the start of the seismic event.

Our setup of velocity-weakening patches within a larger velocity-weakening region allows seismic events originating on patches of higher compression to extend significantly outside of the patch. The rupture extent clearly depends on the instability ratio of the patch. In addition, our simulation results show that the rupture dimension relative to the patch size increases with increasing patch normal stress. This extended rupture dimension controls the stress drop, particularly for patches with highly elevated normal stress.

Most significantly for patches that are similar in dimension to their nucleation size, aseismic stress release also contributes to the reasonable stress drops. Due to the slow pace of this stress release, these patches are able to alleviate some of the accumulated shear stress in a way that is not included in the seismic stress drop calculation.

The appropriate separation in length scales for producing isolated smaller-scale events, i.e., intershocks, depends on various interconnected factors, such as nucleation sizes and instability ratios of both the patches and surrounding seismogenic region, intershock rupture extent, mainshock nucleation size relative to the intershock rupture extent, and the shear stress distribution left over from the history of past events. Nonetheless, the two quantities that we have found to be the most relevant (though incomplete) in controlling the occurrence and isolation of intershocks are the patch instability ratio D_p/h_p^* and the isolation ratio h_m^*/D_r . The former influences the potential for seismic rupture and the capacity for a healthy dynamic rupture, and the latter influences the potential for smaller-scale dynamic events to end before they immediately trigger and thereby blend into the mainshock. Additionally, although we did not explicitly explore patch spacing in this study, it is reasonable to assume that patch spacing would play a role in the occurrence of intershocks, with closely-spaced patches potentially turning into compound events and far-spaced patches being effectively ignored by the mainshock nucleation.

The success of our model in producing two separate scales of seismic events within the same seismogenic zone, with the smaller-scale events having reasonable stress drops despite the heterogeneous properties, provides important insight into the conditions suitable for the occurrence of intershocks on both laboratory and natural faults. In particular, our results suggest that faults with observable intershocks likely have a relatively large mainshock nucleation size as well as localized areas with much smaller nucleation size and properties corresponding to a relatively low instability ratio.

5.1.2. The seismological interpretation of asperity-type events

The current standards in the seismological analysis of microseismicity today are based on kinematically simple sources that envision an axi-symmetric propagation of shear rupture from a point into a circular domain with constant rupture speed and constant shear stress drop. Our asperity-type sources are different and include a heterogeneous stress change over the ruptured area, a non-constant rupture velocity, and sometimes also non-symmetric and non-circular rupture area. That is why we have explored the influence of the variations in the source characteristics on seismic source spectra and the resulting seismologically-derived properties.

While our main goal is to consider the seismically-derived properties of the asperity-type seismic sources, our study has revealed significant inconsistencies in the assumptions of the commonly used analysis based on *Madariaga [1976]*, as well as highlighted the fact that the idealized model envisioned by the analysis cannot be exactly realized physically. We have explored two versions of the idealized models based on rate-and-state friction models, expanding the work of *Kaneko and Shearer [2014]* and *Kaneko and Shearer [2015]* to update the classic idealized source model of *Madariaga [1976]*.

Our investigation shows that the current seismological methods would misinterpret our microseismicity sources. The average rupture speed of our sources varies, with

the average values of about $0.5c_s$ for most sources, hence the standard assumption of $0.9c_s$ would overestimate the rupture speed by a factor of about 2. The seismologically estimated durations of the sources from the corner frequency of the spectral fits tend to be much lower than the actual durations, by a factor that varies from 2 to 4 for the fit based on the procedure developed in *Madariaga [1976]* for the p-wave spectrum and the assumption of the spectral fall-off rate of $n = 2$, which is the most commonly used approach. The two problems partially cancel out when the average source radius is computed as their product, with the average discrepancy in the source radius being a factor of 2. Still, the resulting seismologically estimated stress drops vary from 0.2 to 7.2 MPa. Moreover, the seismological estimates overall increase with the increasing normal stress ratio σ_p/σ_m . As a reminder, the moment-based stress drops calculated directly from the slip on the fault in our 3D BIM simulations are nearly independent from the patch normal stress and cluster around 2-3 MPa. The discrepancies are even larger for the analysis based on the s-wave spectrum as well as when n is not fixed to be 2 but rather found as part of the fit.

We have identified several differences between the spectra based on the standard source models and our asperity-type sources that may potentially be characteristic. In our study, the normalized corner frequency k has a significantly different variation with the angle θ that describes the direction between the normal to the source and the receiver. The spherically averaged fall-off rate n is approximately 2.6 for our sources, which is higher than the usual assumption of $n = 2$. However, the high value of n does not systematically hold for all asperity-type sources and other sources we have studied also have n higher than 2. Fortunately, due to the fault-station geometries, typical observations may be sensitive to averages over the part of the focal sphere that may maximize the difference in n , and this is a subject for our future work. The average p-to-s corner frequency ratio f_c^p/f_c^s is approximately 1.0 for the asperity-type sources, which is lower than the standard value of, for example, 1.52 from the

commonly-used model of *Madariaga* [1976] with $v_r = 0.9c_s$.

Note that our analysis does not include nonlinear path effects and noise, and further study is required to identify their effects and determine which differences can be identified in their presence. However, increasingly dense and sensitive seismic networks, including in boreholes, open the possibility that more detailed analysis of the seismic data may be able to uncover some of these differences.

5.2. Linking to natural faults

While the spatial scale and parameters in our simulations are inspired by laboratory experiments [*McLaskey and Kilgore*, 2013; *McLaskey et al.*, 2014], the qualitative features and trends in our results should be relevant to natural faults. In line with the growing perspective that foreshocks are created by the interaction of slow slip with favorable fault patches [*Kanamori and Stewart*, 1978; *Jones and Molnar*, 1979; *Dodge et al.*, 1995; *McGuire et al.*, 2005; *Kato et al.*, 2012; *Bouchon et al.*, 2013; *Brodsky and Lay*, 2014], we have shown that the scenario of asperity-type patches of elevated compression as initiation locations for foreshocks driven by the larger-scale nucleation process is indeed physically plausible. Natural faults in the laboratory and the field likely have much more distributed and varied heterogeneity than that assumed in our models, but only the spots where properties are favorable for producing smaller-scale seismicity are seen via intershocks.

Our results suggest that faults with numerous foreshocks likely have properties corresponding to a relatively large background nucleation size h_m^* in relation to the foreshock rupture size D_r ; otherwise, the potential foreshocks would just grow into the main event. The microseismicity interpreted as foreshocks on natural faults typically have moment magnitudes M_w of 2-3, which corresponds to the source dimensions around 100-400 m. The larger-scale nucleation size, then, has to be approximately

1-8 km for cases with foreshock sequences. In the context of rate-and-state friction with laboratory-based properties and nucleation estimates given by Equation 2.3, such large nucleation sizes require sufficiently low effective normal stresses, of the order of 1 MPa or even less, depending on the rate-and-stat properties. For example, given the typical values for rate-and-state properties based on laboratory findings and also used in models that reproduce microseismic observations [e.g., *Chen and Lapusta, 2009; Lapusta and Liu, 2009*, and references therein] of $a = 0.01$, $b = 0.014$, and $L = 100 \mu\text{m}$, the effective normal stress needs to be approximately 5-0.5 MPa for mainshock nucleation sizes of 1-8 km, respectively.

While our lab-motivated models thus far have not involved fluids, and therefore effective normal stress and normal stress have been synonymous, natural faults are often permeated with fluids, with the effective normal stress being the elastodynamic normal stress minus the pore pressure. To achieve such low effective normal stresses at seismogenic depths, the faults must have the pore fluid pressure much beyond the hydrostatic level. Such high pore pressure conditions can be achieved locally around faults, as the faults may serve as conduits to fluids generated by dehydration reactions at depth [e.g., *Rice, 1992; Liu and Rice, 2007*], because of the lower fault-parallel permeability due to persistent slip and near-fault damage. In addition, the state of highly elevated pore pressure may be transient, since the pore fluid motion may be episodic.

In fact, the relatively recently discovered slow slip transients in subduction zones [*Dragert et al., 2001; Schwartz and Rokosky, 2007; Peng and Gomberg, 2010*] potentially provide evidence for at least occasional fault conditions in which the nucleation size is quite large. In the slow slip transients, fault slip rates spontaneously accelerate to values 2-3 orders of magnitude above the plate rate but remain 5-6 orders of magnitude below the seismic slip rates. These quasi-static events can be modeled essentially as a protracted large-scale nucleation process that migrates along the

fault [*Liu and Rice, 2007; Segall et al., 2010*]. The transients can travel hundreds of kilometers along the fault but occupy a width of the order of 10 km at the bottom of the seismogenic zone, suggesting the nucleation size estimate of that order. Some of these slow slip events are accompanied by a seismic signal called tremor, which is interpreted as a myriad of barely seismic events (called low-frequency earthquakes) triggered by the slow slip and occurring so frequently that their signals overlap [e.g., *Shelly et al., 2006, 2007; Peng and Gomberg, 2010*]. Earthquake nucleation with foreshock sequences, then, may be a somewhat smaller-scale version of these aseismic transients that occurs in the presence of fault heterogeneity suitable for producing more traditional microseismicity.

Although we did not thoroughly explore it in this study (Chapter 2-3), the sufficiently fast creeping rate may be an important factor for producing intershocks. We have seen that accelerated creep can encourage patches to rupture sooner (Figure 2.8) and that patches may never produce intershocks if the interseismic loading is not enough to overcome their high compression (filled purple triangle in Figure 2.3). Given that all of the patches in our models have significantly higher compression than the background, it is possible that observable asperity-type foreshocks on natural faults only occur for the highest creeping rates, such as the ones during earthquake nucleation.

Our results also suggest that the foreshock sequences on natural faults would be promoted by low instability ratios for asperity-type patches. Low patch instability ratios D_p/h_p^* promote isolated seismic events during the nucleation of a mainshock that do not grow into the mainshock, because lower instability ratios generally correspond to a smaller rupture extent D_r and thereby a higher isolation ratio h_m^*/D_r . Furthermore, high patch instability ratios D_p/h_p^* would require high level of heterogeneity in the fault properties to achieve the required small nucleation size h_p^* that may be less likely.

Overall, observable foreshocks likely occur in the “sweet spot” with respect to fault heterogeneity: if the heterogeneity is too mild, so that the instability ratios on patches are significantly below 1, there is no potential for microseismicity; but if the heterogeneity is too strong, then the patch-initiated events would either grow into the mainshock immediately or the patches may not rupture during the aseismic nucleation, failing during the dynamic event instead.

5.3. Discussion of future research directions and associated implications

There are many exciting avenues for continuing the work presented thus far. In the following, we outline our ideas for related future work, some of which also build off of preliminary results. Section 5.3.1 summarizes topics of future efforts related to considerations in developing further fault models with heterogeneous properties, mainly connecting to the work presented in Chapter 2. The topics in Section 5.3.2 concern deeper analysis of the mechanics of asperity-type events, primarily utilizing the results of Chapter 2-3. Finally, the ideas discussed in Section 5.3.3 expand upon the findings from the seismological analysis of Chapter 4.

5.3.1. Building heterogeneous fault models

Lack of intershocks due to overly strong patches

While the focus of the models presented in this thesis has been on those that produce intershocks, one future research direction is to revisit our observation of models that did not produce any intershocks. Of the three different scenarios for suppressing intershocks that we have seen so far: (1) overly strong patches (Section 2.3), (2) sub-seismic patches (Section 2.3), and (3) immediate triggering of the mainshock

(Section 2.6), the one of particular interest discussed here is scenario (1). In this case, the patches of higher normal stress have an instability ratio D_p/\tilde{h}_p^* greater than 1, and yet they do not rupture separately from the mainshock because they are effectively too strong to be loaded enough from the interseismic creep between mainshocks.

The idea would be to explore the minimum patch normal stress ratio σ_p/σ_m for creating overly strong patches for a given fault model, while considering variations in other properties, such as patch instability ratio (all greater than 1), patch characteristic slip distance ratio L_p/L_m , patch diameter D_p , and the number of patches in relation to the amount of the seismogenic area taken up by the patches. Factors such as the ratio of patch area to background seismogenic area, and additionally the spacing of the patches, should influence the amount of shear stress increase that each patch experiences from the loading during the interseismic period of the mainshock, and thereby affect the outcome of whether the patches produce intershocks or not, from the loading side of the consideration. Furthermore, while the fault heterogeneity in normal stress would not be observed in the form of intershock occurrence in the case of overly strong patches, maybe this heterogeneity could instead be “seen” in the form of additional complexity in the rupturing of the mainshock, for example, in the release of moment over time during the mainshock. The results of this investigation would have implications for inferring information about the fault frictional properties and heterogeneity through analysis of the mainshocks.

Nucleation size estimates in a heterogeneous environment

As discussed in Section 2.1, the nucleation size estimate that we use (Equation 2.4) was developed via a stability analysis in a homogeneous setting. While this estimate has shown to have some relevance in determining how instability-prone a given source patch is, in an order of magnitude sense (recall that we have seen patches with an

instability ratio D_p/\tilde{h}_p^* as low as 0.4 still host intershocks), it clearly does not take the heterogeneous scenario into account. Moreover, we have seen that the nucleating region of the intershocks in our models includes areas on and off of the patch (Figure 2.7). Thus, this effort would focus on updating the current nucleation size estimate that we have used so far to include consideration for the heterogeneous value of normal stress and characteristic slip distance over the nucleating region. The updated nucleation size estimate would be useful for predicting the behavior of patches in our models for future simulations, as well as for understanding the nucleation of seismic events in the field, as natural faults are inherently heterogeneous.

In developing this updated formulation for the nucleation size, it would be particularly useful to be able to measure the nucleation size directly from the results of our 3D Boundary Integral Method (BIM) simulations of asperity-type events, but the procedure for how to do so is unclear. Thus, this work could also include an exploration of ways to extract the achieved nucleation size in our simulations. As proposed in Section 2.4.2, the measurement of nucleation size could involve a weighted combination of the nucleation lengths achieved on and off of the patch, or a global length scale calculated from the entire nucleating region.

Another consideration in updating the nucleation size estimates could be the inclusion of loading rate effects. We have seen examples of the accelerated local loading from the postseismic slip of an intershock influencing the nucleation of the following intershock in the results of our simulations (e.g., Figure 2.8). In addition, the simulations of *Kaneko and Lapusta* [2008] provide an example of a stress step in loading causing the nucleation size to decrease by an order of magnitude. While there is evidence that higher loading rate corresponds to a smaller nucleation size, the exact relationship is unknown, and incorporating the impact of loading rate on nucleation size into our updated estimate would provide additional insights into the nucleation of earthquakes in realistic settings.

Seismic nucleation phase

Although detailed analysis of mainshocks is outside of the scope of our study so far, some of our preliminary analysis has shown that mainshocks from our homogeneous fault model do appear to have a roughly linear increase in moment release rate at the start of the event, which would be consistent with a self-similar rupture growth [Ellsworth and Beroza, 1995]. In contrast, preliminary results from the transition set, which includes models with significant heterogeneity and even lower background instability ratio $W_{\text{VW}}/\tilde{h}_m^*$, provide an example of more gradual moment release at the start of the event. Interestingly, this slower release can occur for both the intershocks and mainshocks, which is also consistent with the observations of the seismic nucleation phase over a wide range of magnitudes [Ellsworth and Beroza, 1995; Iio, 1995]. Furthermore, the phenomenon of delayed triggering discovered in simulations from the transition set provides the conditions for potentially causing the longest duration of the seismic nucleation phase, as discussed towards the end of Section 2.6: the high rates of background quasi-static slip as the seismic event initiates that are inherent to delayed triggering should cause the slowest moment release during the re-rupturing of the previously-slipped regions. The efforts in this future work would be directed towards gaining a better understanding of the intriguing phenomenon of seismic nucleation phase by exploring the conditions under which we see evidence of the seismic nucleation phase, its intensity, and developing a deeper physical explanation for its occurrence.

Modeling laboratory faults

The detailed understanding of the mechanics of asperity-type events presented in this thesis can be used to build models of the laboratory fault in the inspirational experiments of McLaskey and co-authors [e.g., McLaskey and Kilgore, 2013; McLaskey et al., 2014]. In particular, while the geometry of the laboratory fault is known, our

findings can inform the choice of the heterogeneous frictional properties over the fault for our numerical simulations, in an effort to match the observations of both the microseismicity and the larger-scale nucleation process of the laboratory mainshocks. The result of this investigation would not only generate information about the likely frictional properties of the laboratory fault, but would also further strengthen the understanding of earthquake nucleation and the relationship between the physical properties at the source and the inferred properties of the seismic rupture derived from remote measurements, as the laboratory set-up is arguably a scaled version of natural faults [McLaskey *et al.*, 2014]. While there is much work left to do, this effort is already underway, in collaboration with Dr. Gregory McLaksey.

One of the benefits of working with the results from the laboratory experiments is that the laboratory fault is heavily instrumented (including but not limited to slip sensors capturing the relative fault motion, piezoelectric sensors serving as lab seismometers, and strain gage pairs for deriving the local shear stress), providing a plethora of data, and many of the properties of the sample as well as the conditions that it is under during the experiments are known. This allows us the opportunity to develop models that closely match the seismic and aseismic behavior of the laboratory fault, as the number of unknowns is reduced and the variety of data imposes constraints on our models. The overall approach that we take in this work is to first approximately match the qualities of the laboratory mainshock nucleation, and then to add the circular patches that represent the asperity-type sources of microseismicity. We attempt to match both the quantitative features of the source – such as the seismic moment, stress drop, inferred patch size, and event duration – and the qualitative characteristics of their occurrence. In addition to what we have learned about the necessary separation of scales for two scales of seismicity to coexist on the same fault (Chapter 2) and the mechanics of intershocks (Chapter 3), the development of our models that represent the laboratory experiments is also informed by the results

from one of our preliminary studies (Appendix A.1), which illuminate the different effects of increasing normal stress σ_p versus decreasing characteristic slip distance L_p on the rate of intershock occurrence (Figure A.2).

As diagrammed in Figure 5 of *McLaskey and Kilgore [2013]*, the region of quasi-static slip from the nucleation process of the laboratory mainshock initiates in the center of the rectangular fault and slowly expands bilaterally, before the slip behavior transitions into dynamic rupture. This transition into the larger-scale seismic event from its nucleation typically occurs when the slip fronts from the nucleation are near the edges of the sample. In the context of our models using rate-and-state friction, this behavior likely indicates a low background instability ratio W_{VW}/h_m^* , which would explain the long duration of pre-slip and the opportunity for precursory events to be triggered within the slowly nucleating region. Interestingly, *McLaksey and co-authors* also report that the hold time (length of time that the two sides of the fault are held together in stationary contact before the increased shear loading to failure) has a significant effect on the amount of slip occurring in the slow nucleation phase and that this, in turn, affects the number of foreshocks and aftershocks observed [*McLaskey et al., 2014*]. Observations such as this provide important constraints on the properties in our models that control the interaction between the mainshock nucleation and intershocks.

In contrast to the long-term simulations in the studies presented in this thesis, which typically have 10 mainshocks, our simulations for this direction include only one larger-scale event, as the loading is reset after each mainshock in the laboratory experiments. So far, in collaboration with Dr. Gregory McLaksey, the results from our preliminary studies indicate that the laboratory scenario is best modeled by a long rectangular fault that has a free surface at the top and bottom. Currently, we are investigating different loading cases to more closely mimic the experiments. In particular, we are exploring spatial variations of normal stress and/or direct shear

stressing rates over the fault.

The experimental results reported in *McLaskey et al.* [2014] indicate that only 2-10 smaller-scale seismic events were observed per loading cycle. To match the lack of multiple intershocks occurring on the same patch in a given mainshock cycle, as well as the very small moment magnitudes, our preliminary results indicate that the best fitting parameters for the laboratory intershocks will be low instability ratios (i.e., $D_p/\tilde{h}_p^* \leq 1$). In addition, we expect that the main property contributing to the small nucleation size of the patches \tilde{h}_p^* should be the elevated normal stress σ_p , with little or no contribution from a reduced characteristic slip distance L_p , as discussed in Appendix A.2. Further efforts in this direction will involve investigating the model parameters that generate the behavior of the laboratory mainshock and precursory events in detail, with broader implications for the understanding of the seismic observations of heterogeneity on natural faults.

5.3.2. Investigating the mechanics of intershock nucleation and the resulting rupture

Event timing and relationship with nucleation

An interesting finding, discussed in Section 2.4.1, is that the mainshock recurrence time t_r for our fault models with heterogeneous normal stress can be shorter than that for the homogeneous case (e.g., Figure 2.4c.i). This result is counter-intuitive, as adding patches of higher normal stress should make the fault stronger overall, and yet it causes the fault to fail sooner on a larger scale in the form of mainshocks. Furthermore, the occurrence of intershocks also serves to relieve some of the built-up shear stress from the interseismic loading. As our work thus far has focused on the mechanics of asperity ruptures in intershocks, the work of this future direction would focus on aspects related to timing, including investigating the conditions under which

the nucleation process of the mainshock, and hence the mainshock recurrence time, is sped up or slowed down by the occurrence of intershocks.

Another question to explore as part of this future effort is whether or not the properties of intershocks depend on when they occur in relation to the mainshock. For example, we have already discovered that events with isolation ratios \tilde{h}_m^*/D_r less than 1 are able to occur early in the mainshock recurrence interval, when the stress distribution at the time the intershock initiates is thereby unfavorable for rupture growth (Section 2.5 and Figure 2.10). For the same reasons that isolation ratio is affected, the relative rupture extent D_r/D_p for an intershock in a given fault model should also depend on the relative timing within the mainshock recurrence interval. For example, we expect that intershocks occurring in the latter half of the interseismic period of the mainshocks should have a larger rupture extent, as the conditions would be more favorable for rupture growth because much of the fault has already pre-slipped from the protracted nucleation of the mainshock. The approach for investigating this question could be to analyze the rupture extents for groups of intershocks that fall into bins of the latter half and quarter of the mainshock recurrence interval (i.e., $[t_r/2, t_r]$ and $[t_r/4, t_r]$) and compare the rupture extents to those from the first half ($[0, t_r/2]$). In the same vein, we could also compare the average number of intershocks per mainshock cycle to the average isolation ratio. The motivation for this analysis is to further explore the separation of scales corresponding to faults that experience many intershocks per cycle (and consequently have the most foreshock-like events with respect to their timing), which thereby have the most potential forecasting power due to the plethora of precursory signals.

Yet another topic to consider within this topic of future work is the interaction between intershocks. Over the progression of a given interseismic period of the mainshock, intershocks can occur and the extent of their interaction may increase as the extent of the pre-slipped region of the seismogenic zone increases, allowing for easier

communication between intershocks in the form of post-seismic slip (e.g., Figure 2.8 and Figure A.3). In addition, the interaction between intershocks is influenced by the spacing between the patches of higher normal stress. The investigation in this part of the effort would also relate to the consideration of loading effects in the topic proposed in Section 5.3.1.

Variation in the parameters used in the simplified stress drop calculation

The simplified stress drop calculation that we derive in Section 3.4 has been successful in explaining the main features in the dependence of stress drop on patch normal stress ratio. This formulation (e.g., Equation 3.5) relies on values of three parameters (Equation 3.3) – γ , which relates the relative rupture extent to the normal stress ratio; ν_p , which relates the shear stress change on the patch to the patch normal stress; and ν_m , which similarly relates the shear stress change in the ruptured area outside of the patch to the background normal stress – and these parameters have been treated as constants, so far. However, we suspect that γ , ν_p , and ν_m are dependent on the rate-and-state parameters a and b . Moreover, we have uncovered evidence that these parameters are also dependent on the patch instability ratio D_p/\tilde{h}_p^* , with the values of all three being higher for higher D_p/\tilde{h}_p^* (e.g., blue symbols in Figure 3.4a, Figure 3.8a, and Figure 3.9). In this effort, we would further investigate these dependencies, which have consequences for understanding the stress changes over the ruptured area in heterogeneous environments. Furthermore, it would be particularly useful to explore ways to derive values of these parameters based directly on frictional properties of the fault, such as a , b , background normal stress σ_m , normal stress ratio σ_p/σ_m , and shear modulus μ , in contrast to estimating the values from least-squares fitting to the simulation results. In addition, this improved understanding of the mechanics of intershock ruptures can also be utilized to better translate the value of stress drop into information about the fault properties and conditions at the source.

Predictive value of intershocks

The idea of this future direction is to further explore the possibility of identifying the differences between precursory events that are actually leading to the upcoming mainshock (foreshocks) and those that are not (background seismicity), thereby assessing the conditions under which intershocks have predictive value. To do so, we would create heterogeneous fault models that have a more realistic geometry, which would include many patches that have relatively low instability ratios, contributing to maintaining a sufficient separation in length scales. In addition, we could vary the spacing between the patches (and hence the quantity of patches) in a grid-like placement, or even increase the complexity of the model further by having a heterogeneous non-grid-like patch placement, or assigning a variety of properties to the patches within the same fault (i.e., the patch properties such as instability ratio D_p/\tilde{h}_p^* , etc. would no longer be identical). Another variable to explore is the effect of loading rate on the resulting behavior. Consequently, the efforts in this work would rely on what we have learned from our simulations so far about the mechanics of intershocks to choose the model properties carefully, as these larger models will be much more computationally expensive. The results of this investigation would have direct implications for the potential of earthquake forecasting, which also relates closely with all three sub-topics of the avenue proposed in Section 5.3.2: (1) the effect of intershocks on the recurrence interval of the mainshocks, (2) how the properties of the intershocks depend on their timing relative to the mainshock, and (3) the interaction between intershocks.

5.3.3. Exploring seismological interpretations and characteristic features of asperity-type events

Physical explanations of trends in seismological features

The potentially characteristic seismological properties of asperity-type events, presented in Section 4.6, provide some hope that foreshocks, or at least asperity-type events, could be identified as such, immediately after the seismograms are recorded and processed. As part of the effort to determine whether or not these seismological features are reliably characteristic, an interesting topic for future work would be to investigate the physical reasons behind why the qualities of these heterogeneous sources manifest seismologically as high fall-off rate n and low p-to-s corner frequency ratio f_c^p/f_c^s – for example, what is it about the heterogeneity in normal stress over the ruptured area that generates the higher fall-off rates and, in tandem, why does it not instead correspond with typical or low n ? The illumination of the physical connection between the observable seismological features and the behavior of the source, as a result of this work, would have direct implications for seismology, specifically concerning the appropriate interpretation of source properties from seismograms.

Detectability of seismological features

As the seismological analysis conducted in Chapter 4 was for a focal sphere of stations in a homogeneous elastic whole-space, an interesting avenue of future work is to consider the detectability of the proposed possibly characteristic seismological features (Section 4.6) under more realistic observational conditions. Furthermore, these features – high n and low f_c^p/f_c^s – may not arise for every station location, even under ideal conditions. The work of this future direction would explore the effect of additional complications caused by material effects, practical limitations, and methodological choices.

A natural first step to this investigation would be to use a dissipative medium as the bulk material. For example, representing the effects of attenuation by convolving the source with a Futterman function [*Futterman, 1962; Lin et al., 2016*] with successively stronger attenuation (via successively lower quality factor Q) would result in seemingly higher fall-off rate and possibly an apparent shift in the calculated corner frequency towards lower frequencies. Given that seismologists who are analyzing real seismograms are tasked with correcting for the effect of attenuation before fitting the spectra, some may interpret the original high decay in spectral amplitude after the corner in their data as being completely due to intense attenuation and falsely over-correct for it, not realizing that some of the contribution to the faster decay may actually be coming from the fall-off rate n of the source. Thus, not only do the effects of more realistic material properties influence the spectra of the seismograms and therefore the calculation of source properties from their spectral shape, but the methodological choices in analyzing the spectra also affect the calculated properties.

Additional complications are provided by signal quality (e.g., signal-to-noise ratio) and observational perspective. In a realistic scenario, instead of having a full sphere of stations around the source, the set of available stations would span a limited range of angles θ and ϕ , effectively sampling a portion of the focal sphere. Furthermore, for a fixed set of stations, the specific part of the focal sphere that is being sampled depends on the orientation of the fault. If the source ruptures asymmetrically, then there is additional bias in the spectra from the effect of directivity. Calculation of the spectral parameters, such as the corner frequency, can be biased even further by having a limited number of stations.

To approach these practical limitations, in this future effort, we could restrict our analysis to a set of neighboring stations on the focal sphere, representing the limited coverage of a typical set of surface stations for a given fault orientation. As the locations of stations on our focal spheres are grid-like with respect to angle, we could

also explore the bias produced by choosing a randomly chosen subset of stations within this group to simulate uneven coverage. While investigation of the limitations inherent to seismological observations on natural faults is complex, the results would have implications for correctly identifying source qualities and, hence, could shed some light on appropriate methods for the potential of physics-based forecasting of upcoming mainshocks through near-real-time identification of foreshocks.

A. Appendices

A.1. Model parameters and geometry for the preliminary set

The preliminary study explained here consists of nine fault models (Table A.1): one case with a homogeneous seismogenic zone, and eight cases with 25 circular patches of higher normal stress σ_{main} and/or lower characteristic slip distance L_{patch} . Compared to the main set (Section 2.3), all models in the preliminary set (e.g., figure A.1) are three times as large with respect to the overall spatial dimension, but have the same rate-and-state parameters a , b , and L_m as the main set. Additional differences in the parameters are that the background normal stress σ_m is 5 MPa (instead of 10 MPa), creating a background nucleation size \tilde{h}_m^* of 1 m to match the inferred larger-scale nucleation size from the laboratory experiments of *McLaskey and Kilgore [2013]* and, hence, provides a higher background instability ratio W_{VW}/\tilde{h}_m^* of 3 (instead of 2). The final difference is that the plate-style loading rate for the preliminary set is 1×10^{-9} m/s, which is lower than the rate of 4×10^{-8} m/s from the main set.

The models in group A were developed to investigate patches that are expected to be capable of hosting smaller-scale events (intershocks) because they have $D_p/\tilde{h}_p^* > 1$, while models in group B explore the possibility of getting intershocks despite the estimated patch instability ratio D_p/\tilde{h}_p^* being smaller than 1. The models in group C further investigate just how small the patches can be and still produce intershocks

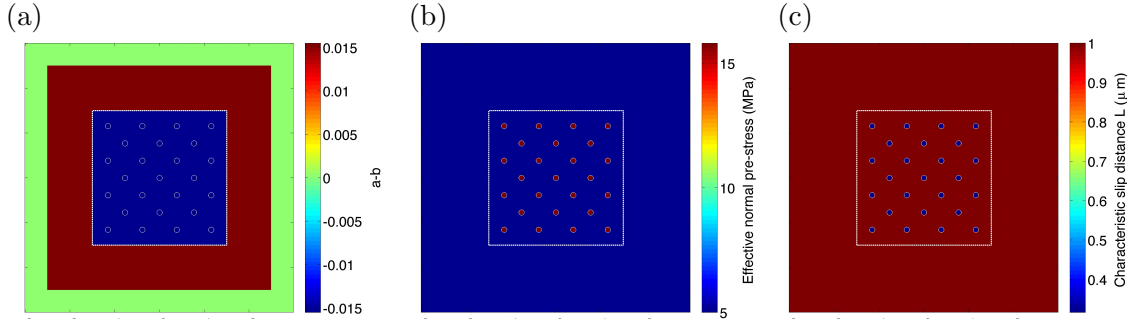


Figure A.1.: Spatial distribution of fault properties for model A.3. A white square outlines the velocity-weakening region and white circles outline the location of heterogeneous patches. **(a)** DR rate-and-state parameter $a - b$. **(b)** Effective normal stress σ . **(c)** Characteristic slip distance L . In this model, the heterogeneous patches are created by a combination of both elevated normal stress σ_p and reduced L_p .

(Table A.1). Although inverse proportions of L and σ result in identical estimates of nucleation size \tilde{h}^* , we anticipate that the corresponding simulations would produce different slip behaviors because decreases in L do not change the overall level of the frictional strength of the patch while increases in σ do.

A.2. Results concerning intershock behavior for the preliminary set

The differences in seismicity between the various models (Table A.1) can be seen by plotting the maximum slip velocity V over the fault as a function of time, shown in Figure A.2. The log scale on the y-axis helps to emphasize the wide range of slip rates that the fault experiences as it progresses from interseismic to seismic slip. Time on the x-axis is normalized by the average interseismic period of the homogeneous model A.0, analogous to Figure 2.4.

The slip rate plots (Figure A.2) for models in group A show that just decreasing L_p on patches with $D_p/\tilde{h}_p^* > 1$ (model A.1) results in many intershock event attempts, as expected, with some of which reaching seismic speeds right before the main event

Table A.1.: Model parameters for the preliminary set. The first two rows correspond to the model with a homogeneous seismogenic region. For the heterogeneous fault models, the second through sixth columns display properties of the 25 circular patches: characteristic slip distance ratio L_p/L_m ; normal stress ratio σ_p/σ_m ; patch instability ratio D_p/\tilde{h}_p^* ; ratio of the background nucleation size to the nucleation size on the patch $\tilde{h}_m^*/\tilde{h}_p^*$ (also called separation ratio); and the diameter of the patch D_p . The values shown in the last column are the average number (rounded to the nearest integer) of intershocks occurring per recurrence interval of the mainshock, N_{avg} .

Model	L_m	σ_m	W_{vw}	\tilde{h}_m^*	a	b
A.0	$1 \mu m$	5 MPa	$3 m$	$1 m$	0.01	0.0255
Model	L_p/L_m	σ_p/σ_m	D_p/\tilde{h}_p^*	$\tilde{h}_m^*/\tilde{h}_p^*$	D_p [cm]	N_{avg}
A.1	1/10	1	1.2	10	12	3
A.2	$1/\sqrt{10}$	$\sqrt{10}$	1.2	10	12	21
A.3	1	10	1.2	10	12	3
B.1	1/10	1	0.8	10	8	0
B.2	$1/\sqrt{10}$	$\sqrt{10}$	0.8	10	8	4
B.3	1	10	0.8	10	8	4
C.1	1	10	0.5	10	5	2
C.2	1/2	10	0.8	20	4	8

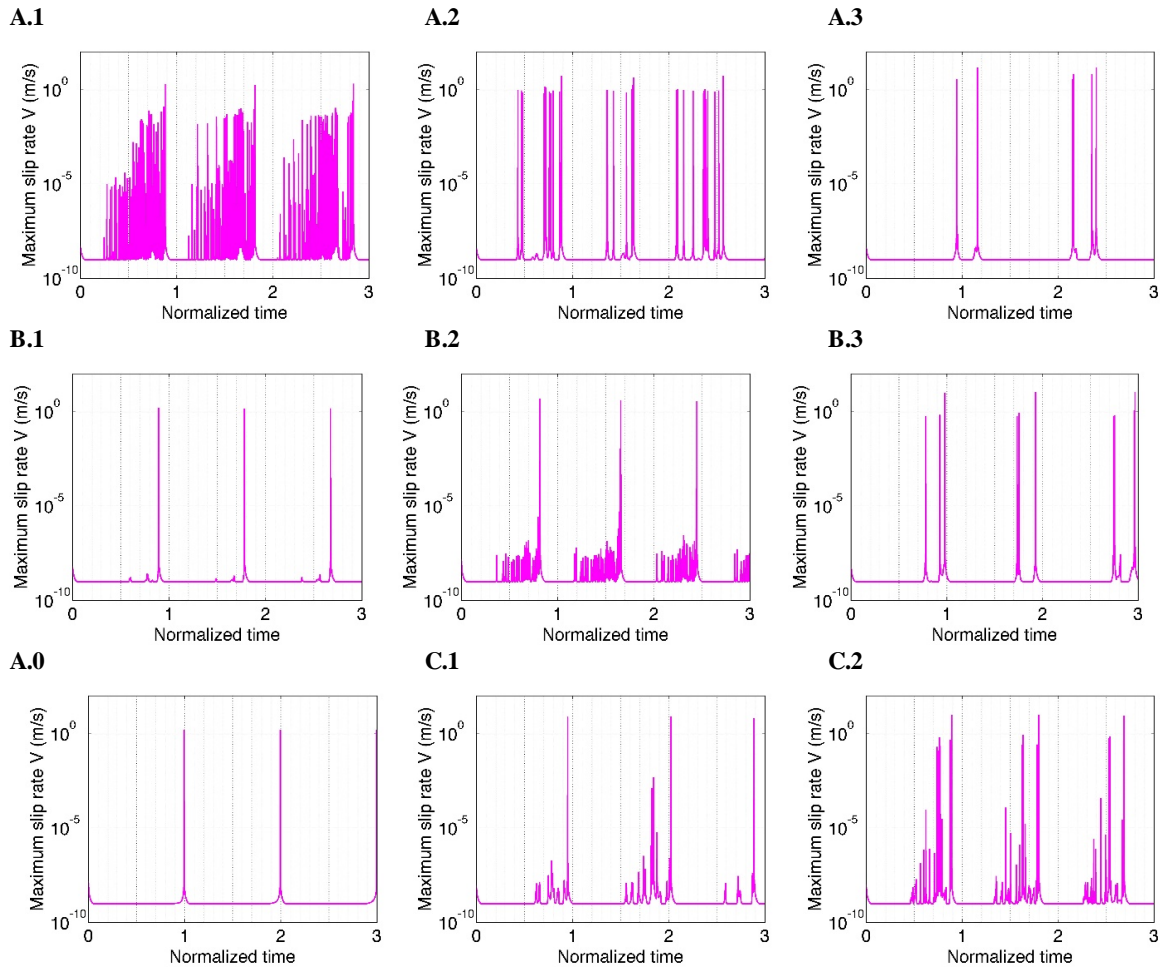


Figure A.2.: Maximum slip velocity as a function of time for each model in the preliminary set. Flat sections correspond to the loading velocity of 10^{-9} m/s and the largest velocity spikes (on the order of 10^2 m/s) correspond to the rupture of the entire seismogenic region in a mainshock. The remaining spikes correspond to accelerated slip on patches, with some of them being fast enough (faster than 10^{-1} m/s) to qualify as seismic events. These plots show that it is indeed possible to obtain seismicity on a smaller scale within the larger-scale nucleation process for realistic values of frictional parameters and that changing the properties of the patches results in different intershock patterns.

(foreshocks). Combining a decrease in L_p with an increase in σ_p while keeping the nucleation size constant results in a reduced number of attempts, but with almost all of them being seismic (model A.2). Only increasing σ_p (model A.3) results in even fewer intershock attempts, but all of which are seismic. This trend makes sense because decreasing L_p essentially only reduces the nucleation size locally, making it easier to nucleate there. On the other hand, while increasing σ_p not only decreases \tilde{h}_p^* but also increases the strength of these patches, which requires higher shear stresses for them to start slipping and produces larger local shear stress changes when they do slip, reducing the number of slip attempts. As expected, the case of changing both parameters falls in between these two models.

The models in group B correspond to patches with $D_p/\tilde{h}_p^* < 1$, which predicts these patches should not be able to host smaller-scale seismic events. The simulation of model B.1 shows that this is indeed the case for only decreasing L_p . Increasing σ_p along with decreasing L_p causes more noticeable nucleation attempts, but most of these are far from seismic (model B.2). Increasing σ_p alone in this regime (model B.3) actually results in less frequent but higher shear stress change intershocks like in the partner case for $D_p/\tilde{h}_p^* > 1$ (model A.3). The models in group B as a whole show that smaller-scale seismic events can occur on patches that are smaller than the estimated nucleation size when the local compression is increased.

In the experiments of McLaskey and co-authors, there is no notable recurrence of smaller-scale events at the same asperity locations during an individual larger-scale nucleation period. Using this observation together with the results of our simulations leads us to conclude that the experimentally observed foreshocks occur on patches that likely have significantly higher normal stress and potentially also slightly smaller characteristic slip distance than the rest of the fault. This combination of relative proportions of σ_p and L_p corresponds to observing a few smaller-scale events per each recurrence period of the mainshock that reach seismic slip rates while also occurring on

patches with estimated patch instability ratios D_p/\tilde{h}_p^* just below 1. The simulation from the preliminary set with intershock behavior that most closely matches the laboratory experiments is model C.2.

As discussed in reference to Figure A.2, the majority of the models in the preliminary set produce smaller-scale seismic events within the protracted nucleation of the larger-scale event. To further illustrate how these intershocks occur, a series of snapshots of the spatial slip velocity distribution in the velocity-weakening region of the fault from model A.2 is shown in Figure A.3. In particular, the snapshots in Figure A.3 provide an example of intershocks clustering before the mainshock, as they interact with each other via postseismic slip. Whether these smaller-scale seismic events and their postseismic slip substantially influence the larger-scale nucleation process itself is an important question of future work.

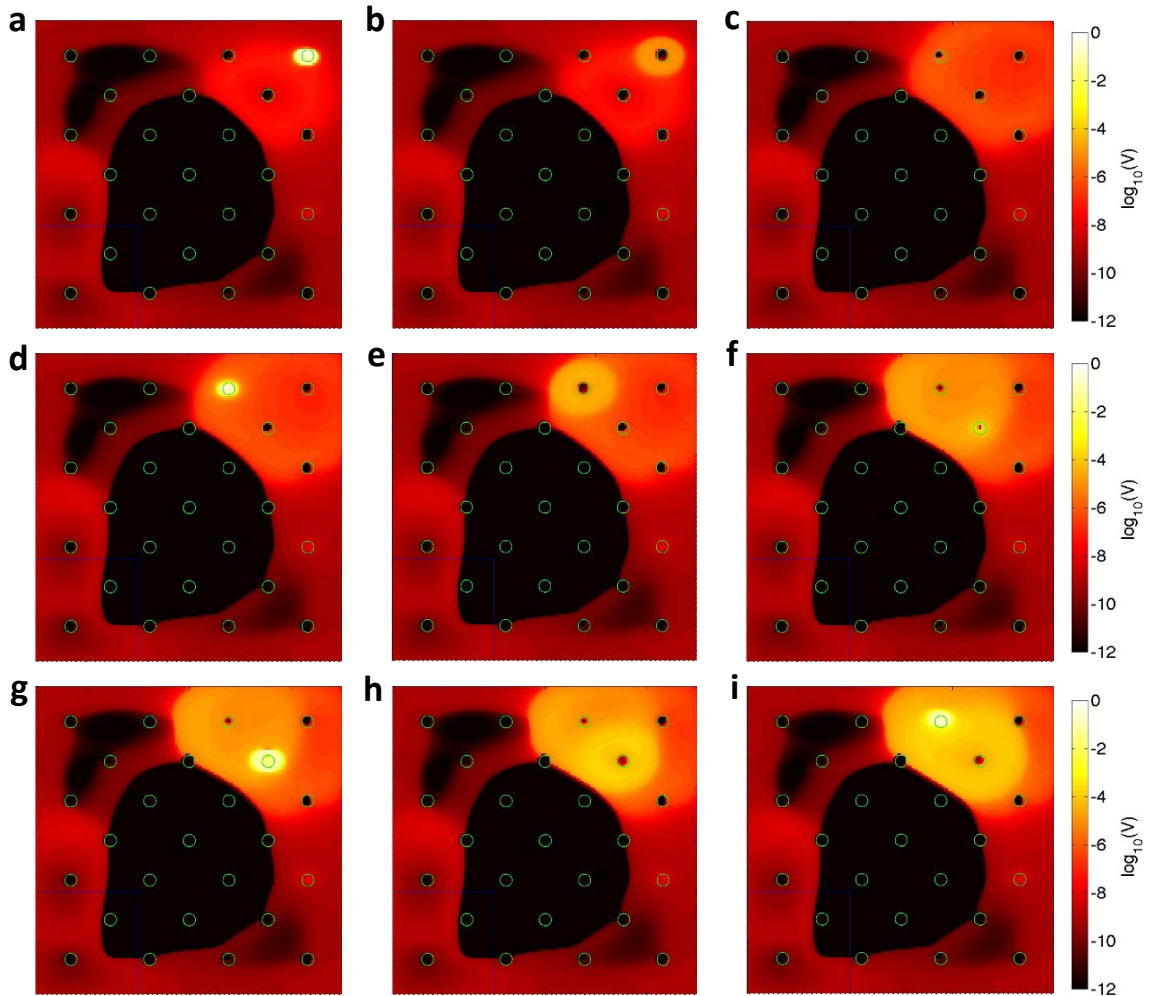


Figure A.3.: Snapshots of the spatial slip velocity distribution over the seismogenic region of the fault for model A.2. Green circles correspond to the patches of higher σ_p and lower L_p . Bright yellow corresponds to seismic slip rates, orange and red correspond to accelerated aseismic slip, dark red corresponds to creep at the plate rate, and black indicates regions that are effectively locked. The panels capture the larger-scale nucleation process, which occurs along the boundaries of the fault while the middle remains locked (due to the background instability ratio $W_{VW}/\tilde{h}_m^* = 3$), as well as a sequence of intershocks occurring over the area where the mainshock finally nucleates. **(a)** An intershock occurring at one of the patches. **(b)-(c)** The postseismic slip from this event, which is added onto the existing nucleation creep and affects the location of the subsequent intershocks. **(d)-(i)** Intershocks continue to occur and to influence each other through their postseismic slip. The smaller-scale seismic event in **(i)** is the last intershock before the mainshock initiates.

Bibliography

Abercrombie, R. E., Earthquake source scaling relationships from -1 to 5 M_L using seismograms recorded at 2.5-km depth, *Journal of Geophysical Research: Solid Earth*, 100(B12), 24,015–24,036, doi:10.1029/95JB02397, 1995.

Abercrombie, R. E., and J. Mori, Occurrence patterns of foreshocks to large earthquakes in the western United States, *Nature*, 381(6580), 303–307, doi:10.1038/381303a0, 1996.

Aki, K., Generation and propagation of G waves from the Niigata Earthquake of June 16, 1964. Part 2. Estimation of earthquake movement, released energy, and stress-strain drop from the G wave spectrum, *Bulletin of the Earthquake Research Institute*, 44, 73–88, 1966.

Aki, K., and P. G. Richards, *Quantitative Seismology*, 2 ed., University Science Books, 2002.

Allmann, B. P., and P. M. Shearer, Spatial and temporal stress drop variations in small earthquakes near Parkfield, California, *Journal of Geophysical Research: Solid Earth*, 112(B4), doi:10.1029/2006JB004395, 2007.

Baltay, A., S. Ide, G. Prieto, and G. Beroza, Variability in earthquake stress drop and apparent stress, *Geophysical Research Letters*, 38(6), doi:10.1029/2011GL046698, 2011.

- Bouchon, M., H. Karabulut, M. Aktar, S. Özalaybey, J. Schmittbuhl, and M.-P. Bouin, Extended nucleation of the 1999 M_w 7.6 Izmit earthquake, *science*, *331*(6019), 877–880, doi:10.1126/science.1197341, 2011.
- Bouchon, M., V. Durand, D. Marsan, H. Karabulut, and J. Schmittbuhl, The long precursory phase of most large interplate earthquakes, *Nature Geoscience*, *6*(4), 299, doi:10.1038/ngeo1770, 2013.
- Bowman, D. D., and G. C. King, Accelerating seismicity and stress accumulation before large earthquakes, *Geophysical Research Letters*, *28*(21), 4039–4042, doi:10.1029/2001GL013022, 2001.
- Brodsky, E. E., and T. Lay, Recognizing foreshocks from the 1 April 2014 Chile earthquake, *Science*, *344*(6185), 700–702, doi:10.1126/science.1255202, 2014.
- Brune, J. N., Tectonic stress and the spectra of seismic shear waves from earthquakes, *Journal of Geophysical Research*, *75*(26), 4997–5009, doi:10.1029/JB075i026p04997, 1970.
- Chen, T., and N. Lapusta, Scaling of small repeating earthquakes explained by interaction of seismic and aseismic slip in a rate and state fault model, *Journal of Geophysical Research: Solid Earth*, *114*(B1), doi:10.1029/2008JB005749, 2009.
- Day, S. M., L. A. Dalguer, N. Lapusta, and Y. Liu, Comparison of finite difference and boundary integral solutions to three-dimensional spontaneous rupture, *Journal of Geophysical Research: Solid Earth*, *110*(B12), doi:10.1029/2005JB003813, 2005.
- De Martin, F., H. Kawase, and A. Modaressi-Farahmand Razavi, Nonlinear soil response of a borehole station based on one-dimensional inversion during the 2005 Fukuoka prefecture western offshore earthquake, *Bulletin of the Seismological Society of America*, *100*(1), 151–171, doi:10.1785/0120090125, 2010.

- Denolle, M. A., and P. M. Shearer, New perspectives on self-similarity for shallow thrust earthquakes, *Journal of Geophysical Research: Solid Earth*, 121(9), 6533–6565, doi:10.1002/2016JB013105, 2016.
- Dieterich, J. H., Modeling of rock friction: 1. Experimental results and constitutive equations, *Journal of Geophysical Research: Solid Earth*, 84(B5), 2161–2168, doi:10.1029/JB084iB05p02161, 1979.
- Dieterich, J. H., Earthquake nucleation on faults with rate-and state-dependent strength, *Tectonophysics*, 211(1-4), 115–134, doi:10.1016/0040-1951(92)90055-B, 1992.
- Dieterich, J. H., Applications of rate-and state-dependent friction to models of fault slip and earthquake occurrence, *Treatise on Geophysics*, 4, 107–129, doi:10.1016/B978-044452748-6/00065-1, 2007.
- Dieterich, J. H., and B. Kilgore, Implications of fault constitutive properties for earthquake prediction, *Proceedings of the National Academy of Sciences*, 93(9), 3787–3794, doi:10.1073/pnas.93.9.3787, 1996.
- Dodge, D. A., G. C. Beroza, and W. L. Ellsworth, Foreshock sequence of the 1992 Landers, California, earthquake and its implications for earthquake nucleation, *Journal of Geophysical Research: Solid Earth*, 100(B6), 9865–9880, doi:10.1029/95JB00871, 1995.
- Dodge, D. A., G. C. Beroza, and W. Ellsworth, Detailed observations of California foreshock sequences: Implications for the earthquake initiation process, *Journal of Geophysical Research: Solid Earth*, 101(B10), 22,371–22,392, doi:10.1029/96JB02269, 1996.
- Doser, D. I., Foreshocks and aftershocks of large ($M \geq 5.5$) earthquakes within the

- Western Cordillera of the United States, *Bulletin of the Seismological Society of America*, *80*(1), 110–128, 1990.
- Dragert, H., K. Wang, and T. S. James, A silent slip event on the deeper cascadia subduction interface, *Science*, *292*(5521), 1525–1528, doi:10.1126/science.1060152, 2001.
- Ellsworth, W. L., and G. C. Beroza, Seismic evidence for an earthquake nucleation phase, *Science*, *268*, 851–851, doi:10.1126/science.268.5212.851, 1995.
- Eshelby, J. D., The determination of the elastic field of an ellipsoidal inclusion, and related problems, in *Proceedings of the Royal Society of London, Series A*, vol. 241, pp. 376–396, The Royal Society, doi:10.1098/rspa.1957.0133, 1957.
- Freund, L. B., *Dynamic fracture mechanics*, Cambridge University Press, 1990.
- Futterman, W. I., Dispersive body waves, *Journal of Geophysical Research*, *67*(13), 5279–5291, doi:10.1029/JZ067i013p05279, 1962.
- Hardebeck, J. L., and A. Aron, Earthquake stress drops and inferred fault strength on the Hayward fault, east San Francisco Bay, California, *Bulletin of the Seismological Society of America*, *99*(3), 1801–1814, doi:10.1785/0120080242, 2009.
- Haskell, N., Total energy and energy spectral density of elastic wave radiation from propagating faults, *Bulletin of the Seismological Society of America*, *54*(6A), 1811–1841, 1964.
- Heaton, T. H., Evidence for and implications of self-healing pulses of slip in earthquake rupture, *Physics of the Earth and Planetary Interiors*, *64*(1), 1–20, doi:10.1016/0031-9201(90)90002-F, 1990.
- Higgins, N., and N. Lapusta, Exploring models of foreshock sources using rate-and-state friction, in *Contributions to the Foundations of Multidisciplinary Research in*

- Mechanics*, vol. 3, edited by J. M. Floryan, pp. 2148–2149, International Union of Theoretical and Applied Mechanics, 2017.
- Ide, S., and G. C. Beroza, Does apparent stress vary with earthquake size?, *Geophysical Research Letters*, 28(17), 3349–3352, doi:10.1029/2001GL013106, 2001.
- Ide, S., G. C. Beroza, S. G. Prejean, and W. L. Ellsworth, Apparent break in earthquake scaling due to path and site effects on deep borehole recordings, *Journal of Geophysical Research: Solid Earth*, 108(B5), doi:10.1029/2001JB001617, 2003.
- Iio, Y., Observations of the slow initial phase generated by microearthquakes: Implications for earthquake nucleation and propagation, *Journal of Geophysical Research: Solid Earth*, 100(B8), 15,333–15,349, doi:10.1029/95JB01150, 1995.
- Jiang, J., and N. Lapusta, Connecting depth limits of interseismic locking, microseismicity, and large earthquakes in models of long-term fault slip, *Journal of Geophysical Research: Solid Earth*, 122, doi:10.1002/2017JB014030, 2017.
- Jones, L., and P. Molnar, Frequency of foreshocks, *Nature*, 262(5570), 677–679, doi:10.1038/262677a0, 1976.
- Jones, L. M., and P. Molnar, Some characteristics of foreshocks and their possible relationship to earthquake prediction and premonitory slip on faults, *Journal of Geophysical Research: Solid Earth*, 84(B7), 3596–3608, doi:10.1029/JB084iB07p03596, 1979.
- Kanamori, H., The energy release in great earthquakes, *Journal of Geophysical Research*, 82(20), 2981–2987, doi:10.1029/JB082i020p02981, 1977.
- Kanamori, H., and D. L. Anderson, Theoretical basis of some empirical relations in seismology, *Bulletin of the Seismological Society of America*, 65(5), 1073–1095, 1975.

- Kanamori, H., and G. S. Stewart, Seismological aspects of the Guatemala earthquake of February 4, 1976, *Journal of Geophysical Research: Solid Earth*, 83(B7), 3427–3434, doi:10.1029/JB083iB07p03427, 1978.
- Kaneko, Y., and N. Lapusta, Variability of earthquake nucleation in continuum models of rate-and-state faults and implications for aftershock rates, *Journal of Geophysical Research: Solid Earth*, 113(B12), doi:10.1029/2007JB005154, 2008.
- Kaneko, Y., and P. M. Shearer, Seismic source spectra and estimated stress drop derived from cohesive-zone models of circular subshear rupture, *Geophysical Journal International*, 197(2), 1002–1015, doi:10.1093/gji/ggu030, 2014.
- Kaneko, Y., and P. M. Shearer, Variability of seismic source spectra, estimated stress drop, and radiated energy, derived from cohesive-zone models of symmetrical and asymmetrical circular and elliptical ruptures, *Journal of Geophysical Research: Solid Earth*, 120(2), 1053–1079, doi:10.1002/2014JB011642, 2015.
- Kaneko, Y., J.-P. Avouac, and N. Lapusta, Towards inferring earthquake patterns from geodetic observations of interseismic coupling, *Nature Geoscience*, 3(5), 363, doi:10.1038/ngeo843, 2010.
- Kaneko, Y., S. B. Nielsen, and B. M. Carpenter, The onset of laboratory earthquakes explained by nucleating rupture on a rate-and-state fault, *Journal of Geophysical Research: Solid Earth*, 121(8), 6071–6091, doi:10.1002/2016JB013143, 2016.
- Kato, A., K. Obara, T. Igarashi, H. Tsuruoka, S. Nakagawa, and N. Hirata, Propagation of slow slip leading up to the 2011 M_w 9.0 Tohoku-Oki earthquake, *Science*, 335(6069), 705–708, doi:10.1126/science.1215141, 2012.
- Kostrov, B., Self-similar problems of propagation of shear cracks, *Journal of Applied Mathematics and Mechanics*, 28(5), 1077–1087, doi:10.1016/0021-8928(64)90010-3, 1964.

- Kwiatek, G., K. Plenkers, G. Dresen, and J. R. Group, Source parameters of picoseismicity recorded at Mponeng deep gold mine, South Africa: Implications for scaling relations, *Bulletin of the Seismological Society of America*, 101(6), 2592–2608, doi:10.1785/0120110094, 2011.
- Lapusta, N., and S. Barbot, Models of earthquakes and aseismic slip based on laboratory-derived rate-and-state friction laws, in *The Mechanics of Faulting: From Laboratory to Real Earthquakes*, edited by A. Bizzarri and H. S. Bhat, pp. 153–207, Research Signpost, 2012.
- Lapusta, N., and Y. Liu, Three-dimensional boundary integral modeling of spontaneous earthquake sequences and aseismic slip, *Journal of Geophysical Research: Solid Earth*, 114(B9), doi:10.1029/2008JB005934, 2009.
- Lapusta, N., J. R. Rice, Y. Ben-Zion, and G. Zheng, Elastodynamic analysis for slow tectonic loading with spontaneous rupture episodes on faults with rate-and state-dependent friction, *Journal of Geophysical Research: Solid Earth*, 105(B10), 23,765–23,789, doi:10.1029/2000JB900250, 2000.
- Lengliné, O., J. Elkhoury, G. Daniel, J. Schmittbuhl, R. Toussaint, J.-P. Ampuero, and M. Bouchon, Interplay of seismic and aseismic deformations during earthquake swarms: An experimental approach, *Earth and Planetary Science Letters*, 331, 215–223, doi:10.1016/j.epsl.2012.03.022, 2012.
- Lin, Y.-Y., K.-F. Ma, and V. Oye, Observation and scaling of microearthquakes from the Taiwan Chelungpu-fault borehole seismometers, *Geophysical Journal International*, 190(1), 665–676, doi:10.1111/j.1365-246X.2012.05513.x, 2012.
- Lin, Y.-Y., K.-F. Ma, H. Kanamori, T.-R. A. Song, N. Lapusta, and V. C. Tsai, Evidence for non-self-similarity of microearthquakes recorded at a Taiwan bore-

- hole seismometer array, *Geophysical Journal International*, 206(2), 757–773, doi:10.1093/gji/ggw172, 2016.
- Liu, Y., and J. R. Rice, Spontaneous and triggered aseismic deformation transients in a subduction fault model, *Journal of Geophysical Research: Solid Earth*, 112(B9), doi:10.1029/2007JB004930, 2007.
- Liu, Y., J. R. Rice, and K. M. Larson, Seismicity variations associated with aseismic transients in Guerrero, Mexico, 1995–2006, *Earth and Planetary Science Letters*, 262(3-4), 493–504, doi:10.1016/j.epsl.2007.08.018, 2007.
- Lohman, R. B., and J. J. McGuire, Earthquake swarms driven by aseismic creep in the Salton Trough, California, *Journal of Geophysical Research: Solid Earth*, 112(B4), doi:10.1029/2006JB004596, 2007.
- Lui, S. K., and N. Lapusta, Repeating microearthquake sequences interact predominantly through postseismic slip, *Nature Communications*, 7, 13,020, doi:10.1038/ncomms13020, 2016.
- Madariaga, R., Dynamics of an expanding circular fault, *Bulletin of the Seismological Society of America*, 66(3), 639–666, 1976.
- Madariaga, R., On the relation between seismic moment and stress drop in the presence of stress and strength heterogeneity, *Journal of Geophysical Research: Solid Earth*, 84(B5), 2243–2250, doi:10.1029/JB084iB05p02243, 1979.
- Maeda, K., Time distribution of immediate foreshocks obtained by a stacking method, *Pure and Applied Geophysics*, 155(2-4), 381–394, 1999.
- Marone, C., Laboratory-derived friction laws and their application to seismic faulting, *Annual Review of Earth and Planetary Sciences*, 26(1), 643–696, doi:10.1146/annurev.earth.26.1.643, 1998.

- Marquardt, D. W., An algorithm for least-squares estimation of nonlinear parameters, *Journal of the Society for Industrial and Applied Mathematics*, 11(2), 431–441, doi:10.1137/0111030, 1963.
- McGuire, J. J., M. S. Boettcher, and T. H. Jordan, Foreshock sequences and short-term earthquake predictability on East Pacific Rise transform faults, *Nature*, 434(7032), 457, doi:10.1038/nature03377, 2005.
- McLaskey, G. C., and B. D. Kilgore, Foreshocks during the nucleation of stick-slip instability, *Journal of Geophysical Research: Solid Earth*, 118(6), 2982–2997, doi:10.1002/jgrb.50232, 2013.
- McLaskey, G. C., B. D. Kilgore, D. A. Lockner, and N. M. Beeler, Laboratory generated $M - 6$ earthquakes, *Pure and Applied Geophysics*, 171(10), 2601–2615, doi:10.1007/s00024-013-0772-9, 2014.
- Meier, M.-A., T. Heaton, and J. Clinton, Evidence for universal earthquake rupture initiation behavior, *Geophysical Research Letters*, 43(15), 7991–7996, doi:10.1002/2016GL070081, 2016.
- Molnar, P., B. E. Tucker, and J. N. Brune, Corner frequencies of P and S waves and models of earthquake sources, *Bulletin of the Seismological Society of America*, 63(6-1), 2091–2104, 1973.
- Noda, H., and N. Lapusta, Stable creeping fault segments can become destructive as a result of dynamic weakening, *Nature*, 493(7433), 518, doi:10.1038/nature11703, 2013.
- Noda, H., E. M. Dunham, and J. R. Rice, Earthquake ruptures with thermal weakening and the operation of major faults at low overall stress levels, *Journal of Geophysical Research: Solid Earth*, 114(B7), doi:10.1029/2008JB006143, 2009.

- Noda, H., N. Lapusta, and H. Kanamori, Comparison of average stress drop measures for ruptures with heterogeneous stress change and implications for earthquake physics, *Geophysical Journal International*, 193(3), 1691–1712, doi:10.1093/gji/ggt074, 2013.
- Peng, Z., and J. Gomberg, An integrated perspective of the continuum between earthquakes and slow-slip phenomena, *Nature Geoscience*, 3(9), 599, doi:10.1038/ngeo940, 2010.
- Perfettini, H., and J.-P. Avouac, Postseismic relaxation driven by brittle creep: A possible mechanism to reconcile geodetic measurements and the decay rate of aftershocks, application to the Chi-Chi earthquake, Taiwan, *Journal of Geophysical Research: Solid Earth*, 109(B2), doi:10.1029/2003JB002488, 2004.
- Perfettini, H., and J.-P. Avouac, Modeling afterslip and aftershocks following the 1992 Landers earthquake, *Journal of Geophysical Research: Solid Earth*, 112(B7), doi:10.1029/2006JB004399, 2007.
- Reasenber, P. A., Foreshock occurrence before large earthquakes, *Journal of Geophysical Research: Solid Earth*, 104(B3), 4755–4768, doi:10.1029/1998JB900089, 1999.
- Rice, J., and A. L. Ruina, Stability of steady frictional slipping, *Journal of Applied Mechanics*, 50(2), 343–349, doi:10.1115/1.3167042, 1983.
- Rice, J. R., Fault stress states, pore pressure distributions, and the weakness of the San Andreas fault, in *International Geophysics*, vol. 51, pp. 475–503, Elsevier, doi:10.1016/S0074-6142(08)62835-1, 1992.
- Rice, J. R., Spatio-temporal complexity of slip on a fault, *Journal of Geophysical Research: Solid Earth*, 98(B6), 9885–9907, doi:10.1029/93JB00191, 1993.

- Rice, J. R., N. Lapusta, and K. Ranjith, Rate and state dependent friction and the stability of sliding between elastically deformable solids, *Journal of the Mechanics and Physics of Solids*, 49(9), 1865–1898, doi:10.1016/S0022-5096(01)00042-4, 2001.
- Rubin, A., and J.-P. Ampuero, Earthquake nucleation on (aging) rate and state faults, *Journal of Geophysical Research: Solid Earth*, 110(B11), doi:10.1029/2005JB003686, 2005.
- Ruina, A., Slip instability and state variable friction laws, *Journal of Geophysical Research: Solid Earth*, 88(B12), 10,359–10,370, doi:10.1029/JB088iB12p10359, 1983.
- Sato, T., and T. Hirasawa, Body wave spectra from propagating shear cracks, *Journal of Physics of the Earth*, 21(4), 415–431, doi:10.4294/jpe1952.21.415, 1973.
- Schwartz, S. Y., and J. M. Rokosky, Slow slip events and seismic tremor at circum-Pacific subduction zones, *Reviews of Geophysics*, 45(3), doi:10.1029/2006RG000208, 2007.
- Segall, P., E. K. Desmarais, D. Shelly, A. Miklius, and P. Cervelli, Earthquakes triggered by silent slip events on Kilauea volcano, Hawaii, *Nature*, 442(7098), 71, doi:10.1038/nature04938, 2006.
- Segall, P., A. M. Rubin, A. M. Bradley, and J. R. Rice, Dilatant strengthening as a mechanism for slow slip events, *Journal of Geophysical Research: Solid Earth*, 115(B12), doi:10.1029/2010JB007449, 2010.
- Shearer, P. M., G. A. Prieto, and E. Hauksson, Comprehensive analysis of earthquake source spectra in southern California, *Journal of Geophysical Research: Solid Earth*, 111(B6), doi:10.1029/2005JB003979, 2006.
- Shelly, D. R., G. C. Beroza, S. Ide, and S. Nakamura, Low-frequency earthquakes

- in Shikoku, Japan, and their relationship to episodic tremor and slip, *Nature*, *442*(7099), 188, doi:10.1038/nature04931, 2006.
- Shelly, D. R., G. C. Beroza, and S. Ide, Non-volcanic tremor and low-frequency earthquake swarms, *Nature*, *446*(7133), 305, doi:10.1038/nature05666, 2007.
- Smith, D. E., and T. H. Heaton, Models of stochastic, spatially varying stress in the crust compatible with focal-mechanism data, and how stress inversions can be biased toward the stress rate, *Bulletin of the Seismological Society of America*, *101*(3), 1396–1421, doi:10.1785/0120100058, 2011.
- Uchide, T., and K. Imanishi, Small earthquakes deviate from the omega-square model as revealed by multiple spectral ratio analysis, *Bulletin of the Seismological Society of America*, *106*(3), 1357–1363, doi:10.1785/0120150322, 2016.
- Wei, S., et al., The 2012 Brawley swarm triggered by injection-induced aseismic slip, *Earth and Planetary Science Letters*, *422*, 115–125, doi:10.1016/j.epsl.2015.03.054, 2015.
- Yang, W., and Y. Ben-Zion, Corner frequency ratios of P and S waves and strain drops of earthquakes recorded by a tight network around the Karadere segment of the North Anatolian Fault Zone: evidence for non-classical source processes, *Geophysical Journal International*, *205*(1), 220–235, doi:10.1093/gji/ggv560, 2016.
- Zanzerkia, E. E., G. C. Beroza, and J. E. Vidale, Waveform analysis of the 1999 Hector Mine foreshock sequence, *Geophysical Research Letters*, *30*(8), doi:10.1029/2002GL016383, 2003.
- Zheng, G., and J. R. Rice, Conditions under which velocity-weakening friction allows a self-healing versus a cracklike mode of rupture, *Bulletin of the Seismological Society of America*, *88*(6), 1466–1483, 1998.